1984

Photon statistics of light resonantly scattered from a three-level atom

Rollin Michael Evans
Iowa State University

INFORMATION TO USERS

This reproduction was made from a copy of a document sent to us for microfilming. While the most advanced technology has been used to photograph and reproduce this document, the quality of the reproduction is heavily dependent upon the quality of the material submitted.

The following explanation of techniques is provided to help clarify markings or notations which may appear on this reproduction.

1. The sign or "target" for pages apparently lacking from the document photographed is "Missing Page(s)". If it was possible to obtain the missing page(s) or section, they are spliced into the film along with adjacent pages. This may have necessitated cutting through an image and duplicating adjacent pages to assure complete continuity.

2. When an image on the film is obliterated with a round black mark, it is an indication of either blurred copy because of movement during exposure, duplicate copy, or copyrighted materials that should not have been filmed. For blurred pages, a good image of the page can be found in the adjacent frame. If copyrighted materials were deleted, a target note will appear listing the pages in the adjacent frame.

3. When a map, drawing or chart, etc., is part of the material being photographed, a definite method of "sectioning" the material has been followed. It is customary to begin filming at the upper left hand corner of a large sheet and to continue from left to right in equal sections with small overlaps. If necessary, sectioning is continued again—beginning below the first row and continuing on until complete.

4. For illustrations that cannot be satisfactorily reproduced by xerographic means, photographic prints can be purchased at additional cost and inserted into your xerographic copy. These prints are available upon request from the Dissertations Customer Services Department.

5. Some pages in any document may have indistinct print. In all cases the best available copy has been filmed.

University Microfilms International
300 N. Zeeb Road
Ann Arbor, MI 48106

Evans, Rollin Michael

PHOTON STATISTICS OF LIGHT RESONANTLY SCATTERED FROM A THREE-LEVEL ATOM

Iowa State University PH.D. 1984

Photon statistics of light resonantly scattered from a three-level atom

by

Rollin Michael Evans

A Dissertation Submitted to the
Graduate Faculty in Partial Fulfillment of the
Requirements for the Degree of
DOCTOR OF PHILOSOPHY

Department: Physics

Major: Nuclear Physics

Approved:

Members of the Committee:

Signature was redacted for privacy.

Signature was redacted for privacy.

In Charge of Major Work

Signature was redacted for privacy.

For the Major Department

Signature was redacted for privacy.

For the Graduate College

Iowa State University
Ames, Iowa

1984

TABLE OF CONTENTS

CHAPTER I. INTRODUCTION

Through the study of atomic spectra nuclear magnetic moments, spins, spectroscopic quadrupole moments and changes in mean square charge radii can be obtained. For the past fifty years, atomic spectra have provided information on stable and long-lived nuclei. It is now possible to extend these studies to short-lived (half life of less than one second) species.

The major advantage of spectroscopic techniques over others is their extreme sensitivity. Nuclear scattering experiments, muonic atom or X-ray isotope shift experiments may provide more information than spectroscopic methods, but require macroscopic amounts of material. It is possible with spectroscopic techniques to work with as few as 10,000 atoms/sec (1). This sensitivity opens up exciting possibilities. All the basic laws of nuclear physics have been derived from an intensive study of some 500 nuclei, namely those that are stable or can be reached from stable nuclei by simple nuclear reactions. The number of nuclei that have been produced is close to 1700, and it is conjectured that 7000 nuclei could eventually be identified (2). In exploring these new regions of short-lived nuclei, new nuclear properties or even new nuclear effects might well be discovered. Already nuclear structure and systematics qualitatively different from stable nuclei have

emerged in the measurements of a long chain of neutron deficient Hg isotopes (3).

A primary purpose of this work is to extend the sensitivity of optical detection techniques to the one atom/sec level through the use of the photon-burst method. The sensitivity increase is obtained by scattering large numbers of photons from a single atom. A number of new and interesting effects in the statistics of the resonantly scattered light then become important.

Nuclear Structure Information Through Optical Means

The addition of neutrons to a nucleus changes its mass, radius, magnetic moment and shape. Changes in the mass and electromagnetic moments of nuclei can be detected through their effects upon the electrons of the atoms (4).

The change in nuclear mass and radius from the addition of neutrons causes a shift in the electron energy levels. This isotope shift can be broken into two parts, one part arising from the change in size of the nucleus and the other arising from the change in mass. Electrons with orbits which penetrate the nucleus (S and $P_{1/2}$ states) are sensitive to nuclear size changes. However, the addition of a neutron also changes the center of mass of the nucleus-electron-cloud system shifting the electron energy levels. The exact size of this mass shift depends upon correlations between all electrons in the atom, which makes calculation of this

effect very difficult. The estimate of the specific mass shift is the single largest source of error in the determination of the change in nuclear size for this type of experiment.

The outer electrons are sensitive to the magnetic dipole and the spectroscopic quadrupole moments of the nucleus. The effect of these moments upon the electronic structure is to split a level into several sublevels. The number of these sublevels depends upon the nuclear and electronic spin. The splitting separations depend upon the electron wavefunction and the sizes of the electromagnetic moments of the nucleus.

Review of Spectroscopic Methods

A relatively new tool for spectroscopy is the high-power, narrow-frequency tunable laser. The resonant interaction cross section between atoms and photons is large ($\sim\lambda^2$) and beam fluxes of 10^{17} photons per sec are not difficult to obtain. The spectral purity and high degree of polarization of a laser makes possible great selectivity in the atomic transition and sublevel being probed.

The major spectroscopic techniques that have been used to probe short-lived nuclei can be grouped into three types: 1) RAdiation Detected Optical Pumping (RADOP), in which radiation from the nuclear decay is detected; 2) Atomic Beam Resonance (ABR), in which the atom itself is detected; and

3) Resonance Fluorescence, in which light scattered by the atom is detected. All of these techniques have been used for many years, but recently lasers have been used to increase their sensitivity.

In RADOP (3), as well as in the later LINO (Laser Induced Nuclear Orientation (5)) and LINUP (Laser Induced NUclear Polarization (6)) techniques an atom is optically pumped, partially aligning the nucleus with the polarization of the light source. An angular asymmetry may exist in the nuclear decay of the aligned nucleus. This alignment occurs when the laser is in resonance with one of the atomic hyperfine components. The hyperfine structure can be obtained by monitoring the anisotropic nuclear decay as a function of laser frequency. The great strength of this technique is the sensitivity of nuclear radiation detection.

The technique of atomic-beam resonance is among the oldest used for hyperfine structure work (7). Huber et al. (8) updated this technique to probe long chains of radioactive alkali isotopes (8, 9). In this system, a laser beam is used to alter the population distribution of the atomic m_f sublevels. The beam of radioactive atoms then enters the field of a strong sextapole magnet, where the nuclear spin, I, and electron angular momentum, J, decouple. The magnetic field gradient is set to focus only one m_j group onto the detector. The detector, a hot tungsten tube,

ionizes the focused beam of atoms as they pass through. The ions are then mass separated and counted by an electron multiplier. Optical resonances are observed by monitoring focused atoms of a particular mass as a function of laser frequency.

The two techniques described depend upon aligning the atom. As a result of this they do not work for spin zero nuclei. If a nucleus has an even number of protons, resonance fluorescence must be used to obtain information about the even neutron nuclei.

In resonance fluorescence experiments the hyperfine structure is probed by monitoring the laser light resonantly scattered by an electronic transition of an atom or ion. In experiments where the Doppler width of the optical transition is not a concern, a gaseous sample can be contained in a cell (10). If the Doppler width is comparable to the hyperfine or isotope shift splitting, and the density of atoms is insufficient for saturation spectroscopy techniques (11, 12), then an atomic beam must be used. Atomic-beam experiments have been performed with off-line (not directly coupled to an accelerator) thermal atomic beams (13) and with on-line fast beams (14, 15). A major difficulty in resonance fluorescence experiments is the high background from scattered laser light. Normally resonance fluorescence methods are not as sensitive as techniques

employing non-optical detection methods because of the high background.

Photon Statistics and the Photon-Burst Method

Resonance fluorescence techniques, as a rule, have higher background rates than methods utilizing non-optical detection. In a typical experiment, roughly 10^{14} photons/sec are being introduced into the system. If only one photon in a billion caused a background count, the background rate would be 10^{5} counts/sec. To attain sensitivity at the one atom/sec level, a way to discriminate between light scattered by atoms and light scattered by other sources is needed. If an atom excited by resonant light scatters photons at a rate of 10 MHz and if the light collection and detection system has an efficiency of 10%, the detection rate from one atom is 1 MHz. If the normal background rate is 10 kHz, the instantaneous signal rate due to an atom scattering photons is one hundred times greater than the background rate. This very high rate for a short time can be used to discriminate between background counts and counts from atom scattered photons. This is the basis of the photon-burst method. It is important that an atom spend sufficient time in the laser light so that the average number of detected photons per atom is at least one. For the case considered, this time must be at least 1.0 μsec. Previous work with barium and sodium atoms utilizing a .5 mm

interaction region (16, 17) established the effectiveness of the technique in increasing the signal to noise ratio. With this detection region, an atomic beam flux as low as ten atoms/sec could be used.

The statistics of the atom scattered photons for a two-level atomic system have been calculated in various ways (18, 19, 20, 21), and the photon probability distribution changes as the exciting field strength is increased. The laser field strength is characterized by Ω, the Rabi frequency parameter, and the atomic transition is characterized by A, the Einstein spontaneous emission coefficient. If the laser field is very weak ($\Omega << A$), the probability of an atom scattering n photons in time t is

$$P(n,t)=[(Rt)^n e^{-Rt}]/n!$$

$$R= A (\Omega^2/A^2)/(1+2 \Omega^2/A^2)$$

$$=A(\text{occupation probability of upper state}).$$

When the field is very strong ($\Omega >> A$), the probability distribution is

$$P(n,t)=[(At/2)^n e^{-At/2}]/n!.$$

In these two extreme cases, the scattered photon probability distribution is a Poisson distribution. In the intermediate region ($A \sim \Omega$), the probability distribution for on-resonance light is sub-Poissonian (18, 20), i.e., the width of the distribution is less than that of a Poisson distribution. The maximum deviation from Poisson statistics occurs when

$\Omega/A=2\sqrt{2}$. It has been shown (20, 22) that the deviation of the detected photon number distribution from the Poisson distribution depends linearly upon the light collection efficiency. If the light collection efficiency is low, a Poisson distribution is a good approximation in all cases.

For an atom to be used effectively in a photon-burst experiment, it must have an electronic transition which meets two criteria: the transition must be fast, and it must be essentially recyclable. A transition is fast if the atomic upper-level lifetime is much shorter than the atomic transit time. A transition is recyclable if the upper level can decay only to the electronic level from which it was initially excited. These conditions must be met if the atom is to undergo the many cycles of excitation and decay necessary for the photon-burst method to work.

If the transition is not strictly recyclable, as shown in Fig. 1.1, where the photon-burst transition is A-B,

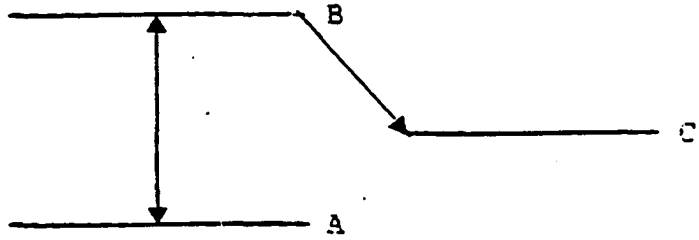

Fig. 1.1 Three-level atomic transition

the atom will quickly be pumped into state C unless the probability of the B-C decay is much smaller than the B-A decay. The photon-burst method can be applied to such a

transition, but the photon statistics are changed by the possibility of decay to state C. If all atoms are pumped into the C level before leaving the laser beam, the probability of detecting n photons is (18)

$$P_{op}(n) = \frac{(\gamma)^n}{(1+\gamma)^n} \quad \frac{(1)}{(1+\gamma)}$$

where $\gamma = R_1/R_2$. R_1 is the rate of photon detection, and R_2 is the rate of B-C transitions. Statistics of this kind are called optical-pumping-limited, as opposed to transit-time-limited statistics (the Poisson distribution). The optical pumping distribution is significantly wider than transit-time-limited statistics (i.e., super-Poissonian, as opposed to the sub-Poissonian statistics on resonance light in a two-level system).

The sensitivity of the photon-burst method depends upon the average number of detected photons received from each atom. The number of photons scattered by an atom during its trip through the laser beam can be increased by lengthening the laser-atom interaction region enhancing the sensitivity of the technique and extending its applicability to slower transitions. With this lengthened interaction region, small effects, such as B-C branching (Fig. 1.1) and momentum transfer from the laser beam to the atoms, become apparent and affect the photon statistics and fluorescence lineshape.

The barium 5535A transition used in previous work (18) is of the type shown in Fig. 1.1. The number of photons scattered in a 0.5 mm interaction region used in that work is too small for many B-C decays to take place, so the three-level nature of transition was not apparent from the photon statistics. Scattering more photons should make the effect of the B-C branch appear, causing the photons statistics to substantially deviate from transit-time-limited statistics. The detected photon probability distribution is then a mixture of the transit-time-limited and optical-pumping-limited statistics. The statistics of the detected photons can be used to measure the branching ratio of this transition. This is a new method. The atomic-branching ratio is an important quantity in some laser isotope separation experiments, in experiments to cool and trap atoms with radiation pressure, and often a sensitive test of atomic wavefunction calculations.

Previous work with this transition has suggested that the branching ratio is as low as 24 (23), i.e., for every 24 B-A transitions there is one B-C transition. More recent calculations indicate the branching ratio is closer to 600 (24). Experimental evidence for the ratio of 600 has been found through a photo-deflection experiment (25). A laser beam was used to impart transverse momentum to a thermal atomic beam. This momentum transfer "bent" the atomic beam

with the amount of bending being strongly dependent upon the number of photons absorbed. The branching ratio obtained from this photo-deflection experiment was 700.

The Doppler Effect and Fluorescence Lineshapes

The large number of photons scattered by an atom in the extended interaction region imparts a velocity along the laser beam to the atom. This velocity, through the Doppler effect, changes the ability of the atom to absorb photons. If the laser frequency is greater than the resonant frequency of the transition this change in velocity enhances the ability of the atom to absorb photons, but if the laser frequency is lower than the resonant frequency the probability of absorbing a photon is decreased by the change in velocity. This causes an asymmetry in the resonance fluorescence lineshape, which in turn causes the individual photon-burst spectra to be skewed. Asymmetries in individual burst spectra were not observed in the short interaction region experiments, but are apparent in the present work in cases where large numbers of photons are scattered.

Due to the nature of photon statistics the burst spectra lineshapes are not Lorentzian, and narrow with increasing multiplicity. High multiplicity spectra can have linewidths less than the natural linewidth, and, in principle, are limited only by the frequency spread of the laser.

Equipment

For photon-burst experiments the most important requirements for the laser system are long-term frequency stability and reliability. The burst method of data collection is necessary when extremely low beam fluxes of the sample are present. The sensitivity of the method enables beam fluxes of a few atoms/sec to be distinguished from background. Sweeping large frequency regions is necessary when searching for signals from new unstable isotopes. Time periods on the order of a day may be required. The system needs a frequency standard stable for such periods of time, and the entire system needs to be reliable enough for continuous operation for such time spans. In addition to long term reliability the laser linewidth should be less than that of the natural linewidth of the transition being studied. This allows the line-narrowing effect to be observed and utilized.

The light collection system must be able to accommodate a laser-atom interaction region of over a centimeter in length with low scattered background light and uniform light collection efficiency. The amount of background is of critical importance. Higher sensitivity is obtained by scattering proportionally more photons compared to the background. In this work, the laser beam input power is increased to saturate the transitions of atoms crossing the

interaction region. If the background scales with the size of the interaction region, there may be no gain in sensitivity over the .5 mm interaction region used previously.

Photon Burst and On-Line Methods

To use the photon-burst method to study short-lived nuclei produced on-line at an accelerator, the nuclei must be neutralized and delivered to the laser interaction region. A new technique being developed to produce radioactive nuclei and then transport them in the form of an atomic beam is the helium jet. Helium jets have been used previously to transport radioactive particles (26), but have never been used with a laser system. The helium-jet transport system developed in conjunction with this work at Argonne National Laboratory is shown in Fig. 1.2 (27). The target chamber is aligned along the path of a heavy-ion beam which passes through thin tantalum windows and interacts with the foil targets. Radioactive nuclei are produced in (HI,XN) reactions. These heavy-ion reaction products recoil out of the foil, where they are stopped by the one atmosphere of He gas in the cell. The gas in the cell flows out through the capillary tube carrying along the reaction products. The helium expands into the volume of the upper chamber while the higher mass recoil products continue on downward through the skimmer. The skimmer is mounted on a

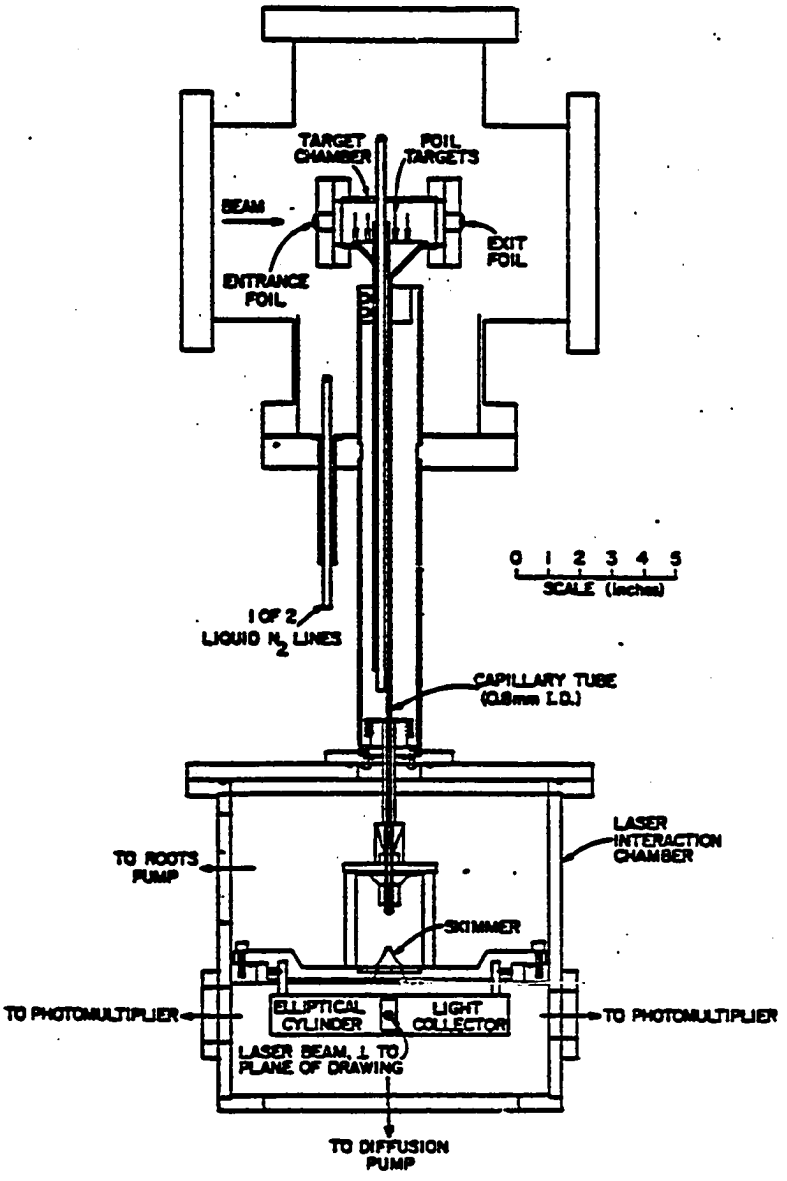

Figure 1.2 Helium jet system

plate which separates the low vacuum region ($\sim 10^{-1}$ torr) of the upper chamber from the high vacuum region ($\sim 10^{-5}$ torr) of the lower chamber. The laser-radioactive atom interaction takes place in the high vacuum region below the plate. The target cell, helium, and capillary are kept at liquid nitrogen temperature, which raises the transport efficiency of the jet. In tests of the transported radioactivities, the system at ANL with two 2 mg/cm^2 Sn targets and a 50 particle na carbon beam, 10,000 nuclei/sec were delivered to the tip of the capillary. Of this 10,000, a few hundred pass through the skimmer. This small atom flux makes the use of the photon-burst method necessary. At present, the system has not yet transported activity in the form of free atoms.

Photon Burst and Exotic Atom Searches

The sensitivity of the photon-burst method and the line narrowing effect can in principle be utilized to distinguish small numbers of "exotic" atoms from their host material. A search of this type has been made with sodium atoms looking for anomalously heavy isotopes (28). It is thought that extremely heavy particles present in the early stages of the development of the universe may have been incorporated into the structure of ordinary nuclei. These heavy isotopes, because of their high mass, would have a large isotope shift. This shift would distinguish them from ordinary atoms. Extremely high atom fluxes were necessary in this

experiment (~10^{10} atoms/sec). This large atomic flux leads to a large fluorescence signal far from resonance, due to the long Lorentzian tails of the atomic resonance. The photon-burst line-narrowing effect reduces this background. This experiment was sensitive enough to detect one atom containing a heavy hadron per approximately 10^{12} normal atoms (29). This experiment is being repeated with lithium which has the advantage that it was largely produced in the Big Bang. Because of the larger isotope shift for the lighter lithium nucleus, the sensitivity may be four orders of magnitude higher (30). A thermal beam of the relatively light lithium atoms will have velocities larger than in previous work, so it will be necessary to use a large interaction region, rather than the .5 mm region used for sodium. The effects of radiation pressure on the fluorescence lineshapes should also be quite pronounced.

A second proposed exotic atom search using resonance fluorescence techniques is to look for an atom with a free quark attached to the nuclei (30). The photon-burst signal processing technique could be used to increase the sensitivity of the search. A free quark would shift the atomic resonance by a large amount, eliminating the large background in the previously mentioned heavy particle searches. A caveat of this experiment is that the exact energy of the quark-atom electron transition would need to

be calculated with high accuracy or else prohibitively large frequency regions would need to be searched.

Thesis Structure

The goals of this work are as follows:

1) help develop the equipment necessary to do photon-burst spectroscopy in an extended interaction region and establish sensitivity limits;

2) observe non-Poissonian statistics that arise from scattering light from a three-level atomic transition;

3) use the non-Poissonian statistics as a new method to obtain weak atomic branching ratios; and

4) verify the effect of photon momentum transfer from the laser beam to the atoms on the fluorescence lineshape.

The thesis is arranged as follows: Chapter II describes the equipment necessary for photon-burst experiments; Chapter III covers the theory of photon statistics for a three-level system and the effect of photon-momentum transfer on the fluorescence lineshape; Chapter IV deals with the experimental problems that must be addressed when using a thermal atomic beam; Chapter V presents the experimental results and analysis; and Chapter VI is a brief summary of the conclusions.

CHAPTER II. EQUIPMENT

This chapter deals with the equipment that has been developed and assembled for high resolution laser spectroscopy. The basic components of the laser system are a commercial dye laser (Spectra Physics model 380a) in a ring configuration, with intra-cavity tuning and control devices, an active stabilization system to narrow the linewidth of the laser, and a method of generating a digital frequency scale at optical frequencies which is coupled to the dye laser. The active stabilization system and apparatus for frequency scale generation were developed for this work. In addition to the laser system itself, a device used to determine the absolute wavelength of the dye laser was constructed; an atomic beam chamber with which to conduct experiments has been built; and photon-burst electronics to process the fluorescence signal were developed.

Review of Dye Lasers

Laser dyes

The extremely wide tuning range of the dye laser arises from the structure of the dye molecule used for the lasing action. Dye molecules are made up of long chains of carbon, hydrogen and oxygen atoms all essentially lying in a plane. The electrons within the dye molecule move in an approximately square well potential, resulting in energy levels of $E_n=(n\,\hbar^2)/8mL^2$ where L is the length of the dye

molecule, m is the electron mass, and n is the quantum number giving the number of anti-nodes in the wavefunction of the electron. A long organic dye molecule also has many vibrational modes, some of which couple to the electronic structure. This superimposes a vibrational spectra on the square well potential, giving an energy level spacing such as that shown in Fig 2.1. These vibration lines are further broadened by collisions and electronic perturbations caused by the surrounding solvent. This gives rise to continuous, broad ground and excited states resulting in wide absorption and emission bands. These broad transitions allow the dye to absorb (and emit) light over a large wavelength region (31).

All lasers require a population inversion between the upper and lower states to operate. In a dye laser, this inversion is maintained by "pumping" the dye with light from an external source as illustrated in Fig 2.2. The input pump light raises the dye molecule energy from its ground state to some vibrationally excited state in the upper level. The excited electron quickly ($\sim 10^{-11}$ sec) drops to the lowest vibrational state in this level and then reradiates light by stimulated emission at a wavelength determined by the details of the laser cavity. The dye molecule quickly drops to the lowest vibrational level becoming available for additional excitations.

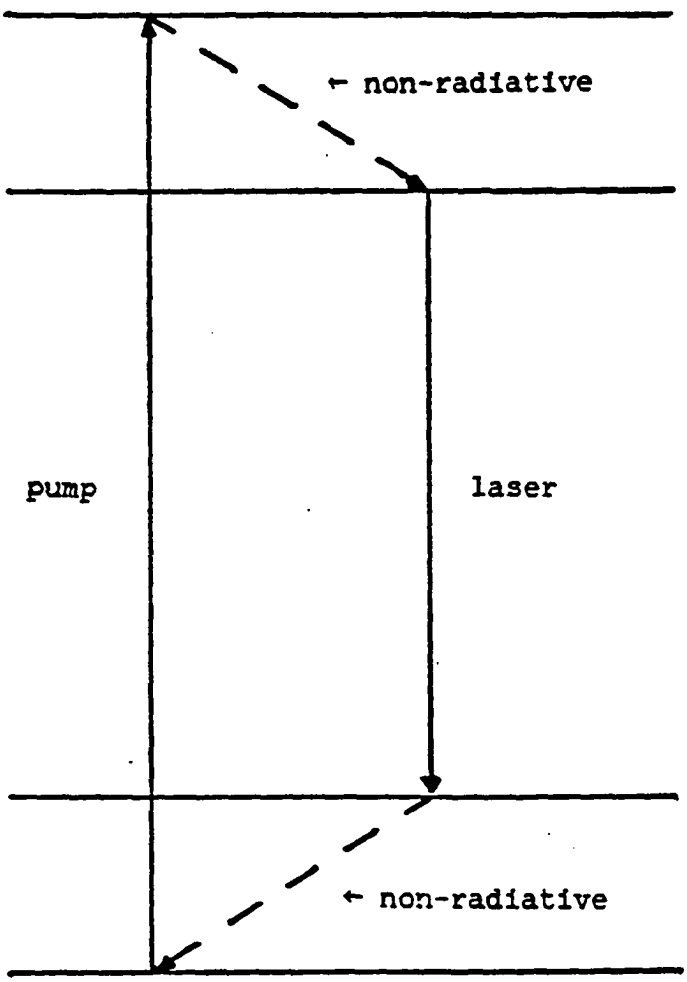

Figure 2.1 Basic energy level diagram of any laser

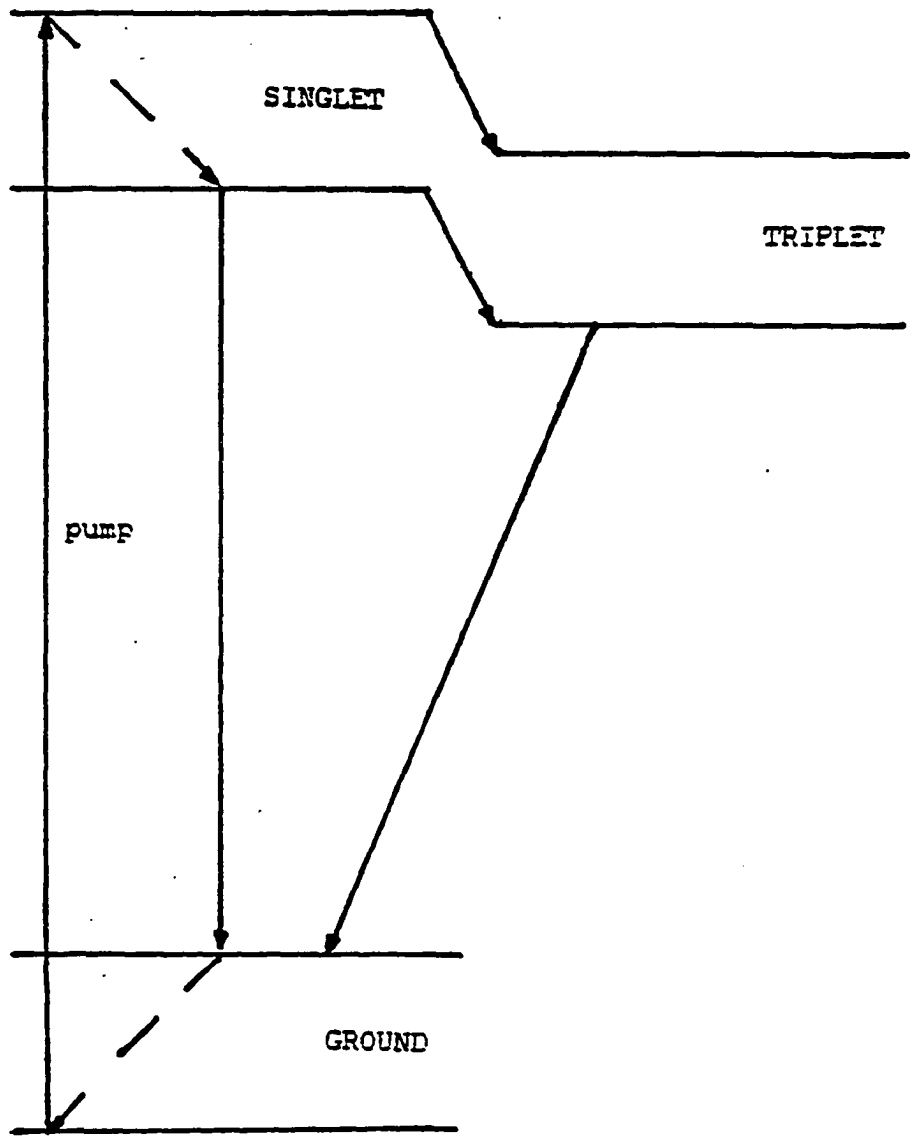

Figure 2.2 Energy level diagram applicable to organic dyes

In between each set of the singlet levels that have been considered so far is a triplet level (32) (see Fig. 2.2). Transitions from the singlet excited state to the triplet level are not as likely as the singlet excited to the singlet ground state, but once a dye molecule is in the triplet state it will not decay to the ground state for a very long time (1 μs for a triplet to singlet transition as compared to 1 ns for a singlet to singlet transition). After many cycles of excitation and decay, a large percentage of the dye molecules accumulate in the triplet state. Dye molecules in this triplet state are not available for lasing action. Also, since triplet to triplet transitions are possible, the dye molecules begin to absorb the laser light by trapping it in excited triplet states rather than emitting it in stimulated emission from singlet to singlet transitions. As time goes on, the absorption of the dye becomes greater than the gain of the dye and laser action ceases. The continuous wave (cw) dye laser avoids this by rapidly circulating the dye through cw laser pump light. Each dye molecule spends a short time passing through the pumping laser beam. The dye molecules accumulate in the triplet state as they pass through this beam, and then leave the pumping laser light. This allows the dye molecules to be replaced by fresh dye molecules that have not yet been trapped in triplet states.

A typical dye laser is shown in Fig. 2.3. The input pump light is supplied by an argon-ion laser and is focused onto a continuously circulating, optically flat dye stream. Three mirrors are used in the cavity. Two mirrors, the end mirror and the collimating mirror, are used to focus the laser light through the dye jet. The flat output mirror completes the cavity. The radii of curvatures of the collimating and end mirrors are such that the light rays between the collimating mirror and the output mirror are parallel. This parallel section of light in the resonator cavity is a convenient region to place the various tuning elements needed to insure single frequency operation.

Ring lasers

In dye lasers, of the type shown in Fig. 2.3, standing waves of frequency Mc/2L are set up inside the cavity, where M is some integer, c is the speed of light, and L is the optical path length of the cavity. Inside the dye jet the standing waves set up regions of extremely high electric fields (anti-nodes) and regions of weak electric field (nodes). This condition has two effects: 1) the parts of the dye in the weak field region are not effectively utilized for lasing action, and 2) the portion of the dye not being utilized by the standing wave pattern is available for lasing at a frequency Nc/2L, where N is an integer different than M. The utilization of only part of the laser gain media

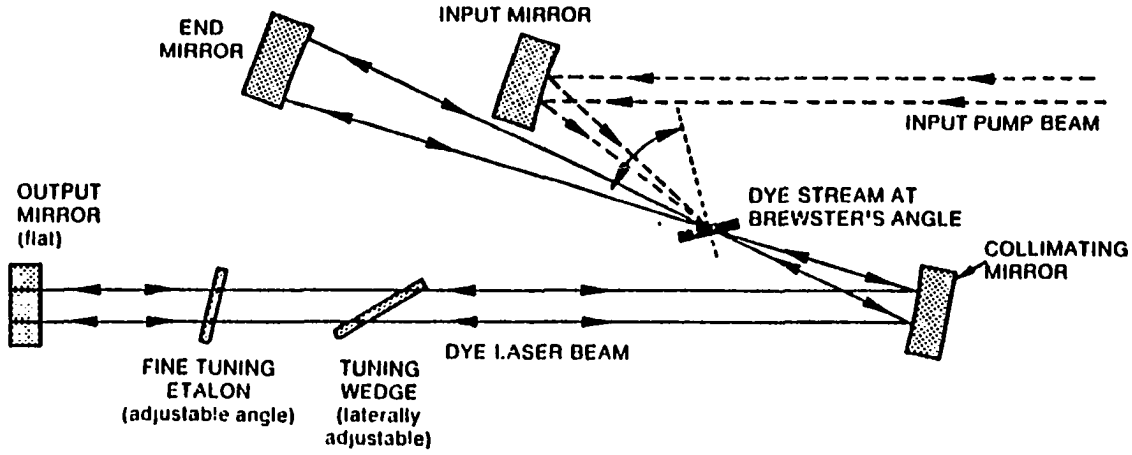

Figure 2.3 Dye laser optical schematic

by a standing wave pattern, called spatial hole burning (33), reduces the laser frequency stability and efficiency.

In a ring configuration, as in Fig 2.4, traveling waves propagate inside the cavity, avoiding the problems of spatial hole burning. However, the output of a laser that uses two counter rotating traveling waves does not have the frequency or amplitude stability of a laser with one traveling wave (34). In Fig 2.5b (35), an oscilloscope trace of the output of a ring laser which allows bi-directional propagation of traveling waves is shown. In Fig 2.5a the signal from the same laser operating with a single traveling wave in the cavity is shown. As can be seen this results in superior power and frequency stability.

Uni-directional operation is achieved by introducing a small differential loss between the two different directions of propagation, through the use of a "uni-directional device". The device consists of a Faraday rotator (36) and a piece of optically active quartz (36). In the presence of a strong magnetic field, certain types of glass become optically active (the Faraday effect). Glass, in such a field, rotates the polarization of light passing through it by an angle $\theta=VBL$, where B is the magnetic field in Teslas, θ is in minutes of arc, L is the length of the glass in meters, and V the Verdt constant, which depends on the type of glass being used. Both of the optically active materials

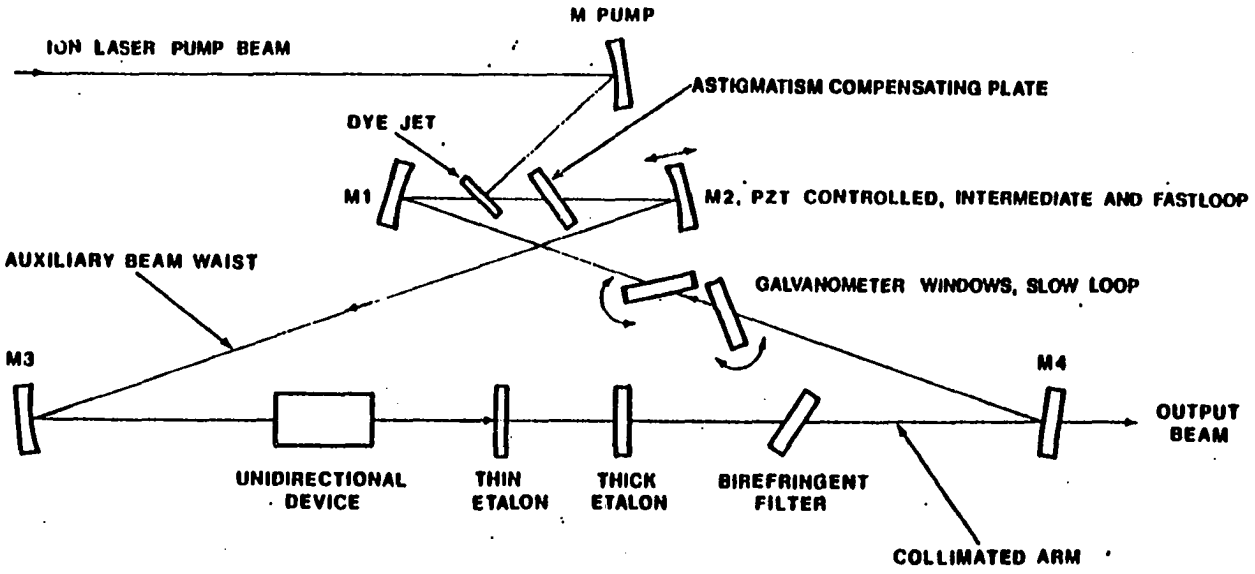

Figure 2.4 Ring dye laser configuration

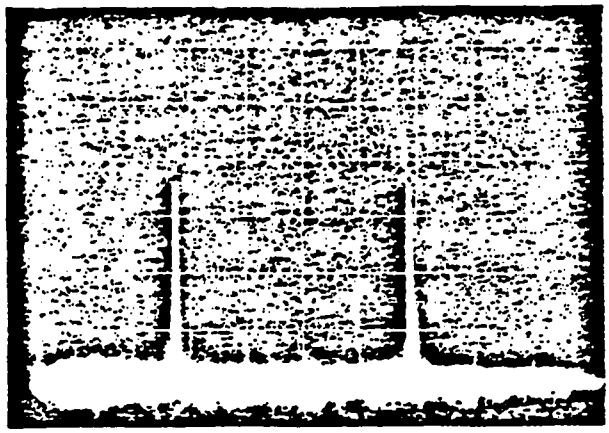

2.5a

2.5b

Figure 2.5 Fabry-Perot etalon display of laser output,
8 GHz free spectral range.
(a) Unidirectional operation, 20 mV/div
(b) Bidirectional operation, 20 mV/div

rotate the polarization of the incoming light, but there is a basic difference: the direction of the angle of polarization rotation depends upon the direction of travel through the optically active quartz and is independent of direction for the Faraday rotator. Light that passes through the piece of quartz and is again reflected back through the quartz exits with the original polarization: light making a round trip through a Faraday rotator has its polarization rotated through an angle of 2θ. Horizontally polarized light first entering the quartz in the uni-directional device is rotated through a small angle θ (θ~ 2.5 degrees in the laser being used in our work (37)). The Faraday rotator is so designed that after passing through it, the light is again horizontally polarized. Light traveling in the other direction, after passing through the Faraday rotator, has its angle of polarization rotated by -θ degrees. The optically active quartz rotates the polarization an additional -θ degrees, so the total rotation of polarization for light traveling in the other direction is 2θ (~5 degrees). Because of the large number of surfaces at the Brewster angle in the cavity, the light with the slightly rotated polarization experiences greater attenuation than light that is horizontally polarized. While the difference in losses for the waves traveling in the two different directions is small, it has been found (36) that a

differential loss of only .01% is all that is necessary to prevent lasing in both directions.

Frequency control of a dye laser

With a particular dye, a laser is capable of operating over a wavelength span of hundreds of angstroms. With no tuning elements in the cavity, the laser operates at the wavelength of highest gain, which normally is the peak of the dye emission curve (38). To change the laser frequency, the cavity gain as a function of wavelength must be controlled. In a Spectra-Physics 380a, this is done by inserting two etalons and a birefringent plate into the cavity.

A birefringent plate with its optical axis tipped with respect to the direction of energy propagation rotates the polarization of light passing through it. To a good approximation, for a plate at the Brewster angle, the angle of rotation is (39, 40, 41)

$$\delta=(n_e-n_o)\ T\ \sin^2(\eta)/(\lambda\ \sin\theta)$$

where (n_e-n_o) is the difference between the ordinary and extraordinary index, η is the angle between the optical axis and the axis of polarization, T is the plate thickness and θ is Brewster's angle. If $\delta=2\pi$, the polarization is rotated back into itself. As mentioned in the discussion of the unidirectional device, the numerous surfaces at the Brewster angle in the cavity cause any ray not horizontally polarized

to suffer attenuation. Rotating the plate about its axis (changing η) changes the wavelength which is rotated through a multiple of 2π, which in turn changes the cavity wavelength of highest gain.

The bandwidth of a birefringent plate tuner is on the order of 100 GHz. Longitudinal modes of a traveling wave laser occur every $\Delta\upsilon=c/L$, where L is the optical path length of the resonator. In the laser used for this work, $\Delta\nu$ is roughly 200 MHz. If only a birefringent plate tuner were being used to control the frequency of the laser, all modes near the top of the flat gain curve of the tuner would lase. This condition would result in a very large linewidth (~2 GHz). Consequently a device with a narrower bandpass, such as a Fabry-Perot etalon (42), which discriminates against adjacent longitudinal cavity modes is required. A Fabry-Perot etalon consists of two parallel partially reflecting mirrors a distance D apart. The condition for transmission through an Fabry-Perot etalon is

$$M\lambda=2D\cos\theta$$

where θ is the angle of incidence of the incoming light. The frequency difference between transmission peaks for $\theta=0$ is

$$\nu=c/2D.$$

This is called the free spectral range (FSR) of the etalon. The transmission through the etalon has an approximately Lorentzian lineshape given by

$$I(\nu)= \frac{1}{1+[4\pi D/(c(1-R))]^2 (\nu-\nu_0)^2}$$

where R is the mirror reflectivity and ν_0 is the central frequency of the peak. The full width at half maximum of the bandpass is

$$\Delta\nu=c(1-R)/(2\pi D).$$

The finesse of an etalon is the ratio of its FSR to full width at half maximum, or

$$F=\pi/(1-R) \quad (43).$$

In the 380a ring laser, two etalons are used. One of the etalons is thick (D ~2 cm) and tunable, and the other is a thin (D~.1 mm) piece of glass. The thick etalon is capable of discriminating against adjacent cavity modes, allowing only one cavity mode to lase. The FSR of this etalon is such that several of its transmission peaks exist inside the envelope of the birefringent tuner gain curve at one time. The laser can operate at the frequency of any of these transmission peaks. During operation, the laser could spontaneously change frequency by the FSR of the thick etalon (mode hop). To suppress mode hopping, the thin etalon is used to provide a third bandpass filter. This etalon

lowers the gain of the thick etalon transmission peaks that are not near one of its transmission peaks preventing frequency changing mode hops.

With the gain modifying devices in the laser cavity, the laser frequency can easily be set to any cavity mode. The cavity mode nearest the thick etalon transmission peak is the frequency at which the laser operates. The frequency of this etalon transmission peak is given by

$$\upsilon = Mc/2D.$$

Since M is a very large number ($\upsilon \sim 5 \times 10^5$ GHz, $c/2D \sim 25$ GHz) if D is changed by a very small amount the central transmission frequency changes significantly. A change in length can be accomplished by varying the voltage on the piezoelectric crystal which spaces the etalon mirrors. For the thick etalon, if the distance between the mirrors changes by a part in a million, the central transmission frequency will shift by 500 MHz. This large shift in frequency for a small change in mirror spacing not only facilitates tuning the etalon, but also makes such devices susceptible to thermal effects. The etalon in the laser cavity is made of a material that has a very low coefficient of thermal expansion and is always kept at about the same temperature through the use of an external heater.

If the thick etalon mirror spacing changes to such an extent that an adjacent laser cavity mode has higher gain,

the laser frequency will "hop" by 200 MHz. With the tuning elements described so far the laser frequency could only be changed in steps of 200 MHz rather than scanned continuously as desired. In addition to the cavity gain controlling elements which select a mode within the laser cavity, a method of continuously varying the output frequency is also needed. This is accomplished through the insertion into the cavity of a piece of glass which can be rotated about its axis perpendicular to the light path. Rotating the glass changes the optical path length the light must follow to complete one trip around the cavity which in turn changes the frequencies of the cavity modes. Light passing through the rotatable glass plate (galvoplate) is displaced a small amount, depending on the angle that the light enters. To avoid changing the position of the light path inside the cavity two counter-rotating galvoplates are used. This minimizes variation in the power and position of the output light.

The laser frequency can be continuously varied with the tunable thick etalon-galvoplate combination. To insure a smooth scan the transmission peak of the tunable etalon must be kept centered about the laser output frequency. A two kHz sinusoidal signal is sent to the etalon piezocrystal. This changes the spacing of the etalon mirrors by a small amount, which in turn changes the central transmission frequency of

the etalon. This small two kHz shifting of the etalon central transmission peak causes a small four kHz amplitude modulation of the output power when the etalon is locked to the laser output frequency. A small fraction of this power is measured by a photodiode-beamsplitter combination. The signal is then multiplied by a square wave that has been phase locked to the two kHz etalon drive signal. If the etalon transmission peak is truly centered on the laser transmission, the result is, when low passed filtered, zero. If the etalon transmission peak is not centered on the laser frequency, the filtered signal has a net positive or negative value, depending upon the direction of the frequency drift. This signal, suitably amplified, is fed back to the etalon piezocrystal, forcing the etalon transmission peak to move toward the laser frequency. As the galvoplates are rotated, this lock forces the etalon transmission frequency to remain at the mode frequency. This arrangement insures continuous single mode scans of tens of GHz.

DC Lock

The linewidth of a dye laser is affected by many internal and external factors. Mechanical vibrations which change the cavity mirror position broaden the laser linewidth. Fluctuations in pressure and position of the dye jet can similarly cause jitter in the laser frequency

output. Careful attention must be paid to minimize these sources of noise to avoid large laser linewidths. To minimize mechanical vibration the laser resonator cavity must be made of a very rigid material and the laser must be isolated from mechanical vibration sources. The dye jet solvent must be viscous enough to provide a stable jet. The laser used has a free running linewidth of about 40 MHz. For our applications the desired linewidth must be less than 20 MHz, the natural linewidth of the 5535 A transition in barium.

To narrow the laser linewidth to an acceptable level we have developed an active stabilization system. The basic idea is the laser output frequency noise can be reduced by controlling its frequency with a device which is less sensitive to environmental factors than the laser. In this system the frequency sensitive device used to stabilize the dye laser is a commercial etalon. The mirrors of the etalon are spaced by Invar, a material which is relatively insensitive to thermal changes. It has a FSR of 8 GHz and a transmission peak FWHM of 40 MHz. Laser light passing through the etalon has a transmission curve as shown in Fig. 2.6. The etalon transmission and incident light intensities are measured. The difference between these two signals depends on the frequency of the input light. If the laser frequency drifts so that the light transmitted through

the etalon is given by A (Fig. 2.6), a signal proportional to A-C is fed back to the laser, forcing it to give the etalon transmission value C. If the frequency drifts so the transmission through the etalon is at level B, a feedback signal proportional to B-C is sent to the laser, and the electronic gain forces the laser to have an etalon transmission value of C. If the frequency manages to somehow get to frequency D, the electronics send the laser the same feedback that was sent to it when it drifted to A. The frequency lock is lost when this occurs. To avoid this problem we take advantage of the fact that the laser frequency rarely suddenly changes by more than 200 MHz. If the frequency difference between points C and E (Fig. 2.6) is greater than 200 MHz, the laser frequency seldom hops outside of the etalon capture range. In this etalon configuration the laser stays locked for many hours at a time.

The feedback signal sent to the laser is split into two components: a low frequency component sent to the galvoplates and a high frequency component that is sent to a low mass cavity mirror mounted on a piezoelectric crystal (Fig. 2.7). This arrangement is necessary because the massive (in comparison to the low mass mirror) galvoplates have a mechanical resonance at 500 Hz. The electronics for the galvoplates is designed to roll off the frequency

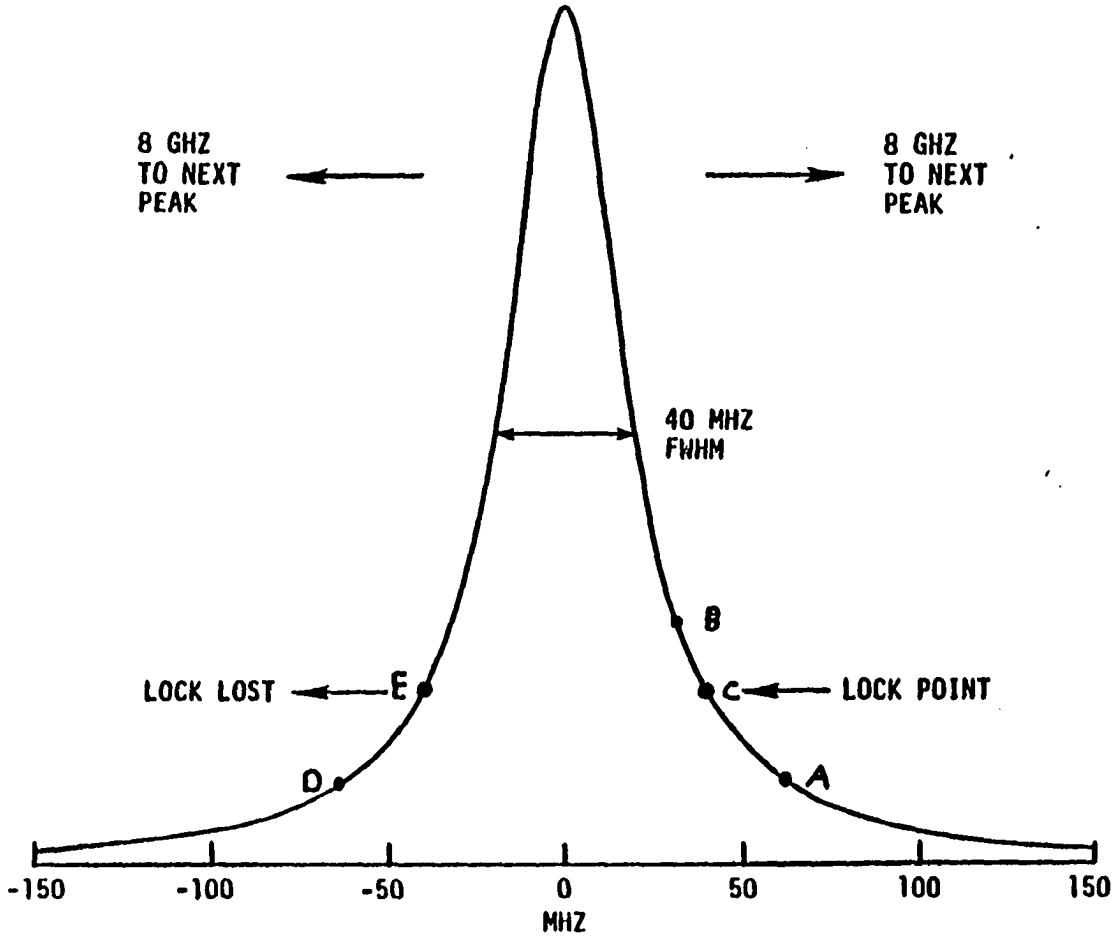

Figure 2.6 Etalon transmission for DC lock

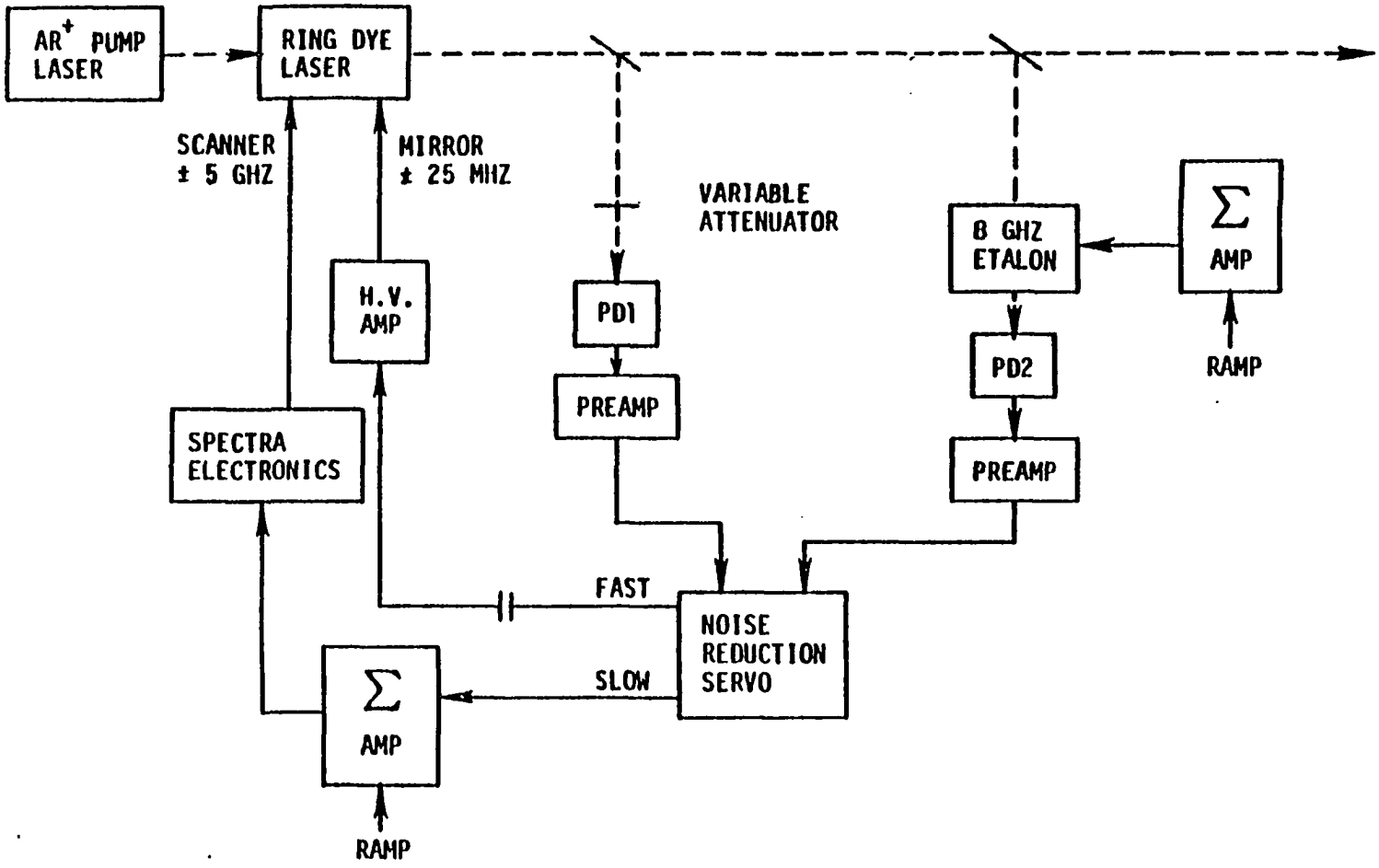

Figure 2.7 DC lock schematic

response of the amplifiers to insure that the gain is much less than one at 500 Hz, avoiding this resonance. As the laser frequency is scanned a compensating ramp voltage is added to the slow signal of the DC Lock. If this ramp were not used an error signal proportional to the scanning frequency change would appear in each feedback circuit as the laser is scanned. Each feedback circuit has a similar ramp signal added to its output, so the lock systems only need deal with the random frequency drifts and the non-linearities of scanning elements.

The high frequency signal is AC coupled and responds to noise from above DC to well over 10 kHz. This feedback signal, suitably amplified, is sent to the piezocrystal mounted mirror (M2 in Fig. 2.4). Moving the mirror changes the optical path length of the laser cavity which shifts the cavity modes, just as the cavity modes shift frequency when the galvoplates are rotated.

This dual fast and slow lock system reduces the laser linewidth from above 40 MHz free running (no external stabilization) to 7 MHz when locked to the 8 GHz etalon. A spectrum taken with this system is shown in Fig. 2.8. The natural linewidth of the transition is ~ 250 kHz (44), and the Doppler linewidth of the atomic beam used is roughly 1 MHz. Each horizontal mark is .911 MHz. The linewidth that is not due to Doppler broadening of the line or the natural

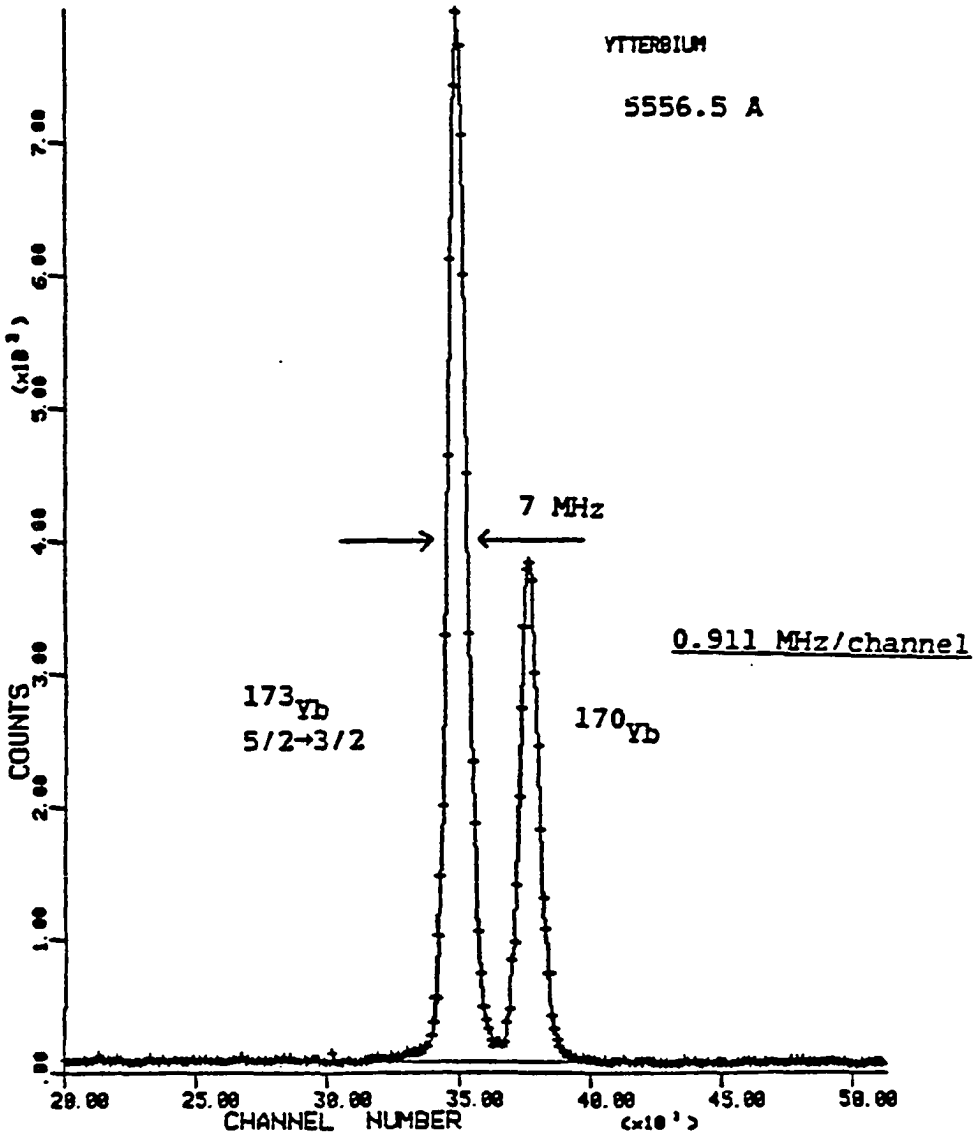

Figure 2.8 Ytterbium spectrum taken with laser system

linewidth of the transition is assumed to be due to the linewidth of the laser.

Heterodyne Lock

The laser system thus far described has a relatively narrow linewidth and is capable of being scanned, but its long term frequency stability is determined by the frequency stability of the 8 GHz etalon. An unstabilized etalon such as that being used in this system can easily drift tens of MHz an hour. A thermally stabilized, pressure regulated etalon would be better, but a system consisting of a dye laser and locking reference etalon would not have a convenient, reproducible frequency scale that is important for hyperfine structure measurements. Although other methods have been developed using only etalons (45) or external interferometers (46) as the ultimate frequency reference and frequency scale for laser systems, this system uses an optical heterodyne technique to generate the frequency scale and a stabilized transverse-field Zeeman laser as the frequency reference. The basic technique has been described by others (47, 48) but the execution in this system is somewhat different (49). The components needed for the heterodyne system are a stable reference laser, a tunable laser, and a method to control the frequency difference between them.

The beat frequency between the two lasers can be controlled by changing the frequency of the tunable laser. The frequency difference, after being scaled by a computer controlled divisor, is equivalent to a phase-locked voltage controlled oscillator in a frequency synthesizer. The frequency of the tunable laser can be changed by changing the divisor. The absolute frequency stablity is determined by the stability of the reference laser.

The tunable laser was constructed using a short (10.5 cm) helium neon (He-Ne) plasma tube sealed with windows mounted at the Brewster angle. External mirrors, one flat and the other with a radius of curvature of 60 cm, are mounted in precision angular-positioning devices (Oriel Model 1435). This particular choice of mirrors (60 cm, flat) was found to produce more power and make the laser less likely to operate in transverse modes other than the lowest order mode (TEM_{00}) (50) than mirrors with smaller radii of curvature. The angular positioning devices are mounted on aluminum blocks which are spaced by Super Invar rods roughly 15 cm apart. This distance is as close as the mirrors can be placed and still allow access for mirror and Brewster window cleaning. The separation of the mirrors has a large effect on the tuning range of the laser. A gas laser, such as a He-Ne, can only operate in a frequency range fixed by the atomic transition being used and its Doppler width. For this

particular laser the Doppler broadened gain curve is approximately 1.5 GHz wide, i.e., the laser can operate at any frequency inside this 1.5 GHz envelope. The 60 cm radius mirror can be moved with an applied voltage to the piezoelectric crystal device which positions it. The laser frequency is continuously tuned by changing the cavity length. If the laser cavity length is changed such that an adjacent cavity mode has higher gain, the laser frequency changes by c/2L. The frequency between the hops is the tuning range of the laser. Making the spacing between the mirrors (L) as small as possible makes the frequency between mode hops as large as possible, maximizing the tuning range. For this laser the maximum tuning range is roughly 1.12 GHz.

The reference for this heterodyne system is a commercial laser (Laboratory for Science Model 200) incorporating a standard internal mirror Spectra-Physics He-Ne plasma tube placed in a transverse magnetic field. Normally, a tube of length greater than 20 cm, such as this, operates on more than one longitudinal mode. However, a normally multi-mode He-Ne placed in a transverse magnetic field of between 200 to 3500 gauss operates on single cavity mode (51, 52). This effect, known as single mode collapse, is thought to be caused by the Zeeman frequency shifts in the neon sublevels. When the shifts approach the mode spacing, the mode structure of the multi-mode laser collapses, due to mode

coupling, leaving a single strongly lasing mode (52). Due to the magnetic field the gas in the tube emits light that is linearly polarized along the pi and sigma axis. The magnetically induced birefrigence in the gas causes the two polarizations to have slightly different frequencies. The frequency difference between the pi and sigma components of the single mode varies as the mode is tuned across the gain profile of the He-Ne. This frequency difference can be exploited to produce a simple frequency stabilization scheme. Zeeman lasers stabilized in this manner (controlling the frequency difference between the two polarizations) have central frequencies that are extremely stable, some experimenters claiming a frequency variation of one part in 10^{10} (53). The frequency stability claimed by the manufacturer of the laser being used in this system is a variation of less than 300 kHz per day.

The heterodyne frequency between the stabilized Zeeman laser and the tunable laser provides the frequency scale for the system. A beat note is obtained as shown in Fig. 2.9. The two laser beams are expanded to the same size and set to focus at infinity with beam expanding telescopes (B.E.). The beams are then focused by a lens onto the small active area of a fast photodiode (PD5). The stabilized laser is extremely sensitive to retro-reflected light. The $\lambda/4$ plate is placed between PD5 and the stabilized laser to

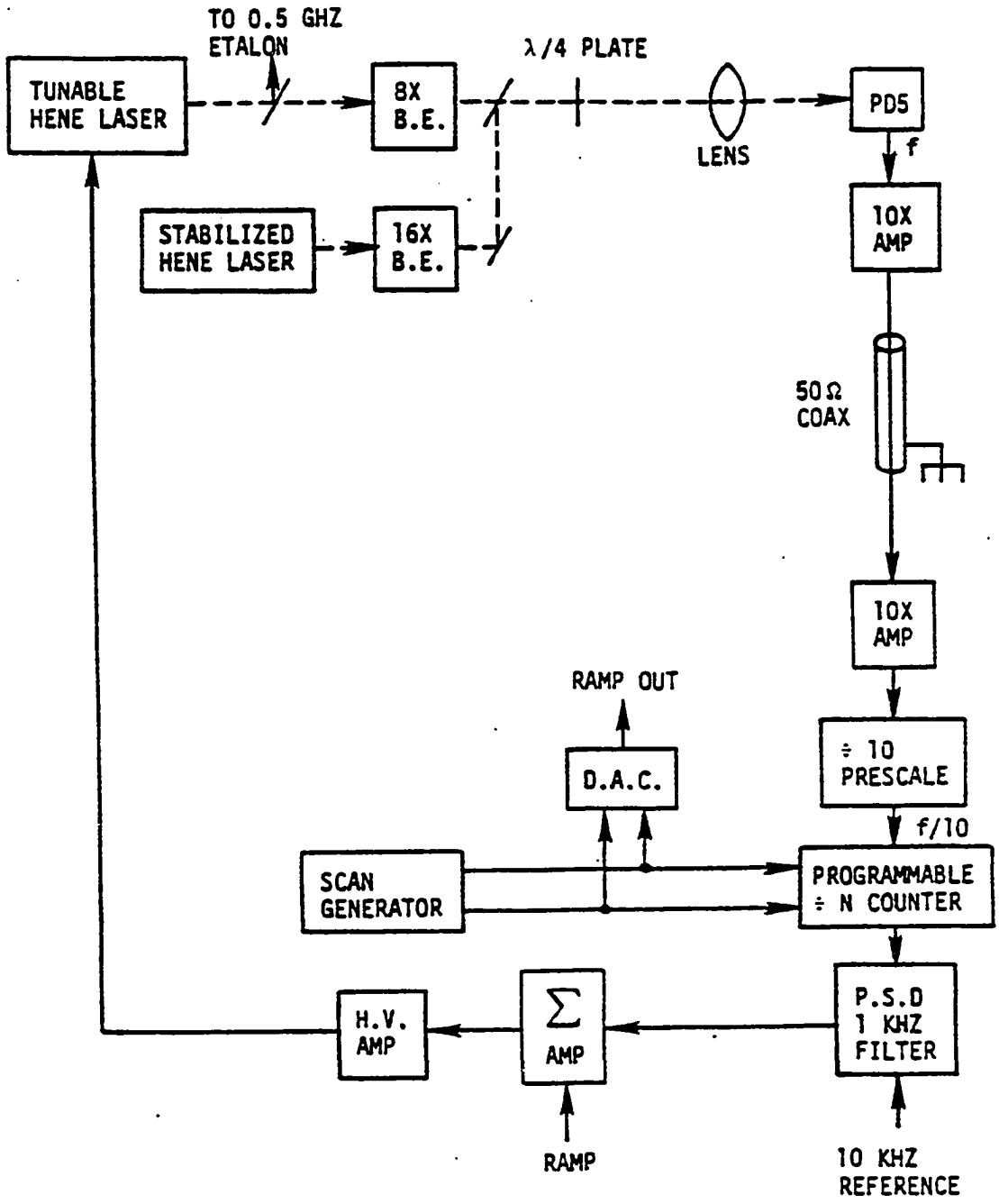

Figure 2.9 Heterodyne lock schematic

interchange the polarization of reflections from the fast photodiode, which results in greater stability. The signal from the photodiode is amplified by two Hewlett-Packard 10855A preamplifiers. This .2 V peak to peak sinusoid is amplified and converted to TTL levels by a Racal 9915 frequency meter. The counter not only changes the analog heterodyne signal to a digital TTL signal but also provides a convenient monitor of the heterodyne frequency. The frequency of the TTL signal from the first decade counter of the frequency meter is then divided by four and further divided by some large number N (typically N is between 250 and 1500). The result is phase locked to 10 kHz. The output of the phase sensitive detector provides an analog signal whose amplitude is proportional to the phase difference between the heterodyne frequency divided by 40N and 10 kHz. This signal is used to drive the piezoelectric crystal mounted mirror of the tunable laser forcing it to maintain a frequency difference of 40N[10 kHz]=[.4 MHz]N from the stabilized laser. By changing N to N+1 (or N-1) the frequency of the tunable laser can be changed in steps of .4 MHz. This generates the frequency scale.

Transfer Etalon

What has been described are two separate laser systems: first, a narrow frequency dye laser, and second, a dual He-Ne laser system that is capable of generating and

maintaining a frequency difference of 100 to 700 MHz between the two lasers and whose absolute frequency is stable within 300 kHz per day. A confocal etalon has been constructed to couple these two systems, transferring the frequency scale of the heterodyne lock to the dye laser. This is accomplished by locking a transmission peak of the etalon to the tunable He-Ne and locking the frequency of the dye laser to a second transmission peak of the etalon. As the tunable He-Ne laser frequency changes, the dye laser frequency is forced to track.

A diagram of the transfer etalon system is shown in Fig. 2.10. Light from the tunable He-Ne and the dye laser are combined on a beamsplitter. The two beams are sent through the etalon, and the transmitted dye and He-Ne light is separated by a dichroic beamsplitter (36) and detected by two photodiodes. Light striking PD3 (Fig. 2.10) passes through an interference filter, which eliminates light of wavelengths other than that of the He-Ne laser. This prevents the dye laser light from masking the He-Ne signal at PD5. Since the tunable He-Ne light is vertically polarized and the dye light is horizontally polarized, a polarizing filter prevents He-Ne light from striking the dye photodiode (PD4).

Figure 2.10 Transfer etalon
lock schematic

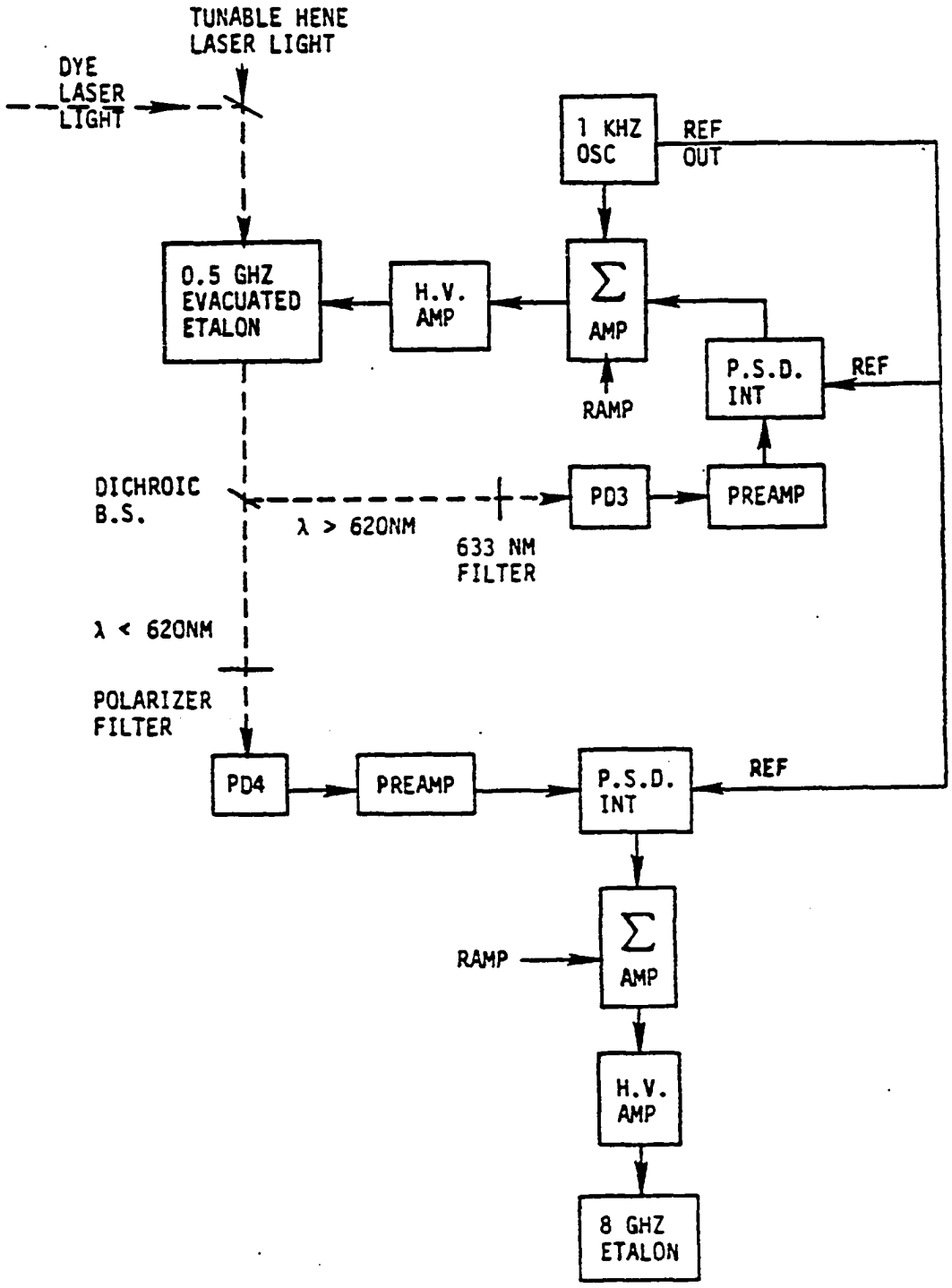
TUNABLE HENE
LASER LIGHT
DYE
LASER
LIGHT
1 KHZ
OSC
REF
OUT
0.5 GHZ
EVACUATED
ETALON
H.V.
AMP
Σ
AMP
RAMP
P.S.D.
INT
REF
DICHROIC
B.S.
λ > 620NM
633 NM
FILTER
PD3
PREAMP
λ < 620NM
POLARIZER
FILTER
PD4
PREAMP
P.S.D.
INT
REF
RAMP
Σ
AMP
H.V.
AMP
8 GHZ
ETALON

The etalon is swept 6 MHz with a 1 kHz sinusoidal signal. As discussed previously, if the transmitted light frequency is centered with respect to the swept etalon transmission peak, the light intensity has a minimum 1 kHz amplitude and a maximum 2 kHz amplitude. The 1 kHz signals from the two photodiodes are received by their respective phase sensitive detectors (PSDs) which are referenced to the driving signal. The signal from the dye laser PSD is proportional to the frequency difference between the laser output frequency and the etalon transmission frequency. This signal is sent to the eight GHz etalon, which controls the dye laser output frequency through the DC lock. The signal from the tunable He-Ne PSD is proportional to the frequency difference between the etalon central transmission frequency and the tunable He-Ne frequency. This PSD signal is fed back to the etalon keeping its transmission frequency centered on the He-Ne output. Changing the tunable He-Ne frequency forces the etalon transmission frequency to change, which in turn forces the dye laser frequency (through the DC lock) to change.

The etalon has a FSR of 466 MHz and is sealed in its own vacuum chamber to avoid problems with differential changes in the index of refraction of air associated with changes in pressure. The dye laser frequency is adjusted to have a transmission peak through the etalon at some frequency

$F_1=n_1c/4L$, where c/4L is equal to 466 MHz. The tunable He-Ne laser has a similar transmission peak at some frequency $F_2=n_2$ 466 MHz. The dye laser frequency is then forced to stay at frequency F_1 by locking it to the etalon. The etalon length is controlled by keeping the n_2 transmission peak centered on the tunable He-Ne laser frequency.

If the tunable He-Ne frequency changes from F_2 to F_2' (by changing the heterodyne lock number N to N') the etalon changes its length from L to L + ΔL to keep the He-Ne laser transmission peak centered. This forces the dye laser to change its frequency from $F_1=n_1c/4L$ to $F_1'=n_1c/(4(L+\Delta L))$, so

$$F_1'=n_1c/4L(1+\Delta L/L)=n_1c(1-\Delta L/L)/4L$$

or

$$F_1-F_1'=n_1(\Delta L/L)466 \text{ MHz}$$

since ΔL is very small in comparison to L. The He-Ne frequency change is

$$F_2-F_2'=n_2c(\Delta L/L)/4L=n_2(\Delta L/L)466 \text{ MHz}.$$

The frequency change F_2-F_2' is a known quantity controlled by the heterodyne lock system. The change in the dye laser frequency is then

$$F_1-F_1'=(n_1/n_2)[F_2-F_2'].$$

The ratio n_1/n_2 is equal to the ratio of the dye laser frequency to the He-Ne laser frequency, which is known. As

the He-Ne frequency is changed, the dye laser changes frequency by a known amount giving the dye laser an accurate and reproducible frequency scale. The tunable He-Ne, through the Zeeman laser has its absolute frequency held fixed, and through the transfer etalon the dye laser frequency is held stable over long periods of time.

The system scan range is fixed by the scan range of the heterodyne lock (roughly 500 MHz). After scanning one frequency region with the heterodyne lock, the dye laser frequency can be changed by the FSR of the etalon, accessing a frequency region 466 MHz higher (or lower). Using this technique the frequency scale can be extended from its 500 MHz heterodyne lock limitation to many gigahertz by successively jumping the laser frequency by the FSR of the transfer etalon.

This completes the description of the laser system which possesses the following properties:

1) wide wavelength tuning range (use of dye laser);

2) high power and frequency stable light source (use of ring configuration);

3) narrow frequency light source (use of active stabilization);

4) accurate, reproducible frequency scale (use of heterodyne lock system);

5) long term absolute frequency stability (use of Zeeman laser);

6) wide frequency range with calibrated scan (use of transfer etalon).

Wavemeter

To set the dye laser frequency to the desired atomic transition, some method is needed to measure the absolute wavelength. A Michelson interferometer (36) with an arm terminated by a reflector movable over a one meter length has been constructed for this purpose. The geometry is based on a design by Kowalski et al.(54). A corner cube (Fig. 2.11) is mounted on a twenty five cm air track glider so the cube can be smoothly moved over long distances. The laser light is separated by a beamsplitter. The two beams follow different paths, one path leading directly to the photodiode, the other reflected and displaced by the corner cube and recombined with the first beam by a second beamsplitter. If the corner cube moves a distance of $\lambda/2$, where λ is the wavelength of the dye light, the path length difference between the two beams changes by λ. As the cart moves, the two collinear beams alternately go from being completely in phase to being completely out of phase. Thus the photodiode detects a sinusoidal variation of the incoming wavefront. The number of fringes counted depends on the distance the cart moves and the wavelength of the incoming light. The distance the cart moves is measured by sending a He-Ne beam along the same path as the dye light

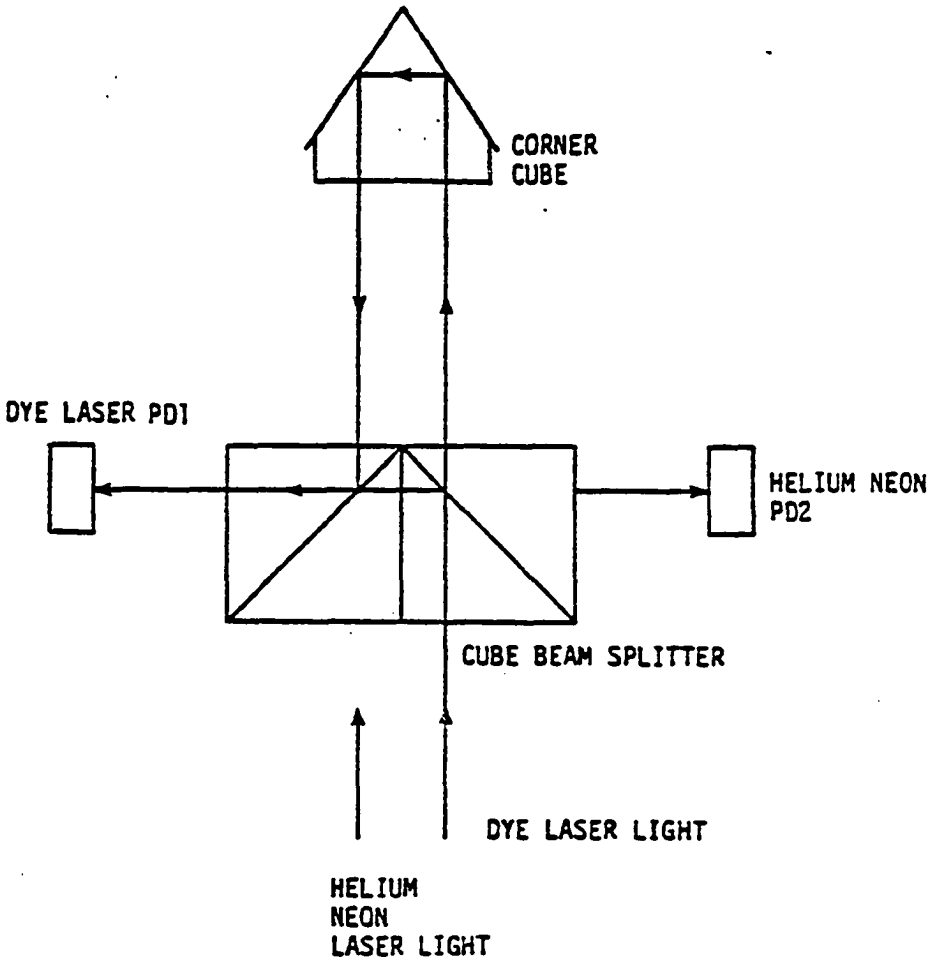

Figure 2.11 Wavemeter

but in the opposite direction. The ratio of the number of dye fringes counted to the number of He-Ne fringes counted in the same distance is the ratio of the two frequencies. The wavelength of the He-Ne laser is well known (6328.198 A), so the wavelength of the dye light is easily obtained from this ratio. In practice a two channel counter is used to count the nodes. The counter is programmed to stop after receiving a preset number of He-Ne light fringes. The number is some convenient power of ten (100,000 or 1,000,000 typically) so the frequency ratio is easily read from the counter display.

In one complete trip of the cart along the air track, the cart moves through roughly six million He-Ne laser nodes. Using this entire distance would result in a statistical precision of about 80 MHz. This precision is not necessary since the device is used only to set the dye laser frequency close to an atomic transition. The dye laser, when not locked to external electronics, can easily scan 10 GHz, so a million (roughly good to 480 MHz) fringes are all that are normally used. Kowalski et al. have stated (54) that an air track wavemeter such as this might possibly have its accuracy pushed to a part in 10^9, but because the He-Ne used is not stabilized and there are problems in obtaining a smooth travel of the air cart, a part in a million precision is the limitation of the present device.

Atomic-Beam Chamber

The atomic-beam chamber houses the apparatus that produces the atomic beam, the light collectors, and parts of the optics chain. This provides an atomic beam for off-line experiments and a reference atomic beam during on-line experiments.

The chamber is built out of standard four inch "dependex" couplings. The vacuum is maintained with a four inch diffusion pump. A liquid nitrogen cold trap between the diffusion pump and the rest of the chamber is used to prevent oil from the pumps from backstreaming into the chamber, coating the light collectors and destroying them. Pressures of 10^{-6} to 10^{-7} torr have been obtained with this pumping system.

The atomic beam is produced by evaporating a sample of the element being studied below a pair of small circular apertures. The sample is held in a tantalum crucible which is in turn placed in a resistively heated oven. The oven has reached temperatures as high as $1200^{o}C$ as measured by an optical pyrometer. Power is supplied by 120 V AC line voltage going through a variable transformer and a 120V to 12V transformer.

The slit system above the oven allows atoms in a small cone to pass through the light collector. The angular divergence determines the Doppler width of a given element for the atomic beam being used. The circular slits are made

to be removable so the angular divergence appropriate for the particular experiment can be obtained. For this work the average Doppler width is 3 MHz for barium and the atomic beam is .26 mm wide at the interaction region.

The light collector is designed to accept as much of the light scattered from the atomic beam as possible while rejecting light from other sources. This light selection is done by using polished elliptical cylinders as mirrors with the atomic beam at one line focus and slits at the other line focus. Light scattered by the atomic beam is detected by photomultiplier tubes (Fig. 2.12). The slit separation is made as small as possible to reduce the background scattered light detected by the photomultiplier tube and yet allow all light scattered by the atomic beam to be seen by the photomultiplier tube. These considerations (large collection efficiency with low background rate) determine the shape of the ellipse.

The light collection system is designed to accommodate an atomic beam roughly one mm in diameter. The size the image of a one mm source has at the second focus determines the slit opening. The "magnification" for ellipses of various eccentricities was determined using a two dimensional ray tracing program for axial (along the axis defined by the two foci of the ellipse) and transverse

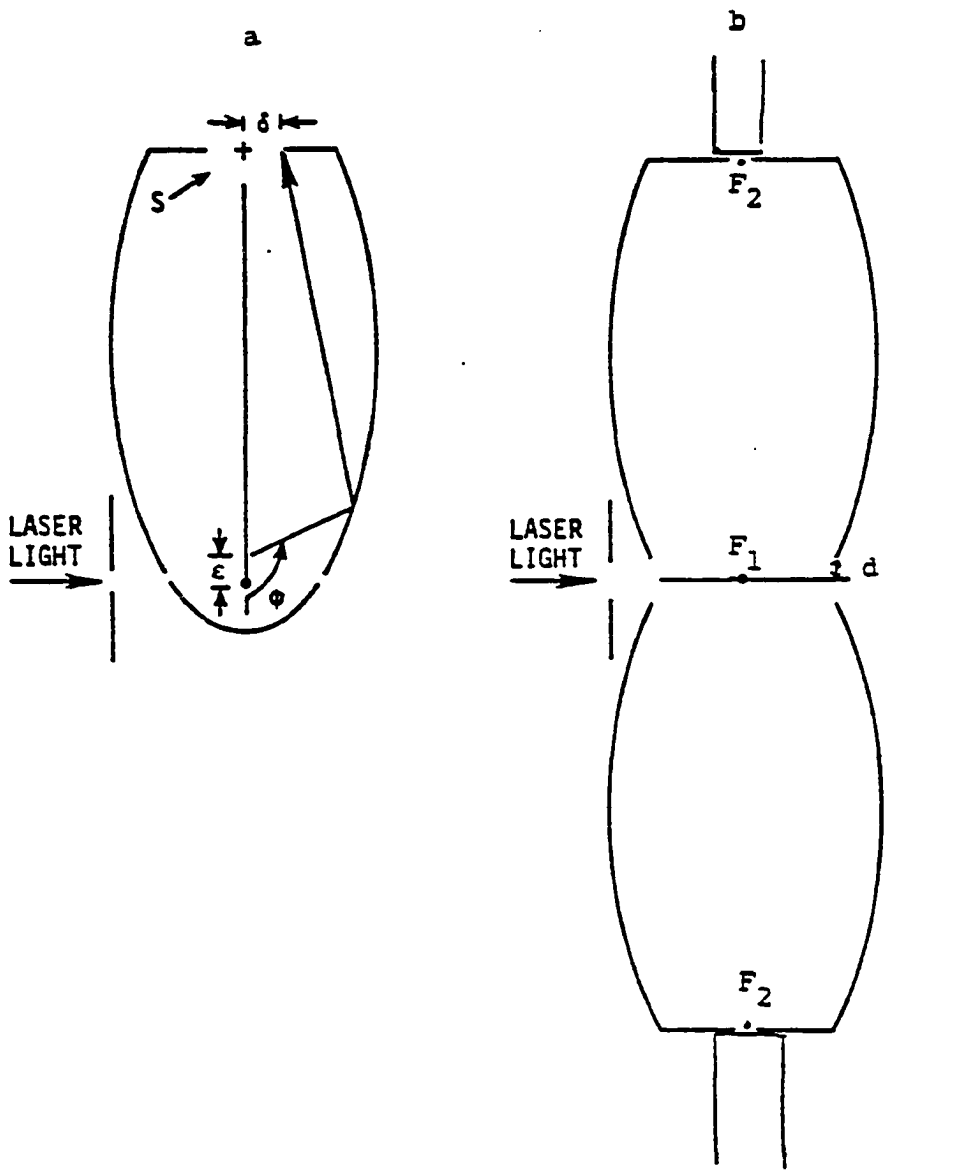

Figure 2.12 Elliptical cylinder light collectors

(perpendicular to the axis defined by the ellipse) displacements from the focus of the ellipse. The results are shown in Figs. 2.13, 2.14, where ϕ is defined as in Fig. 2.12. The curves are labeled by the ratios of the minor to major axis of the ellipses. The transverse magnification can be positive or negative. As can be seen a more eccentric ellipse has higher magnification and the highest magnifications occur for angles less than ninety degrees. These regions of high magnification lead to large images at the second focus. This led to the geometry of Fig. 2.12b. The double ellipse system avoids the regions of high magnification and allows the two photomultiplier tubes to be run in coincidence giving further advantages that will be discussed in Chapter IV.

As can be seen from Figs. 2.13 and 2.14 a less eccentric ellipse has a lower magnification. To minimize the magnification it would seem that an ellipse with a very small eccentricity would be desired. However, as the ellipse is made more circular the area truncated at the second focus becomes larger. This area cannot gather light for the photomultiplier tubes, so the light gathering power of the ellipse is reduced. Some compromise must be reached between magnification and truncation effects. The ellipse constructed has a major axis of five inches, a minor axis of three inches and four inches between the foci. This gives a

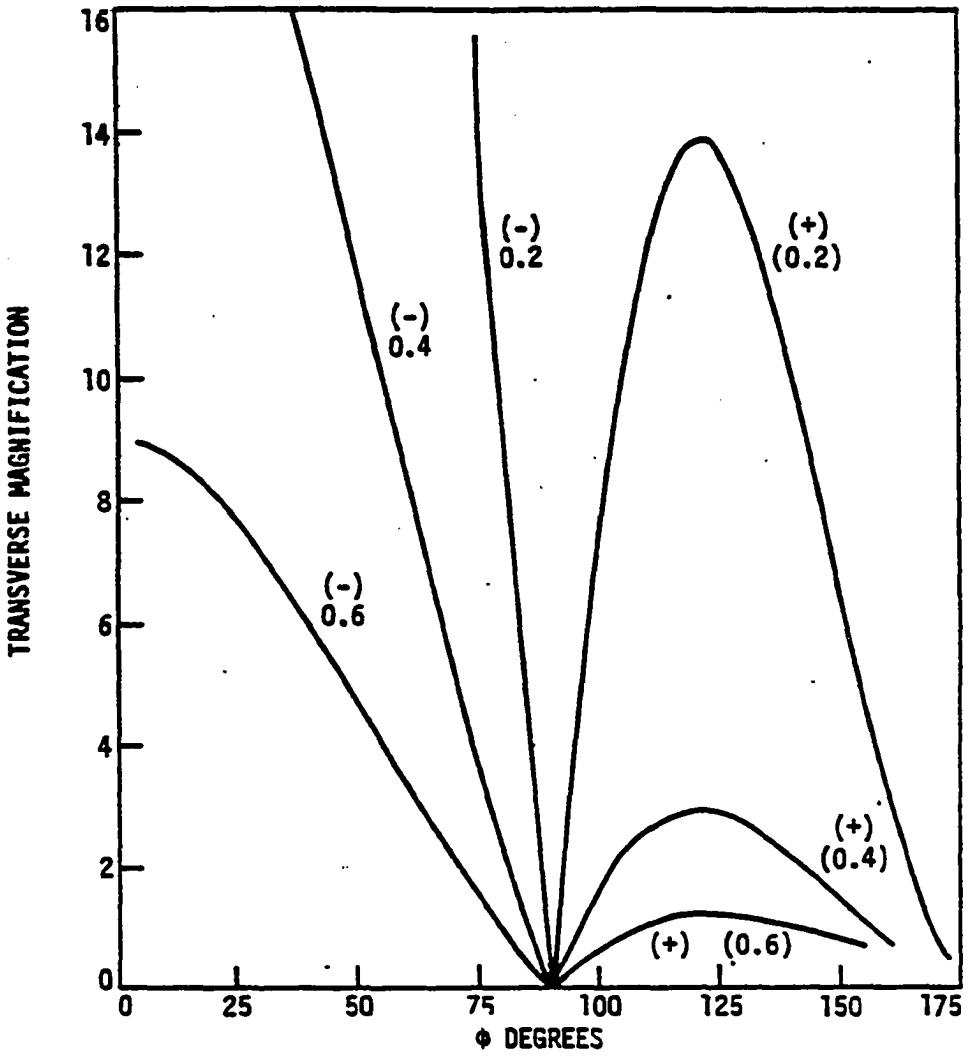

Figure 2.13 Transverse magnification for various ellipse geometries

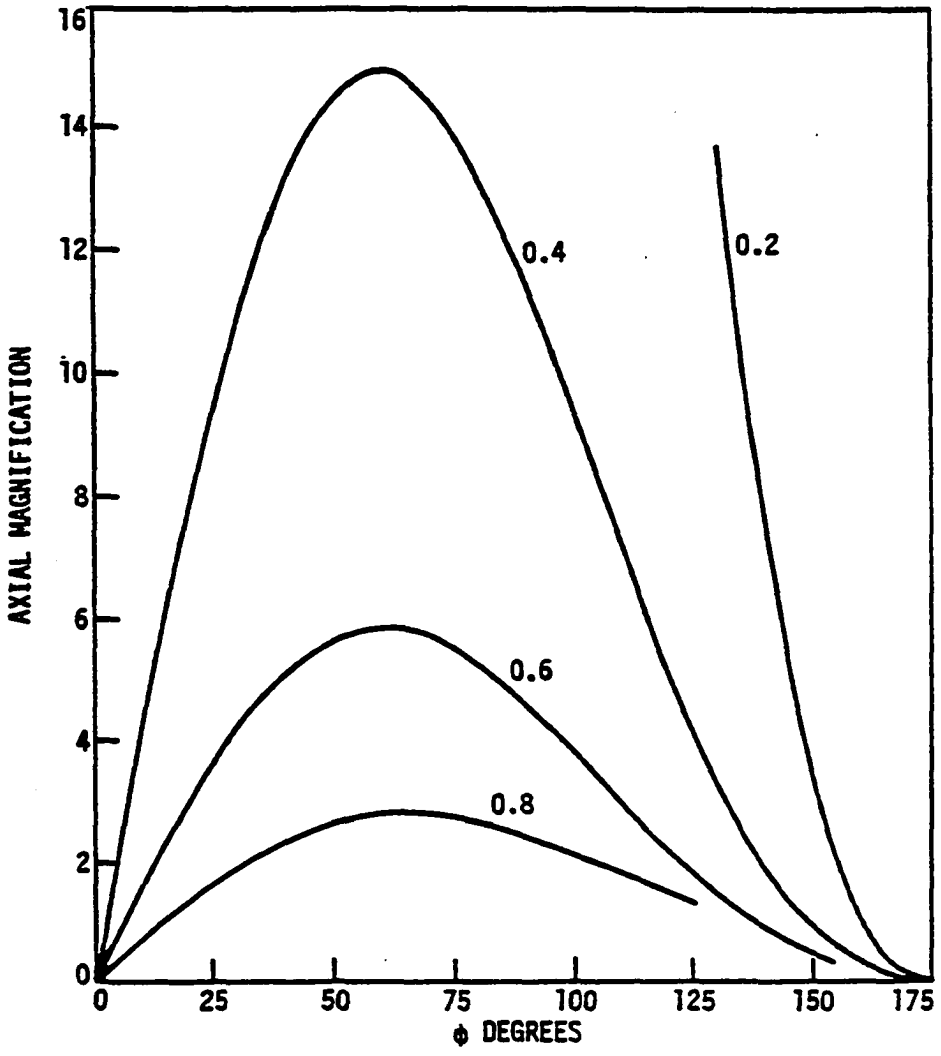

Figure 2.14 Axial magnification for various ellipse geometries

total loss due to the truncation effect of 14%, with a maximum magnification (axial) of 4.6. The elliptical cylinder was designed to fit into a four inch dependex multicross.

The light collector is one inch high with flat top and bottom reflecting plates. The distance d (Fig 2.12b) is .4 inches. The ellipse was cut back to minimize the scattering of incoming laser light. It is truncated at the second focus. The light collection efficiency depends on the angular distribution of the light given off at the focus. For randomly polarized laser light the resonantly scattered light is isotropic. For laser light which is linearly polarized along the atomic beam, the spatial distribution is proportional to $\sin^2\theta$ (with the z axis along the atomic beam). A third distribution of interest is that of a long thin cylindrical lamp, which emits light in a $\sin\theta$ pattern. The numerically calculated efficiencies of the elliptical light collector for these distributions are: isotropic, 40%; $\sin\theta$, 47%; $\sin^2\theta$, 49%, assuming a reflectivity of .96. The only distribution directly measurable is that of the lamp, which was found to be 34%. The discrepancy between the calculation and measurement may be due to basic imperfections in the light collector or to the finite size of the light detector used for the measurements. A three dimensional ray tracing program was used to calculate the

spatial and angular distribution of light leaving the ellipse which was scattered from the first focus. This program predicted 70% of the light scattered by a sinθ distribution which entered the ellipse will strike a 1.0 in dia. light detector positioned .1 in. from the second focus. This agrees well with the 72% (34%/47%) experimentally obtained. The light pipes used to transmit light to the photomultiplier tubes are larger (1.2 in. dia.) so that more of the light from the ellipses is captured by these pipes.

The efficiency of the photomultiplier tube-preamplifier discriminator electronics system was measured with red light from a He-Ne laser and found to be 7%. According to the manufacturer's specifications, the photomultiplier tube sensitivity should be 1.5 times greater with green light from the barium 5535 A transition.

The calculated efficiency for the ellipse when operating with a sinθ distribution is essentially the same as that of a $\sin^2\theta$ distribution. In tests of the light-pipe-photomultiplier tube combination the light detection efficiency with diverging He-Ne light was found to be 5% (55), as compared to 7% obtained with light normally incident on the photomultiplier tube alone. The light pipes have since been extended so this 5% efficiency should be viewed as a lower bound. The overall light collection and

detection efficiency of the system should be between the lower limit of 2.6% extrapolated from measurement [ε_m=(.34)(.05)(1.5)=2.6%] to the calculated value of 5% [ε_c=(.49)(.07)(1.5)=5.0%].

The laser beam optics used in this experiment are shown in Fig. 2.15a. The light is first spatially filtered with a commercial pinhole-telescope (Jodon LPSF 100) and expanded to the beam size required. In a coordinate system where X is along the laser beam, Z along the atomic beam and Y perpendicular to both, for the B and C distributions (see list below) the beam is focused to a line parallel to the Z axis one meter from the interaction region using a 4 m cylindrical lens. The beam is perpendicular to the atomic beam with the light rays parallel in the XZ plane. The 1/2 mm (A distribution) interaction region is produced with the addition of a second 4 m cylindrical lens which focuses the laser light in a line parallel to the Y axis at the atomic beam, minimizing the length of the interaction region. This arrangement makes the laser beam width much larger than the atomic beam diameter at the interaction region, which insures that all atoms experience the same laser power profile. The laser light profiles are approximately Gaussian with a half width at half maximum of $D_{1/2}$ (see below). The various beam sizes and total input powers used are given below.

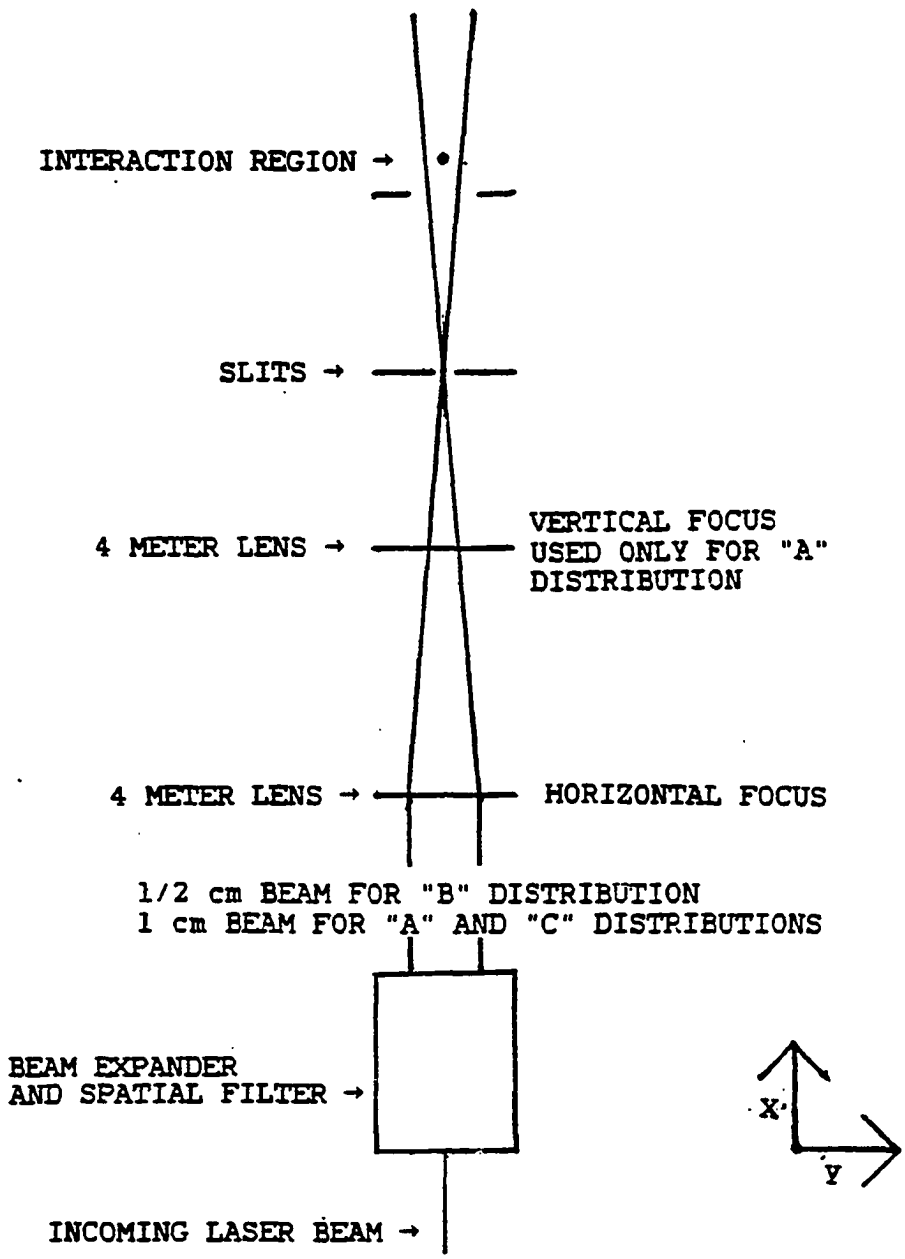

Figure 2.15a Laser beam optics system

Label	Interaction Length($D_{1/2}$)	Input Power
A1	.26 mm	.3 mW
A2	.26 mm	1.0 mW
A3	.26 mm	4.0 mW
B1	1.5 mm	1.25 mW
B2	1.5 mm	2.5 mW
B3	1.5 mm	5.0 mW
C1	2.8 mm	5.0 mW
C2	2.8 mm	10.0 mw
C3	2.8 mm	12.5 mW

The major source of background signal in this experiment is the laser light which is scattered from various surfaces inside the chamber and finds its way into the elliptical cylinder. To minimize background scattered light several adjustable slits with razor blade edges have been placed along the laser beam path (Fig. 2.15b). The incoming laser beam is normally focused in one dimension producing a one cm high ribbon of light inside the chamber. This beam passes through a window where it enters the chamber which is 30 cm upstream from the first slit. The beam is focused through the first slit (slit A). Since the lens being used is so weak (4 meter focal length) there is a long region of very narrow beam, making the exact placement of the focus not critical. It has been experimentally determined that a razor blade separation of 2.5-4 mm is optimum for this slit. If

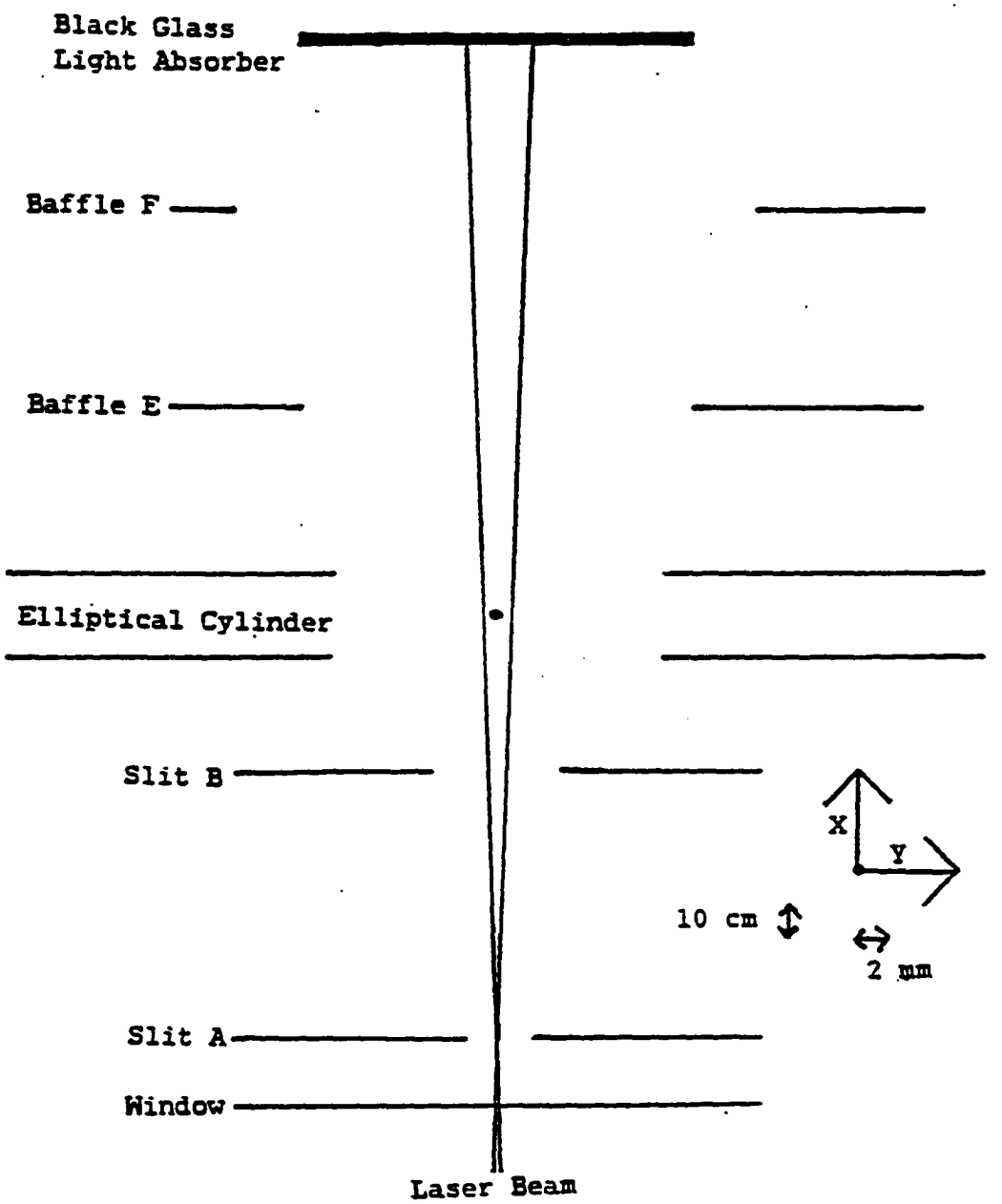

Figure 2.15b Slit System

this slit is opened wider than 4 mm, large numbers of photons produced by Rayleigh scattering in the entrance window are detected by the photomultiplier tubes. If the slit opening is less than 2.5 mm then the razor blades begin to scatter light. For slit openings between 2.5 and 4 mm there is no noticeable change in the background rate. To prevent light scattered by slit A from reaching the ellipse, a second slit (slit B) has been placed 80 cm away. The B slit opening which minimizes background is 8-10 mm wide. Again there is no difference in the background rate as long as the slit width is between these two limits. Slits A and B are constructed using commercial devices which consist of four mounts equally spaced about a four inch dependex beampipe. Razor blades attached to these mounts form the horizontal and vertical slits. The mounts are coupled to an external micrometer allowing quick and accurate adjustments to the slit separation even when the chamber is under vacuum. Unfortunately, due to the design of these devices it is not possible to close the vertical slits to less than 2 cm. The ellipse supports are made such that the background rate is much less sensitive to the vertical separation of the slits. While tests indicated that the background rate could be reduced a small amount by closing the vertical slits even further, this effect was small.

Epoxied directly onto the front of the elliptical cylinder are razor blades with a horizontal separation of 2.0 cm (slightly less than the 2.03 cm separation of the elliptical cylinders). These blades were found to have a dramatic effect, cutting the scattered light background rate by a factor of 4.5. The region between slit B and the ellipse seems to be extremely critical for light scattering because every adjustment in this region has a large effect. Increasing the distance of slit B to slit C by 8 cm raises the background rate by a factor of 3. Decreasing the distance by a similar amount also increases the background by a factor of three over the rate at the optimum position. After much work, it was found that the first distance tried was the optimum. It is not understood why the background rate is so sensitive to the B-C slit separation.

Downstream of the interaction region in the optics system are slits epoxied to the back of the elliptical cylinder and two light baffles (E opening 3.81 x 5.08 cm, F opening 5.08 X 5.08 cm) which prevent light scattered from the chamber walls from reentering the ellipse. Similar light baffles were placed between slits B and C but were removed after finding they greatly increased the background rate. At the end of the optics chain is a piece of light absorbing glass (Schott Glass RG1000) set at the Brewster angle for light with vertical polarization. This arrangement prevents

light from bouncing from the laser beam exit into the ellipse. The black glass was found to cut the background rate a factor of two over the previously used scheme, a window at the Brewster angle followed by a mirror which reflected the exiting laser light to a far wall.

With all of these components in the chamber, and with the interior of the chamber painted flat black the lowest background rate obtained for light from a He-Ne laser was 3500 counts/mw-sec.

Photon-Burst Counting Electronics

The heart of the signal processing in this experiment is the master counter. This coincidence counter acts as a multichannel rate analyzer grouping events by their count rates.

Pulses from the two photomultiplier tubes (Fig. 2.16), after being amplified and converted to TTL levels, are sent through an OR circuit connected to the input of the master counter. This counter contains a clock that controls the length of the counting interval. The first pulse in the event begins the counting interval and all additional counts received during the interval are included in the event. When the counting period ends the counter sends out a strobe pulse. This strobe enables the electronics which records the number of counts (multiplicity) in the event by incrementing the appropriate scaler. The counter then resets itself and

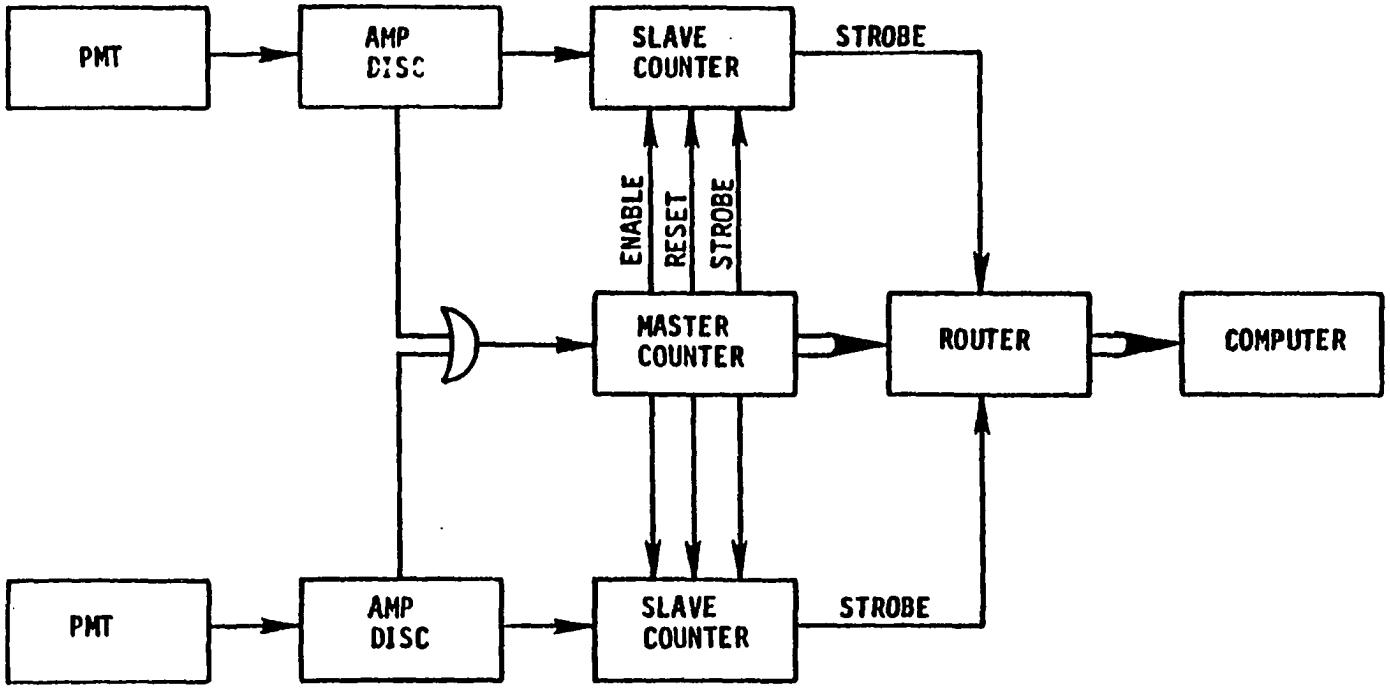

Figure 2.16 Photon burst counting electronics

is ready to receive another pulse and start the process over again.

The number of counts in an event is recorded by incrementing one of eight scalers. The master counter is connected to the scalers through a routing circuit. The strobe pulse sent from the counter signals the router that the counting is finished and causes it to increment the scaler corresponding to the multiplicity of the event. When the laser frequency is changed, the computer reads each scaler and adds the counts to the appropriate laser frequency bin with a separate spectrum recorded for each multiplicity.

The two phototubes are connected not only to the photon-master counter, but each tube is also connected to its own slave counter. The strobe pulse sent from the master counter must first pass through each slave counter before it reaches the router. The slave counters do not allow the strobe pulse to reach the router if a minimum number of counts have not been recorded by each counter. Counts must be received from both tubes before an event is recorded. The purpose of this scheme is to reduce background in spectra due to the autocorrelation in the dark counts of a single photomultiplier tube.

The master counter is capable of operating in two ways, one in which the counting time is fixed (Mode 1) and the

other in which the counting time is variable (Mode 2). Mode 1 operation is as described, a pulse starts the counting, the counting continues for a preset length of time and then stops. In Mode 2, as in Mode 1, a pulse begins the counting but each additional pulse received resets the timer extending the counting period. As long as a pulse is received before the timing interval ends, the counting period continues. In Mode 1, the timing interval is determined by the atomic-laser-beam transit time; in Mode 2 this interval depends upon the time between the detection of atom scattered photons. Mode 1 is used for short interaction regions and in situations where the atomic transit time is the same for all atoms, such as atoms from a helium jet. Mode 2 is most effective when the atoms have a wide range of transit times, such as in a thermal atomic beam.

CHAPTER III. PHOTON STATISTICS AND FLUORESCENCE LINESHAPES

Two-Level System and the Burst Method

It has been shown (21) for a source scattering photons at a constant rate R_e that the probability of scattering N photons in time T is

$$P(N)=[(R_eT)^N e^{-(R_eT)}]/N!. \qquad 3.1$$

The probability of detecting n of these N photons is given by the Bernoulli convolution

$$P(n)=\sum_{N=n}^{+\infty} \varepsilon^n (1-\varepsilon)^{N-n} \{[(R_eT)^N e^{-R_eT}]/N!\}\{N!/[n!(N-n)!]\}$$

$$=[(R_1T)^n e^{-R_1T}]/n! \qquad 3.2$$

where ε is the light detection efficiency and $\varepsilon R_e=R_1$. If an atom spends 10 μsec interacting with the laser light, and the photon detection rate (R_1) is 1 MHz, then the average number of detected photons per atom (R_1T) is 10. The probability of detecting n photons from this atom is

$$P(n)=[(10)^n e^{-10}]/n!.$$

Background counts from scattered laser light also follow the same statistics. If the background rate were 10,000/sec, then during a 10 μsec interval the probability of n background counts would be

$$P_b(n)=[(.1)^n e^{-.1}]/n!.$$

In this situation the rate of multiplicity n background

events would be

$$R_b(n)=9091\ [(.1)^n\ e^{-.1}]/n!.$$

The factor 9091 rather than 10,000 multiplies the probability due to a deadtime correction as will be explained in Chapter IV. If x atoms/sec were traversing the laser beam, the rate of obtaining n count events caused by atoms would be

$$R_a(n)=x\ [(10)^{10}\ e^{-10}]/n!$$

as long as the probability of more than one atom in the laser light at a time is small. The rate of background events with a multiplicity of 10 would be 2×10^{-13}/sec and the rate of counts from atoms would be .125(x).

The photon-burst method takes advantage of this strong dependence of probability on rate. When a photon is detected a clock is started and remains on for time T. All photons detected while the clock is on are included in this single event. The number of counts in the event, the multiplicity, provides a sorting mechanism. If there were only one count in the event, the one that started the clock, after the clock timed out the ones event bin would be incremented. If seven additional counts were received after the starting pulse during the counting interval, then one would be added to the eights bin. In the situation described in the previous paragraph (an atomic-transit time of 10 μsec) a clock time of 10 μsec would optimize the signal to noise

ratio. The probability of obtaining multiple counts in 10 μsec decreases much more rapidly for background light than for light from atoms. Only if the laser is tuned to an atomic resonance would events be present in high multiplicities.

The barium transition at 5535 A is suitable for photon-burst experiments. As can be seen in Fig. 3.1a, due to the small isotope shifts of barium, the signals from many stable barium isotopes are present in a very small region. The ^{138}Ba line was used for the experiment. The isotope ^{138}Ba is even-even so there are no hyperfine structure effects to be considered and it is separated from other lines better than transitions in the other abundant even-even isotopes. This isotope is the most abundant, so a small beam flux of ^{138}Ba insures an even smaller flux of other isotopes minimizing problems with the overlap of the Lorentzian tails of the lineshapes. The frequency region scanned in the experimental runs corresponds to channels 125-285 in Fig. 3.1a. Photon-burst spectra of this transition with a tenuous atomic beam are shown in the next few figures. In Fig. 3.1b, the twos (all events which consisted of two counts) are shown. There is no evidence of an atomic resonance in this frequency region. Fig. 3.1c shows the threes. The background has dropped and two peaks have appeared. Moving on to the sevens, the background has fallen

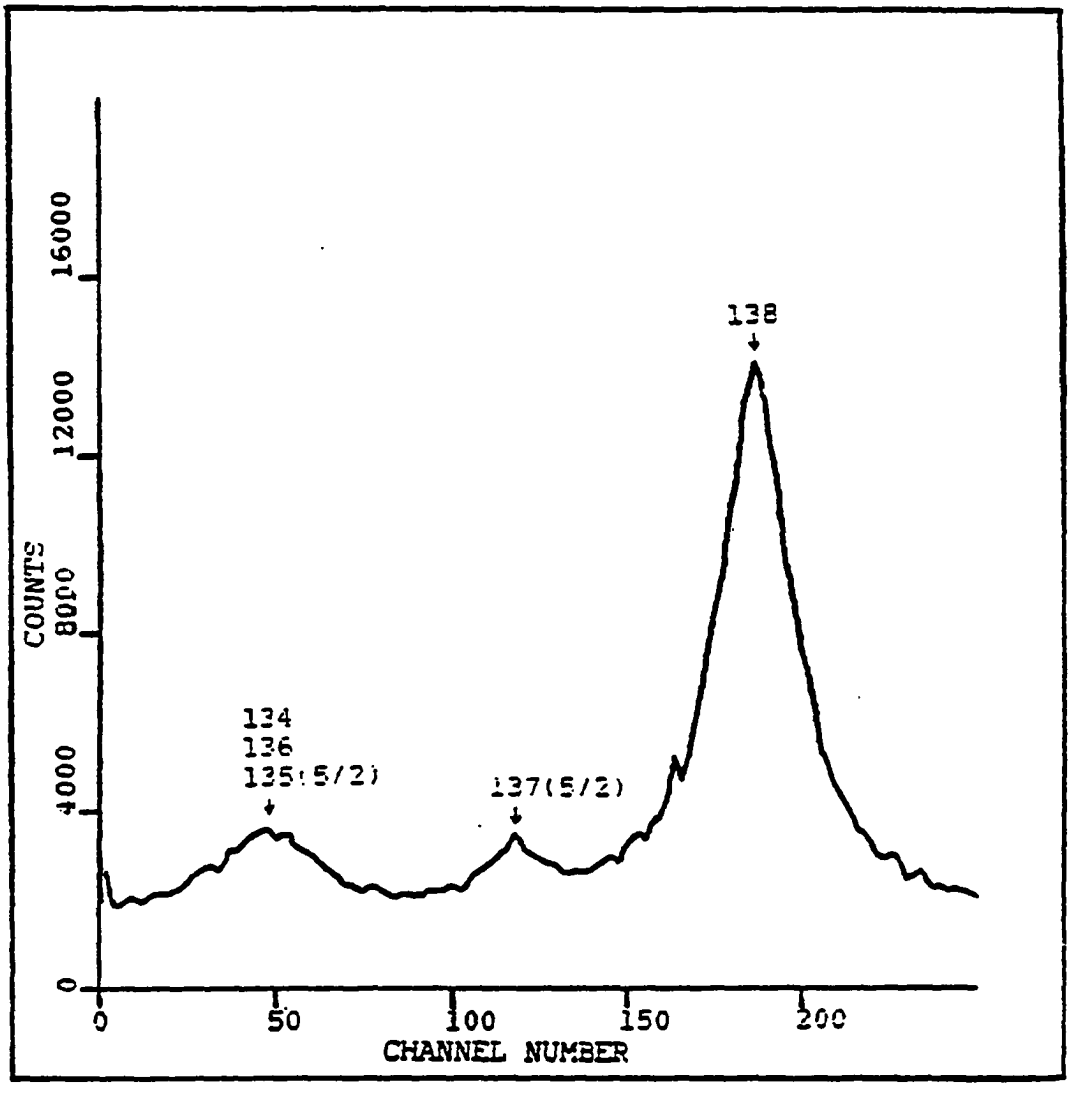

Figure 3.1a Spectrum of barium isotopes for λ=5535A transition. The scan width used in this experiment was from channel 125-285. Each channel number is .911 MHz

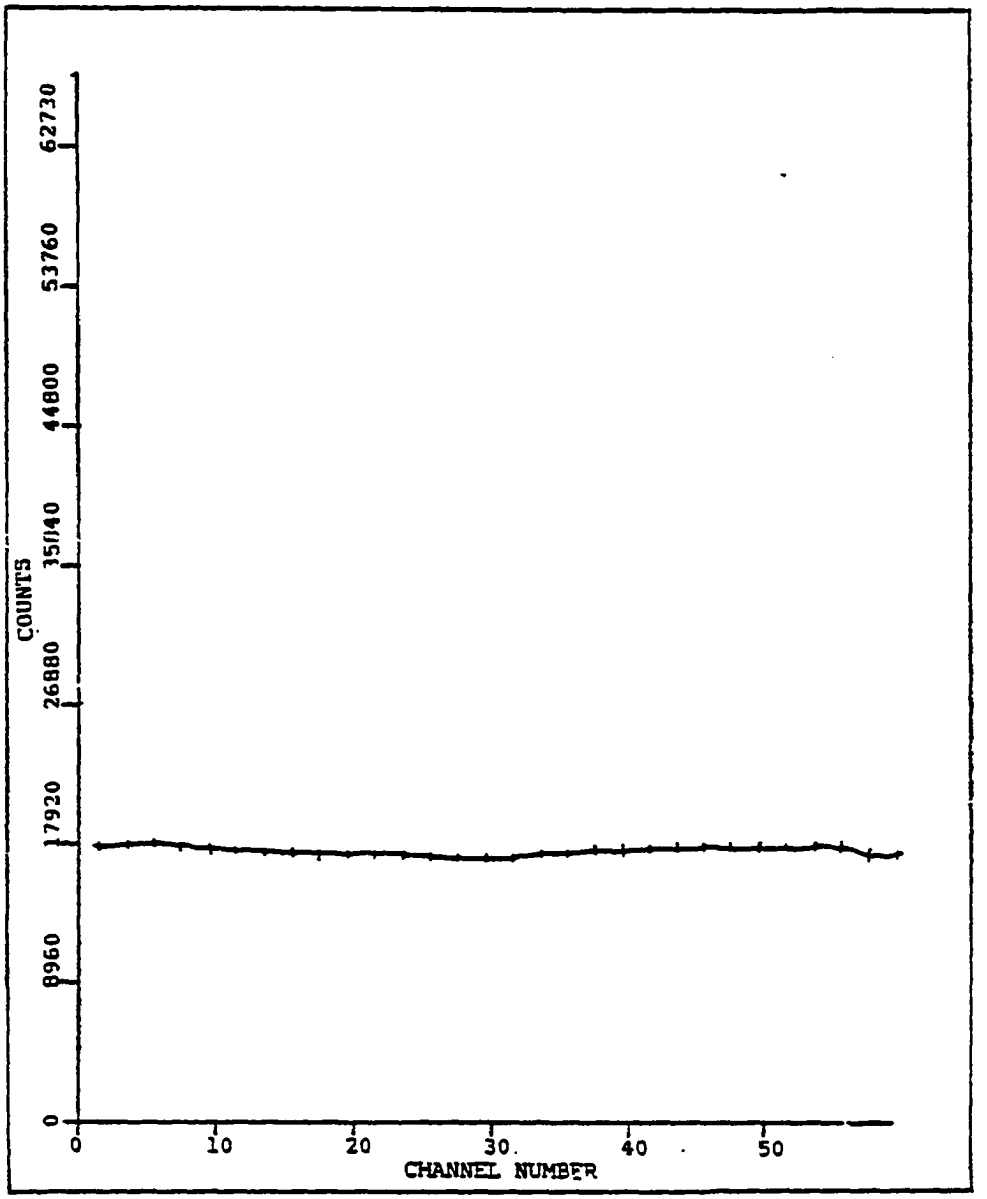

Figure 3.1b Multiplicity 2 spectra. The scale is 2.29 MHz/channel

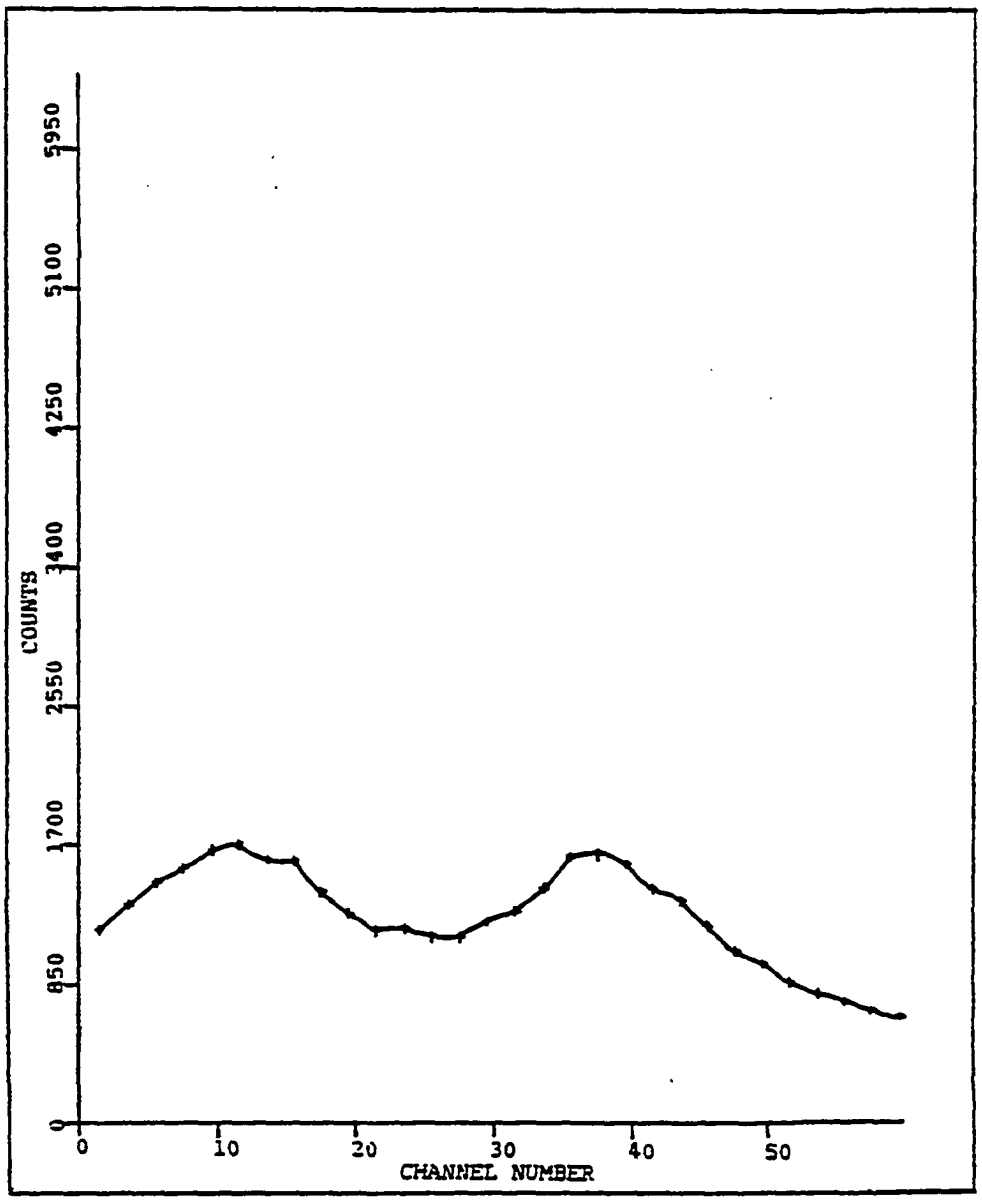

Figure 3.1c Multiplicity 3 spectra

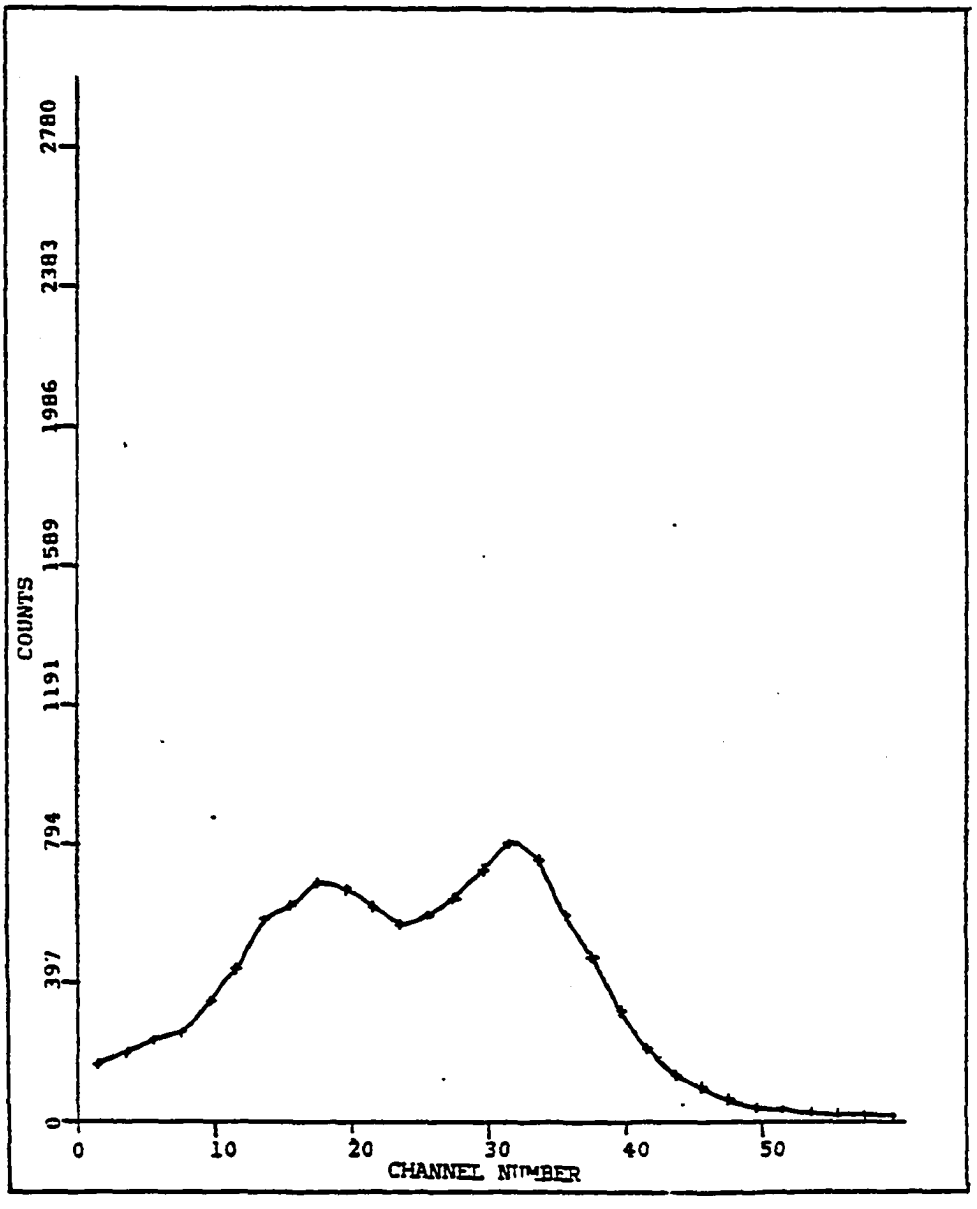

Figure 3.1d Multiplicity 7 spectra

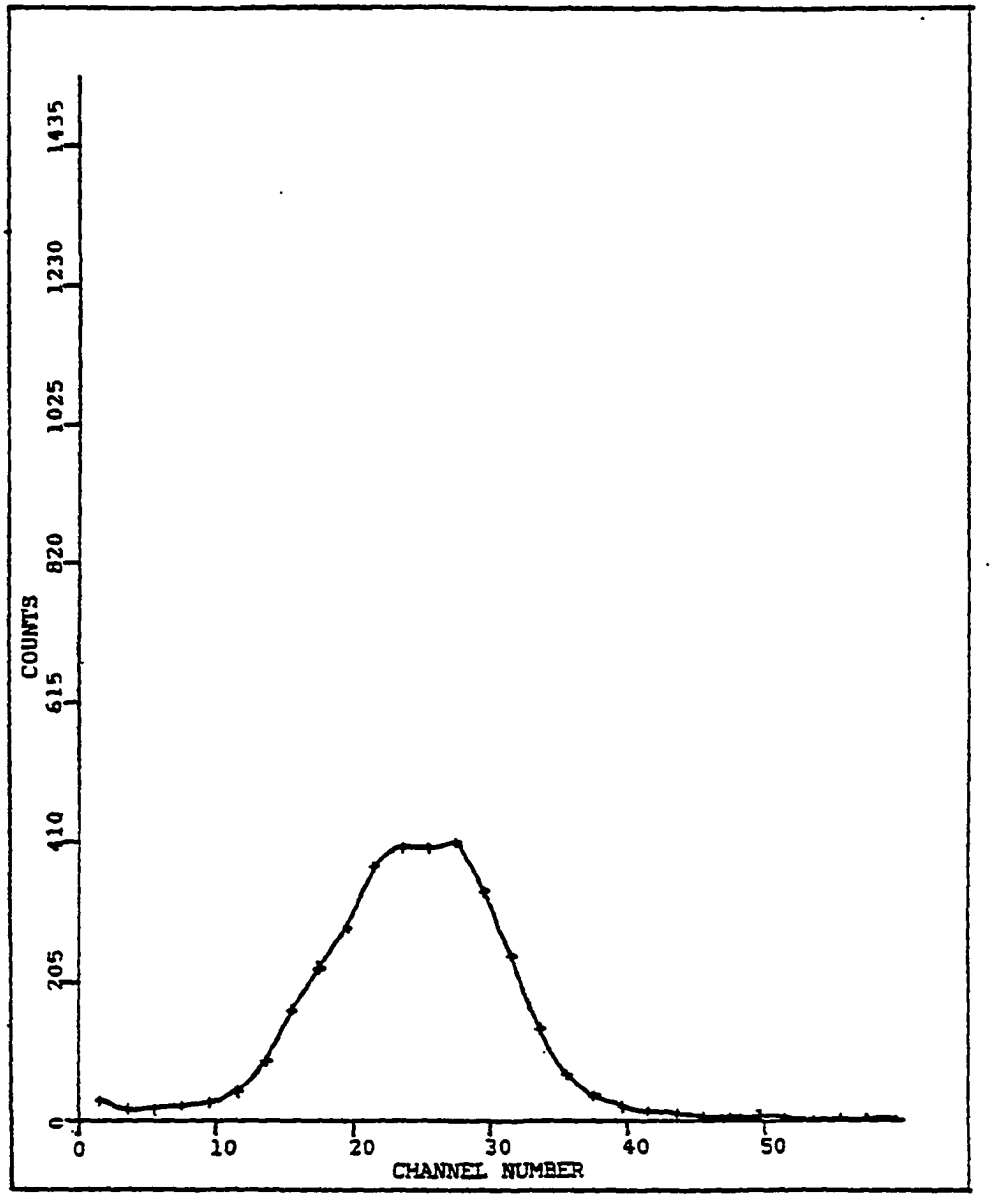

Figure 3.1e Multiplicity 12 spectra

considerably. The resonance consists of two closely spaced peaks, the separation of which is smaller than in the threes and the overall structure has narrowed. In the twelves, the background is zero, and the resonance consists of a single narrow peak. This behavior will be qualitatively discussed and equations derived for a quantitative description in this chapter.

In the derivation of eq. 3.1 (21), the detection of a photon at time t_1 was assumed to have no effect on the probability of the detection of a photon at a later time t_2. This is not strictly true for either background or atom scattered light. Background light should exhibit bunching, i.e., more high multiplicity background events should be received than predicted by Poisson statistics. Light scattered from atoms is anti-correlated in time, i.e., detection of a photon at time t_1 lowers the probability of detecting a second photon immediately after the first.

The photon bunching of the background light, known as the Hanbury-Brown Twiss effect (56), is due to the finite frequency width of the light source. Different frequency components of the laser interfere with one another, causing an overall amplitude modulation of the laser output. The frequency of modulation is on the order of the inverse of the frequency spread of the laser (57). The laser instantaneous FWHM is approximately 1 MHz, so the photons

would be expected to bunch on the time scale of 1 μsec (22). The photon-burst clock time setting would need to be shorter than 1 μsec for this effect to become apparent. The counting times used in this work were much longer than this, so the bunching would be averaged over many cycles. Because of this, no deviations from Poisson statistics should be apparent in the background.

After a two-level atom emits a photon it is in its ground state. Before the atom can emit another photon, it needs to be raised to an excited state. The time delay between the emission of a photon and the subsequent excitation is the mechanism for anti-bunching. The effect of this on the photon number distribution has been calculated (18, 19, 20) and the results are functions much more complicated than the Poisson distribution. Exactly at resonance the photon number distributions which include photon anti-bunching are narrower than the Poisson distribution with fewer high and low multiplicity events than would be expected with Poisson statistics. The deviation from Poisson statistics is characterized by the Q, the second factorial moment,

$$Q=(\langle(\Delta n)^2\rangle-\langle n\rangle)/\langle n\rangle \qquad 3.3$$

where $\langle n\rangle$ is the average number of photons scattered and $\langle(\Delta n)^2\rangle$ is the variance of the photon number distribution. The parameter Q is zero for the Poisson distribution,

negative for a sub-Poissonian distribution and positive for a super-Poissonian distribution. The calculations of Cook, Lenstra and Mandel are of atom scattered photon number distributions, not detected photon number distributions. It has been shown (20, 22) that the second factorial moment for the detected photon distribution is given by $Q'=\varepsilon Q$ where ε the system light collection efficiency. The approximately 3% light detection efficiency of the apparatus used in this work implies the difference from Poisson statistics is very small. In the development of the photon number distributions for the three-level system two-level photon statistics are assumed to be Poisson.

Photon Number Distributions in a Three-Level System

In the barium 5535 A transition the excited 6s6p $^1P_1$ state can decay either to the $6s^2\ ^1S_0$ ground or to the metastable 6s5d $^1D_2$ state. The transit time of an atom through the laser beam is on the order of tens of μsec and the lifetime of the metastable state is several msec (24). Once an atom decays into this state it is lost for photon scattering purposes. The number of photons is limited either by the atom leaving the laser light (as in the previously discussed two-level system) or by a branch to the metastable state. This pumping of atoms changes the probability distribution of the detected photons. If R_1 is the rate of detected photons then the probability of n detected photons with no branching in time t is

$$P(n,t)=[(R_1t)^n e^{-R_1t}]/n!. \qquad 3.4$$

If R_2 is the rate at which atoms decay into the metastable state the probability/unit time for this decay is $P(t)=R_2e^{-(R_2t)}$. The probability for a three-level atom to scatter n photons is then

$$P_{3L}(n,T)=\int_0^{+\infty}P(n,t)P(t)dt=\int_0^{T}P(n,t)P(t)dt+\int_T^{+\infty}P(n,t)P(t)dt \qquad 3.5$$

where T is the atomic transit time. The $T\to+\infty$ integral represents atoms that have left the laser beam without being optically pumped. The probability of an atom surviving this interval without being optically pumped is $e^{-(R_2T)}$, and the corresponding probability of emitting n photons is

$$P(n,t)=P(n,T)=[(R_1T)^n e^{-R_1T}]/n!, \qquad 3.6$$

for $t\geq T$. The second integral becomes

$$\int_T^{+\infty}P(n,t)P(t)dt=[(R_1T)^n e^{-RT}]/n! \qquad 3.7$$

where $R=R_1+R_2$. The first term in eq. 3.5 represents the probability distribution for those atoms which are pumped into the metastable state within time T and is equal to

$$\int_0^{T}P(n,t)P(t)dt=(R_1/R)^n(R_2/R)^n\{1-\Sigma_{k=0}^{n}[(RT)^k e^{-RT}]/k!\}. \qquad 3.8$$

The total probability distribution is

$$P_{3L}(n,T)=[(R_1T)^n e^{-RT}]/n! + [R_1/R]^n [R_2/R] [1-e^{-RT} \sum_{k=0}^{n} (RT)^k/k!]. \quad 3.9$$

An important quantity in the characterization of a probability distribution is

$$\langle n\rangle=\sum_{n=0}^{+\infty} n\, P(n) \quad 3.10$$

the average value of n. For a two-level system this is given by

$$\sum_{n=0}^{+\infty} n\, P(n) = \sum_{n=0}^{+\infty} n\, [(R_1\, T)^n e^{-R_1T}]/n! = R_1T, \quad 3.11$$

and in the three-level case

$$\langle n\rangle = \sum_{n=0}^{+\infty} n\, P_{3L}(n) = (R_1/R_2)(1-e^{-R_2T}). \quad 3.12$$

The rates R_1 and R_2 are equal to $(1-x)\varepsilon R_e$ and xR_e respectively where x is the fraction of decays that go to the metastable state. If $\gamma=R_1/R_2= \varepsilon(1-x)/x$, then $\langle n\rangle$ can be written as

$$\langle n\rangle=\gamma(1-e^{-R_1T/\gamma}). \quad 3.13$$

This parameter γ is also the average number of detected photons in the optical pumping limit ($R_1T\rightarrow +\infty$) and plays an important role in this work. The quantity x is assumed to be much less than one so that $R_1=\varepsilon R_e$ and $\gamma=\varepsilon/x$.

Alternatively the situation can be viewed as follows. If either a detected photon or a decay which branches to the metastable state is an event, then $[(RT)^n e^{-RT}]/n!$ is the probability of n events. The probability that an event is a detected photon is $\gamma/(1+\gamma)$, and the probability the event is a branch is $1/(1+\gamma)$. There are two ways that n photons can be detected: there can be exactly n events, all of which are detected photons, or there can be at least n+1 events in which the first n are detected photons and the (n+1st) is a branch. The probability of the first case is $[(RT)^n e^{-RT}]/n!$ (the probability of n events) times $[\gamma/(1+\gamma)]^n$ (the probability that all events are detected photons). In the second case, the probability of at least n+1 events is $\Sigma_{k=n+1}^{+\infty} [(RT)^k e^{-RT}]/k!$, and the probability of exactly n detected photons followed by a branch is $[\gamma/(1+\gamma)]^n[1/(1+\gamma)]$. After branching, no photons can be detected, and therefore all the events of multiplicity n+1 and greater must be included. This again implies

$$P_{3L}(n,T)=[(R_1T)^n e^{-RT}]/n! + [\gamma/(1+\gamma)]^n [1/(1+\gamma)][1-e^{-RT}\sum_{k=0}^{n}(RT)^k/k!]. \quad 3.9$$

In eq. 3.9, R is a constant in the laser-atom interaction region. The laser beam profile used in the experiment is not constant, so the scattering rate is also not constant. As the atom moves through the beam its

scattering rate is $R_e(t)$. For time dependent rate distributions, such as this, it has been shown (21) that the probability of n events is

$$P(n)=[R_I(t_1,t_2)^n \; e^{-R_I(t_1,t_2)}]/n!, \qquad 3.14$$

$$R_I(t_1,t_2)=\int_{t_1}^{t_2} R_e(t)\,dt$$

where t_1 is the time the interaction starts and t_2 is the time it ends.

The rate of spontaneous emission, for the laser tuned to the resonant frequency of the transition (19), is

$$R_e=A\,(\Omega^2/A^2)/(1+2\,\Omega^2/A^2)$$

where Ω is the Rabi frequency parameter and A is the Einstein spontaneous emission coefficient. The Rabi parameter is

$$\Omega= 2\pi\langle u|\bar{x}|1\rangle\cdot\bar{E}/h \qquad 3.15$$

where $\langle u|\bar{x}|1\rangle$ is the dipole matrix element of the transition and $\bar{E}$ is the electric field strength of the exciting field. The dimensionless parameter Ω^2/A^2 is equal to KI, where K depends on the particular atomic transition and I is the laser intensity.

The actual laser intensity distribution along the atomic beam is approximately a Gaussian profile. The spontaneous emission rate can be written as

$$R_e(z)=A\,KI_0e^{-(z/D)^2}/(1+2KI_0e^{-(z/D)^2}) \qquad 3.16$$

where $[A\ KI_0/(1+2KI_0)]$ is the light scattering rate at the center of the laser beam (z=0) and D is the distance from the center of the interaction region to the 1/e points of the Gaussian. In terms of the dimensionless quantity

$$\bar{O} = (1/D)\int_{-\infty}^{+\infty} [KI_0 e^{-(z/D)^2}/(1+2KI_0 e^{-(z/D)^2})]\,dz$$

$$= \int_{-\infty}^{+\infty} [KI_0 e^{-y^2}/(1+2KI_0 e^{-y^2})]\,dy \qquad 3.17$$

the average rate $\langle R\rangle=\langle R_1\rangle+\langle R_2\rangle$ is defined as $(\varepsilon+x)A\,\bar{O}$. If the atom has velocity v perpendicular to the laser beam then

$$R(t)=(\varepsilon+x)[A\ KI_0 e^{-(vt/D)^2}/(1+2KI_0 e^{-(vt/D)^2})] \qquad 3.18$$

$$\int_{-\infty}^{+\infty} R(t)dt=(\varepsilon+x)A\int_{-\infty}^{+\infty} [KI_0 e^{-(vt/D)^2}/(1+2KI_0 e^{-(vt/D)^2})]dt$$

$$=(D/v)(\varepsilon+x)A\int_{-\infty}^{+\infty} [KI_0 e^{-y^2}/(1+2KI_0 e^{-y^2})]\,dy$$

$$= (D/v)\ (\varepsilon+x)\ A\ \bar{O}$$

$$= (D/v)\ \langle R\rangle. \qquad 3.19$$

From equations 3.14 and 3.19, the probability of n events with the rate varying is

$$P(n)= [(\langle R\rangle D/v)^n e^{-D\langle R\rangle/v}]/n!. \qquad 3.20$$

Using eq. 3.20 in eq. 3.9, the probability of n detected photons in this case is

$$P_{3L}(n,v)=(\{[\gamma/(1+\gamma)]\langle R\rangle D/v\}^{n} e^{-\langle R\rangle D/v})/n! + [\gamma/(1+\gamma)]^{n}[1/(1+\gamma)][1-e^{-\langle R\rangle D/v}\sum_{k=0}^{n}(\langle R\rangle D/v)^{k}/k!]. \quad 3.21$$

The atoms in a thermal atomic beam do not all have the same velocity, but have the distribution (58)

$$P(v)dv=2(2K_bT_e/m)^{2} v^{3} e^{-(mv^2/2K_bT_e)} dv, \quad 3.22$$

where K_b is the Boltzman constant, and T_e is the temperature of the oven. The three-level probability distribution must be averaged over the atomic velocity distribution to be compared to experiment.

$$P_{3L}(n)=\int_{-\infty}^{+\infty} P(v)P_{3L}(n,v)\,dv \quad 3.23$$

Define $\langle T\rangle=D\langle 1/v\rangle$, where $\langle 1/v\rangle=\int_{-\infty}^{+\infty}P(v)/v\,dv$, and let $\alpha=v\langle 1/v\rangle$. Then $P_{3L}(n)$ is given by

$$P_{3L}(n)=(32/\pi^2)\int_{0}^{+\infty} \alpha^{3} e^{-\pi\alpha^2/4} d\alpha\{(1/n!)(\langle R_1\rangle\langle T\rangle/\alpha)^{n} e^{-\langle R\rangle\langle T\rangle/\alpha} + [\gamma/(1+\gamma)]^{n}[1/(1+\gamma)][1-e^{-(\langle R\rangle\langle T\rangle/\alpha)}\sum_{k=0}^{n}(\langle R\rangle\langle T\rangle/\alpha)^{k}/k!]\}. \quad 3.24$$

The quantity $\langle R_1\rangle$ is equal to $[\gamma/(1+\gamma)]\langle R\rangle$, which is the average rate of detected photons in the absence of optical pumping. The three-level probability distribution is completely characterized by two quantities, $\langle R_1\rangle\langle T\rangle$ and γ.

In the event $\gamma\to+\infty$ (indicating there is no branching) eq. 3.23 reduces to

$$P_{2L}(n)=(32/\pi^2)\int_0^{+\infty}\alpha^3 e^{-\pi\alpha^2/4}\,d\alpha\{(1/n!)[\langle R_1\rangle\langle T\rangle/\alpha]^n e^{-\langle R_1\rangle\langle T\rangle/\alpha}\}. \qquad 3.25$$

This is the probability distribution of a two-level system averaged over velocity (43).

Photon probability distributions (eq. 3.24) are shown in Fig. 3.2. The lower multiplicities are dominated by those atoms that have been optically pumped. As the excitation rate increases, the likelihood that the atoms will be optically pumped increases. This causes the distribution to tend toward a simple power law, i.e.,

$$\lim_{\langle R_1\rangle\langle T\rangle\to+\infty} P_{3L}(n)=[\gamma/(1+\gamma)]^n[1/(1+\gamma)]. \qquad 3.26$$

The lower multiplicities are the first to show this behavior. Unfortunately these also have the highest background, which makes the interpretation more difficult.

In summary, the three-level probability distribution depends only on $\langle R_1\rangle\langle T\rangle=[\gamma/(1+\gamma)]\langle R\rangle\langle T\rangle$, the average number of detected photons in the transit time limit, and γ, the average number of detected photons in the optical pumping limit. The most general expression is eq. 3.24, and the two limiting cases are eq. 3.25 and 3.26.

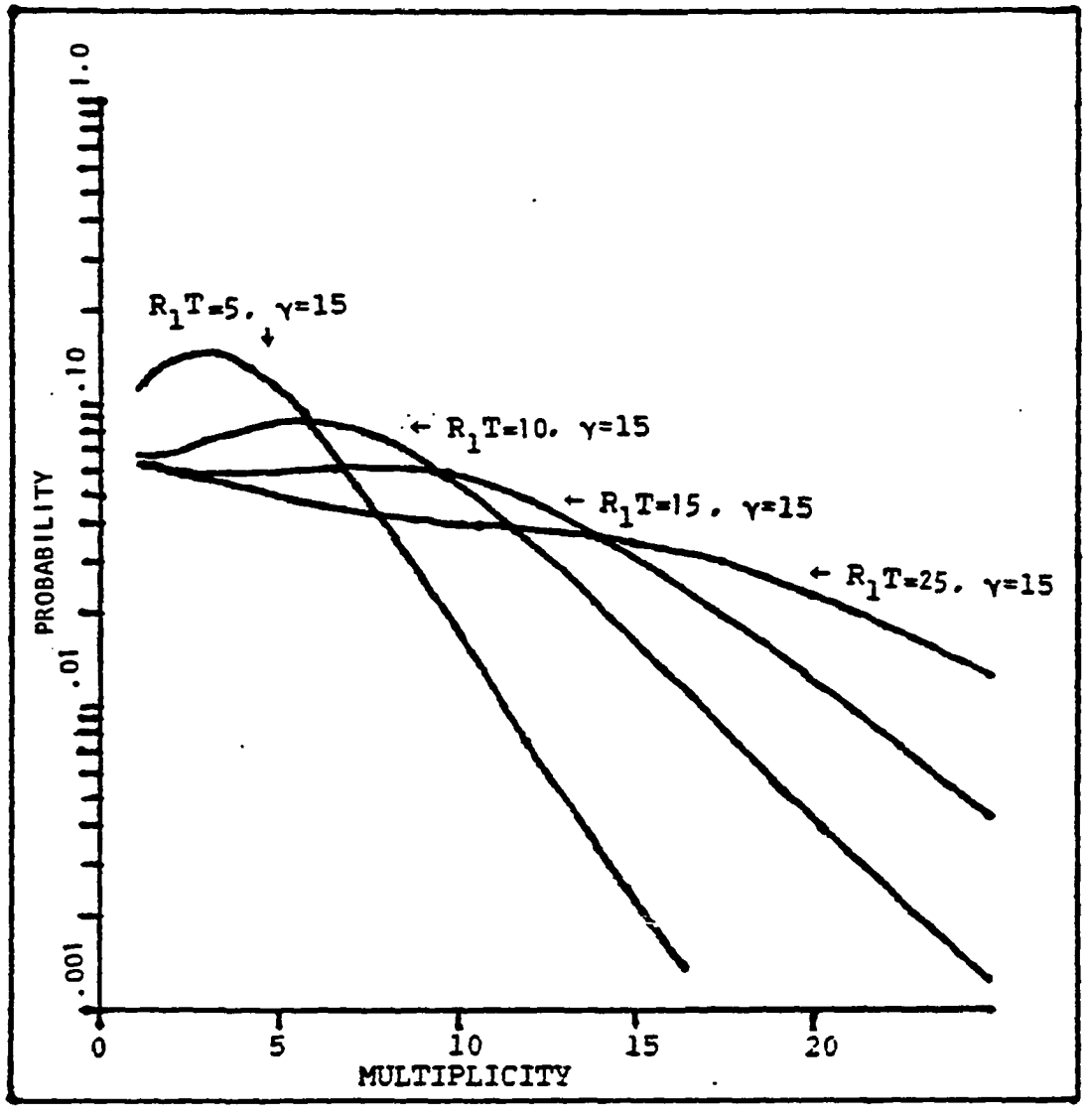

Figure 3.2a Photon number distributions for various values of R_1T and γ

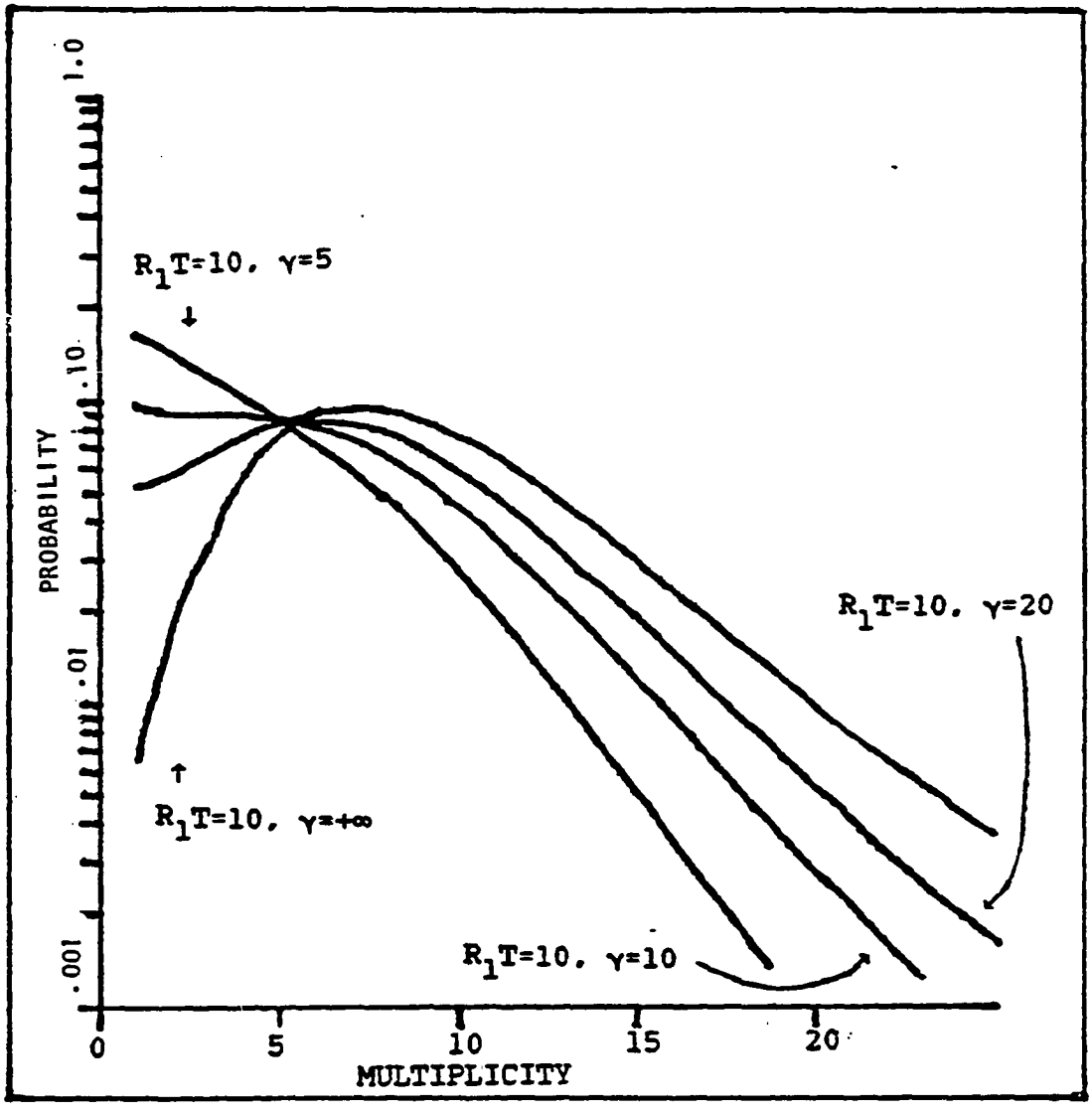

Figure 3.2b Photon number distributions for various values of R_1T and γ

Q Parameters

For a Poisson distribution, the second factorial moment, Q_p, is zero. For an optical-pumping-limited system this parameter can be shown to be

$$Q_{op}=\gamma. \tag{3.27}$$

Using eq. 3.9, Q for a three-level system is

$$Q_{3L}= \frac{\gamma[1-e^{-(2R_1T/\gamma)}] - 2R_1T\, e^{(-R_1T/\gamma)}}{[1 - e^{(-R_1T)}]} \tag{3.28}$$

assuming a constant atomic transit time. If $R_1T<<\gamma$, the three-level distribution approaches the Poisson limit,

$$\lim_{R_1T\to 0} Q_{3L} =0 \tag{3.29}$$

and if $R_1T>>\gamma$ the photon number distribution approaches the optical-pumping limit

$$\lim_{R_1T\to+\infty} Q_{3L} = \gamma \ . \tag{3.30}$$

In Fig. 3.3 eq. 3.28 is graphed for various values of R_1T and γ. The γ=5 curve saturates at value of Q_{3L}=5 as expected. The Q_{3L} values for higher values of γ are close to zero for relatively large values of R_1T, indicating that the distributions correspond to the Poisson distribution for these values of R_1T and γ, also as expected.

If the atom transit time is not a constant the Q parameters of the distributions are changed. A Poisson distribution averaged over a thermal atomic-beam velocity

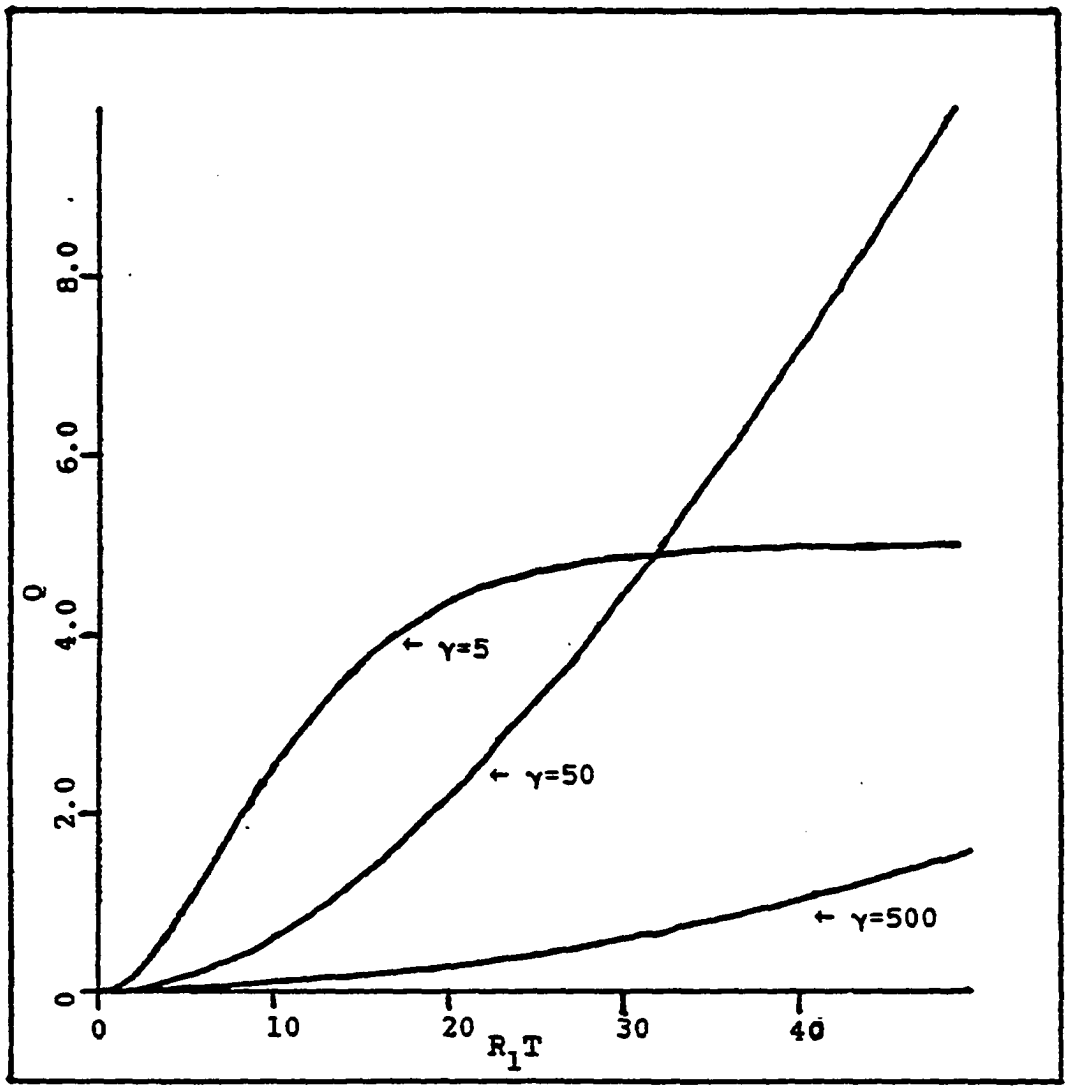

Figure 3.3 Second factorial moments for a three level system vs. photon scattering rate for γ=5, 50, 500, for fixed transit time

distribution (eq. 3.22) has a Q parameter of

$$Q_{pT} = (4/\pi - 1)\, R_1 T.$$
$$\cong .273\, R_1 T \qquad 3.31$$

which is a linear function of the number of detected photons. An optically-pumped distribution is independent of transit-time effects, so

$$Q_{opT}=Q_{op}=\gamma. \qquad 3.32$$

For the intermediate case, Q_{3L} averaged over velocity is

$$Q_{3LT}= \frac{\gamma(1- \langle e^{-R_1 T/\gamma\ 2} \rangle)- \langle R_1 T e^{-R_1 T/\gamma} \rangle}{(1 - \langle e^{-R_1 T} \rangle)} \qquad 3.33$$

where $\langle\ \rangle$ denotes an average over the transit times across the laser beam again assuming the velocity distribution given in eq. 3.22. Graphs of Q_{3LT} vs. R_1T for four values of γ shown in Fig. 3.4. Also plotted is Q_{pT}. The Q vs. R_1T curves for the two different cases have different shapes, but show the same behavior: for $R_1T \ll \gamma$, Q_{3LT} approaches the Poisson limit, and for $R_1T \gg \gamma$, Q_{3LT} saturates at γ. An interesting reversal from the fixed transit time case occurs in that the velocity-averaged Poisson distribution is wider than the corresponding three-level photon number distribution. The difference in Q parameters of the three-level distribution from the two-level distribution is not large for large values of γ. For the experimental distributions in this work the Q values obtained are also

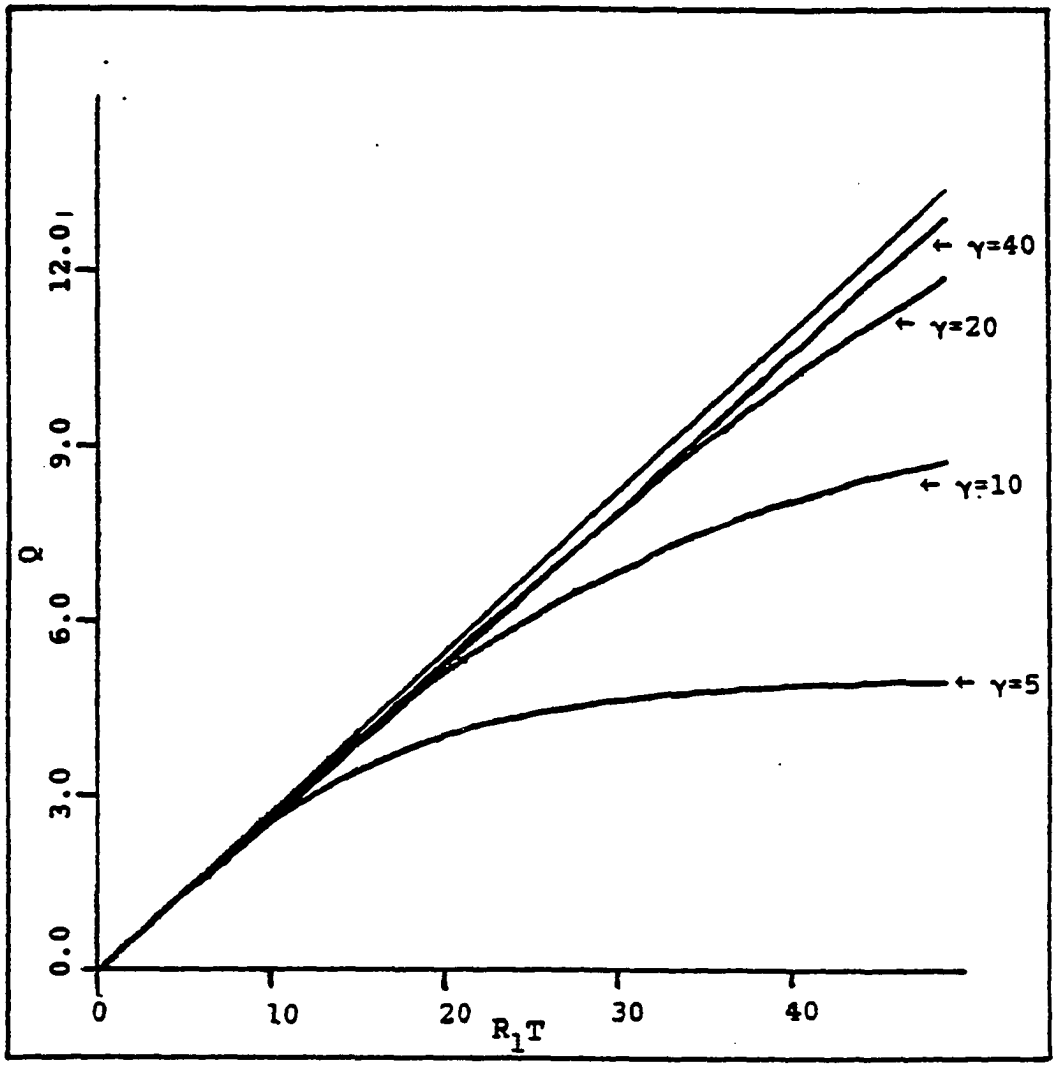

Figure 3.4 Second factorial moments for a two level system ($\gamma=+\infty$), and for three level systems with $\gamma=5$, 10, 20, 40

affected significantly by the truncation effects of recording only multiplicities less than 31. The quantity Q is not a good parameter to use in characterizing experimental differences between two-level and three-level systems if the atomic light scattering statistics were obtained using a thermal atomic beam.

Lineshape Calculations

Total resonance fluorescence lineshapes for two-level atoms

As an atom moves through the laser beam the absorption of photons changes its velocity. The rate of change of the atomic momentum along the laser, assuming that the net momentum carried by spontaneous emission is zero, is

$$dp/dt = (h\nu/c)\, R_e(t), \qquad 3.34$$

where $R_e(t)$ is the spontaneous emission rate. This is given by (Coo 80),

$$R_e(t) = A\Omega^2/[4(\Delta - 2\pi\nu v_L(t)/c)^2 + A^2 + 2\Omega^2] \qquad 3.35$$

where Ω is the Rabi frequency, $\Delta = \omega - \omega_0$, the angular frequency difference between the laser and the atomic resonance, A is the Einstein spontaneous emission coefficient, and $v_L(t)$ is the atomic velocity along the laser beam. Rewriting this as

$$R_e(t) = A\,(\Omega^2/A^2)/[(4/A^2)(\Delta - 2\pi\nu v_L(t)/c)^2 + 1 + 2\Omega^2/A^2]. \qquad 3.36$$

The ratio Ω^2/A^2 is recognized as KI, the previously used saturation parameter. If Λ is defined as

$$\Lambda=\frac{1}{A}\left[\frac{2\pi\nu v_L(t)}{c}-\Delta\right] \qquad 3.37$$

then $d\Lambda/dt=(2\pi\nu/Ac)dv_L/dt = (2\pi\nu/A)\, d\beta/dt$, where $\beta=v_L/c$. From (3.34) it follows that

$dp/dt= (h\nu/c)\, A\, KI/(4\Lambda^2 +1+ 2KI)$, and 3.38a

$d\beta/dt= 1/mc\ dp/dt.$ 3.38b

Using 3.37 and 3.38b to solve for Λ in terms of laser beam intensity,

$d\Lambda/dt=(2\pi\nu/Amc)\ dp/dt$, and substituting for dp/dt, 3.38c

$d\Lambda/dt=(2\pi h\nu/mc^2)\nu\ KI/(1+2KI+4\Lambda^2)$. 3.38d

Define α_ν as $(2\pi h\nu/mc^2)\nu$. Rearranging terms and integrating yields

$4/3\ [\Lambda^3(t)-\Lambda^3(t_0)]+(1+2KI)[\Lambda(t)-\Lambda(t_0)]=\alpha_\nu\ KI(t-t_0)$ 3.39

where $\Lambda(t)$ is the value of Λ at time t. The parameter $\Lambda(t)=(2\pi\beta(t)\nu-\Delta)/A$ is proportional to the angular frequency difference between the resonant frequency and the laser frequency as a function of time.

The laser beam profile is not constant throughout the interaction region, but is given by

$$KI(z)=KI_0 e^{-(z/D)^2}. \qquad 3.40$$

The changing laser beam intensity must be taken into account to find the shift in the resonant frequency. Instead of using the continuous distribution, the laser profile can be approximated by N cells of equal width, such that I_n is a constant in each cell, i.e.,

$$KI_n = KI_0 e^{-(n/N - .5)^2 (Z_{max}/D)^2} \qquad 3.41$$

where Z_{max} is chosen to be the effective limit of the interaction region. The change in $\Lambda(t_n)$ as the atom traverses the n th region is governed by

$$4/3[\Lambda^3(t_n)-\Lambda^3(t_{n-1})]+(1+2KI_n)[\Lambda(t_n)-\Lambda(t_{n-1})]=\alpha_\nu KI_n T/N. \qquad 3.42$$

For an atom which enters the laser light with frequency offset Λ_0, eq. 3.41 can be used iteratively to find $\Lambda(t_n)$, the frequency offset when the atom leaves the beam.

$$\Lambda(T+t_0)-\Lambda(t_0)=\Lambda(t_N)-\Lambda_0 \qquad 3.43$$

From eq. 3.38c it follows that

$$R_1(\nu,t)=(\epsilon A/\alpha_\nu)\, d\Lambda/dt. \qquad 3.44$$

The average value of $R_1(\nu,t)$ over the interaction region is

$$\langle R_1(\nu)\rangle=(1/\langle T\rangle)\int_{t_1}^{t_1+\langle T\rangle} R_1(\nu,t)dt = (\epsilon A/\langle T\rangle\alpha_\nu)\int_{t_1}^{t_1+\langle T\rangle} d\Lambda/dt\, dt$$

$$= \epsilon A/(\alpha_\nu\langle T\rangle)\,[\Lambda(\langle T\rangle+t_1) - \Lambda(t_1)]$$

$$\langle R_1(\nu)\rangle\langle T\rangle=\epsilon A/\alpha_\nu\,[\Lambda(\langle T\rangle+t_1)-\Lambda(t_1)]. \qquad 3.45$$

If an atom has zero velocity along the laser when it enters the beam, then $\Lambda(t_1)$ is proportional to the frequency difference between the laser and the center of the atomic resonance. A plot of $\epsilon A/\alpha_\nu\,[\Lambda(\langle T\rangle+t_1)-\Lambda(t_1)]$ vs. $\Lambda(t_1)$ (ϵ is the system light detection efficiency) is the atomic line shape that results if the laser light has zero frequency

width. The expression in eq. 3.45 for $\langle R_1(\nu)\rangle\langle T\rangle$ when used in eq. 3.24 yields the photon-burst lineshapes. The total fluorescence lineshape is shown for a barium-like transition (FWHM 19.2 MHz, wavelength 5535 A (24), $KI_0=1$, Gaussian beam profile with D=13.5 mm) for atomic masses of 138 and 14 in Fig. 3.5. The curve for the lighter mass nucleus clearly shows the asymmetry arising from the radiation pressure.

Photon-burst lineshapes

In a two-level system with constant light scattering rate $R(\nu)$ and constant interaction time T, the lineshape in an individual burst spectrum is given by

$$[(R(\nu)\ T)^n\ e^{-(R(\nu)T)}]/n!. \qquad 3.46$$

The stationary points for such a curve are determined by

$$(\partial R(\nu)/\partial\nu)\ (n-R(\nu)T)=0. \qquad 3.47$$

One minimum (or maximum) occurs at ν_{max}, the frequency of the peak of the fluorescence curve which satisfies $(\partial R(\nu_{max})/\partial\nu)=0$. For $R(\nu_{max})T> n$, maxima occur at $\nu_{\pm}$, where $R(\nu_{\pm})T=n$. If $n > R(\nu_{max})\ T$ there is only one maximum which occurs at ν_{max}. This change in curve shape with multiplicity is a clue to the number of detected photons at ν_{max}. This simple result (eq.3.47) also holds for the three-level system. In general, for a two or three-level system if $n<< R(\nu_{max})T$, there will be a dip in the center of the curve; if $n\cong R(\nu_{max})T$, the curve will be flattened near the peak; and if $n>R(\nu_{max})T$ the curve will peak at ν_{max}.

For multiplicities $n<R(\nu_{max})T$ the maxima in the burst

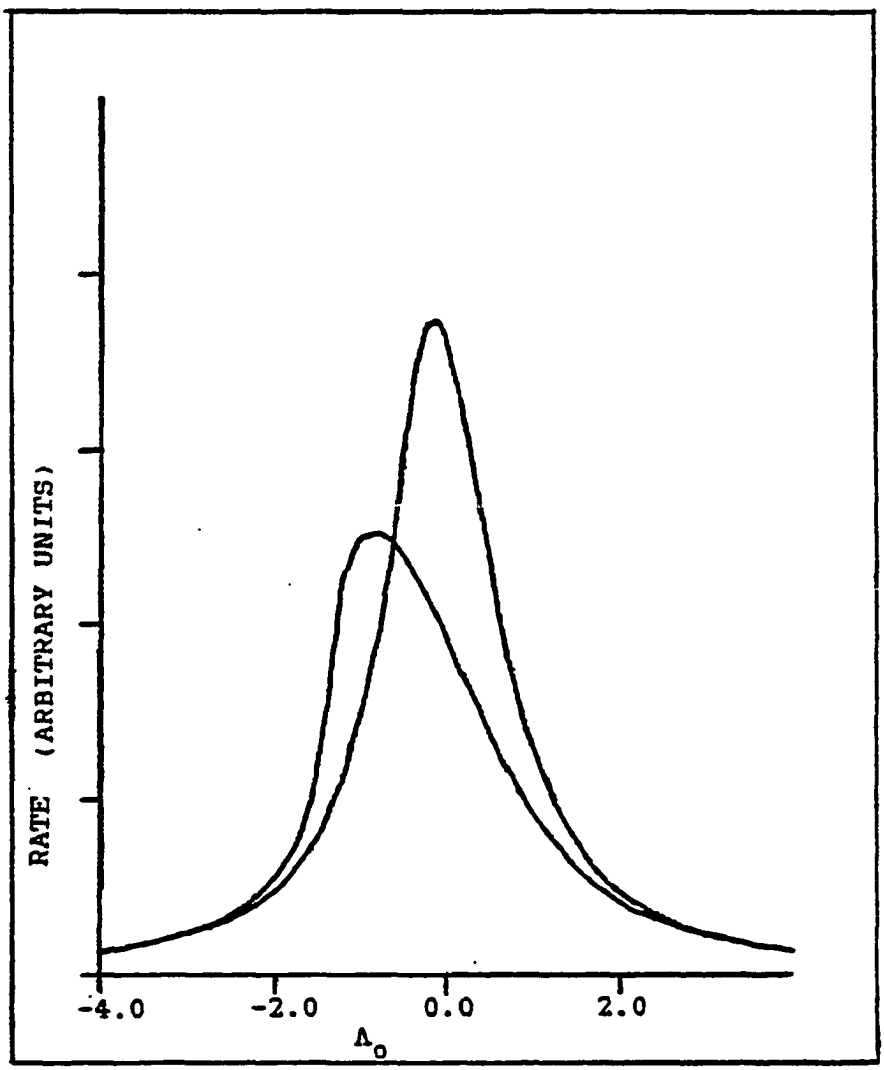

Figure 3.5 Fluorescence lineshape resulting from scattering large numbers of photons from A=14 nucleus and A=140 nucleus

spectra occur at frequencies for which $R(\nu_{\pm})T=n$ and the half maxima occur at frequencies for which the scattering rate is given by

$$2[R(\nu_{1/2},n)T]^{n} e^{-R(\nu_{1/2},n)T} = n^{n} e^{-n} \qquad 3.48$$

in a two-level system. For $n > R(\nu_{max})T$ the frequencies of half maxima are given by

$$2[R(\nu_{1/2},n)T]^{n} e^{-R(\nu_{1/2},n)T} = [R(\nu_{max})T]^{n} e^{-R(\nu_{max})T} \qquad 3.49$$

For a massive atom, the fluorescence lineshape is a Lorentzian. The FWHM for a multiplicity n in units of the fluorescence FWHM is then given by

$$W = \sqrt{[(R(\nu_{max})T)-(R(\nu_{1/2},n)T)]/(R(\nu_{1/2},n)T)} \quad . \qquad 3.50$$

The values of $R(\nu_{1/2},n)T$ can be found using eqs. 3.48 and 3.49. The widths for various multiplicities, in units of the resonant fluorescence FWHM are shown in Fig. 3.6 for $R(\nu_{max})T$ values of 5 and 10. The lower multiplicities are much wider than the natural linewidth, but the spectra narrow with increasing multiplicity. These calculations have not taken into account the effects of finite laser linewidth and power broadening on the burst spectra, but the general results are still valid: the lower multiplicities ($n<<R(\nu_{max})$ T) are wider than the natural linewidth, the spectra narrow with increasing multiplicity and, for sufficiently high multiplicities, the burst spectra have sub-natural linewidths.

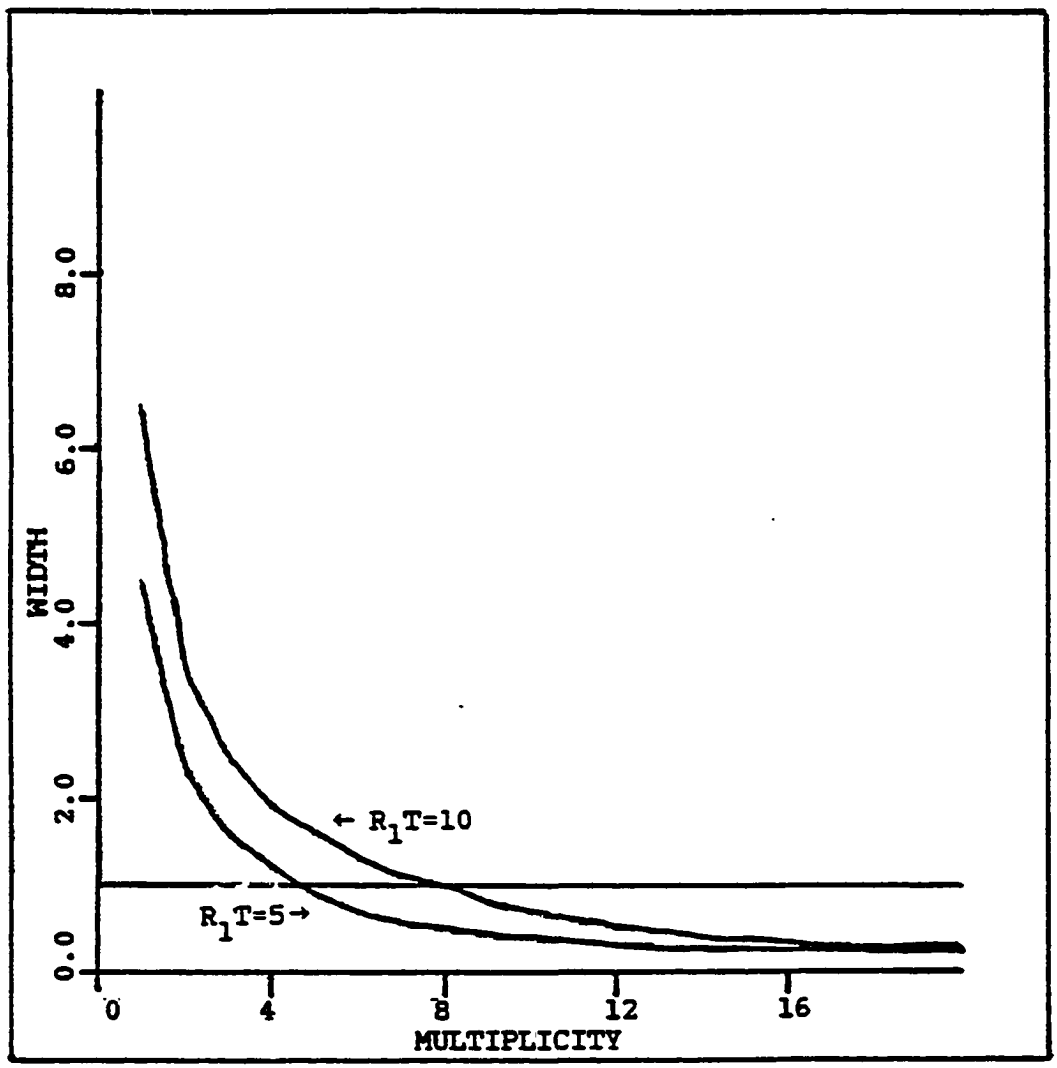

Figure 3.6 FWHM vs. multiplicity for $R_1T=5$, 10

The skewed resonant fluorescence lineshape gives rise to skewed photon-burst spectra. For $n< R(\nu_{max})T$, the frequencies at which $R(\nu_{\pm})T=n$ are not symmetric about ν_{max}. The nonlinear nature of the photon-burst function enhances the asymmetry causing the high frequency side of the curve to be suppressed at low multiplicities and enhanced at high ones. Because of this, the center of gravity of the photon-burst spectra shifts towards higher frequency with higher multiplicity. This skewness is small and barely visible in Fig. 3.7a. To compare with the experiment, the curve must be averaged over the laser frequency profile with the result shown in Fig. 3.7b. The resulting lineshape shows a clear asymmetry. The curves become more symmetric with higher multiplicity because of the line narrowing effect as discussed above.

These effects can be characterized by the first three moments of the curves. The center of gravity is characterized by the first moment, $(\int_0^{+\infty} \nu\, F(\nu)d\nu)/U$, width by the second moment, $(\int_0^{+\infty} \nu^2\, F(\nu)d\nu)/U$, and skewness by the third $(\int_0^{+\infty} \nu^3\, F(\nu)d\nu)/U$, where $U=(\int_0^{+\infty} F(\nu)d\nu)$. To summarize, there are three main effects to be noted in the spectra with increasing multiplicity.

1) The center of gravity of the curves shifts toward higher frequency with increasing multiplicity.

2) The linewidth narrows with increasing multiplicity.

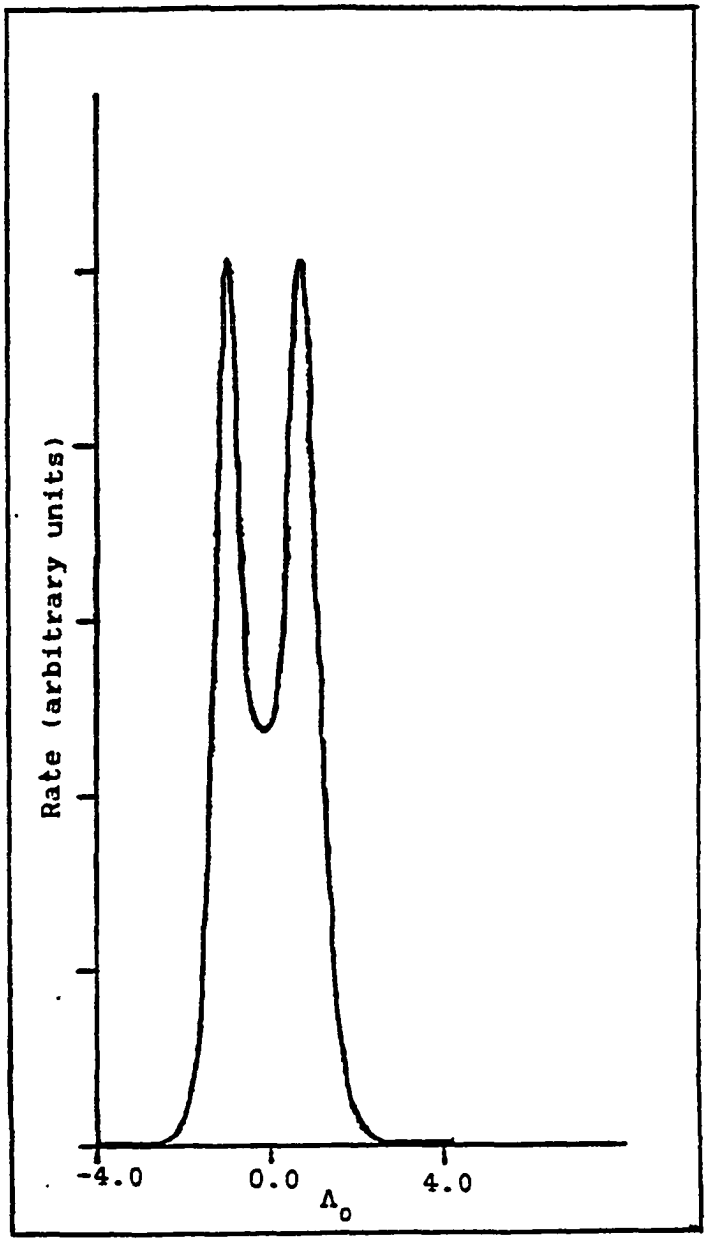

Figure 3.7a Photon burst lineshape resulting from scattering large numbers of photons

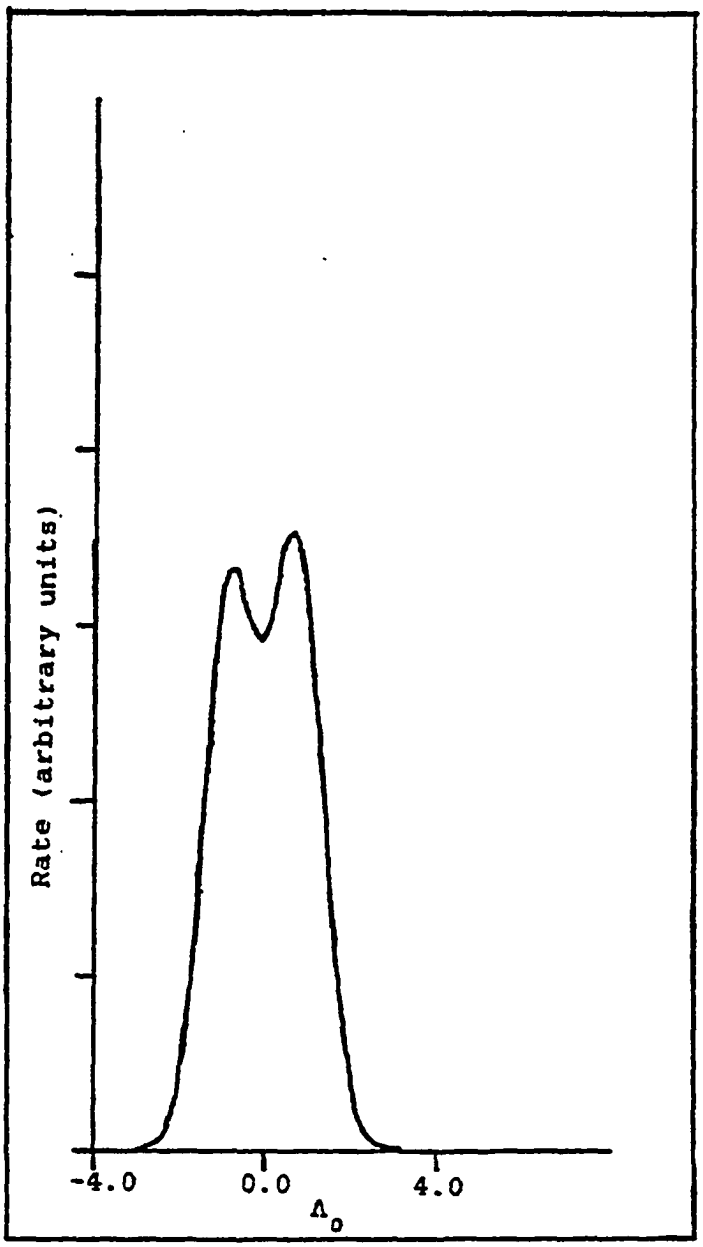

Figure 3.7b Photon burst spectal lineshape resulting from scattering of large numbers of photons averaged over laser lineshape

3) The skewness of the curves changes and becomes small for multiplicities larger than $\langle n \rangle$.

CHAPTER IV. BACKGROUND AND ATOMIC VELOCITY EFFECTS

Atoms from a thermal atomic beam such as that used in this experiment have a wide range of transit times across the laser light. This means there is no unique transit time to which the photon-burst clock can be set (see Chapter II). If the atom-scattered light statistics are to correspond to the transit-time-limited case (two-level system) or optical-pumping-limited case (three-level system) the clock cannot be allowed to time out while an atom is still scattering photons. The premature ending of the counting interval can be avoided by choosing a clock time much longer than the average atomic-transit time. This procedure works well for the short interaction regions previously used, but for the extended regions of this experiment the extremely long time settings required would lead to a very slow reduction of background with increasing multiplicity. The long, variable, atom-laser interaction time can be accommodated and slow background reduction can be avoided by using a resettable (mode 2) counter. The clock reset time is set such that the high detection rate of atom-scattered light extends the counting interval as long as the atom emits photons. When the atom stops emitting photons the clock times out ending the counting period. The resettable clock tailors the counting interval to each atomic-transit time. Atom-scattered light distributions are recorded

according to their statistics as derived in Chapter III without the slow background reduction inherent in long mode 1 settings. This chapter deals with the background statistics in the resettable mode, how a reasonable reset time is chosen, and the effect mode 2 background interference has on the atomic photon number distribution.

The problems considered in this chapter needed to be addressed to take the data and to interpret it, but an understanding of this chapter is not necessary to understand the results. The reader can skip this chapter with no loss in continuity.

Mode 2 Counting and Background

The velocity distribution of atoms from thermal source is (58)

$$P(v)dv=2(2K_bT_e/m)^2 v^3 e^{-(mv^2/K_bT_e)} dv. \qquad 4.1$$

The average time for a barium atom to cross a 1 mm beam is 2.5 μsec and 99% of all atoms have a transit time of less than 15 μsec. If the background rate is 10,000 counts/sec in a 15 μsec interval, there is an average of .15 background counts. If a one centimeter region is used, a coincidence time of 150 μsec is required for 99% of the atomic-transit times to fall within this interval. Again with a background rate of 10,000 counts/sec there would be an average of 1.5 counts/interval. The background would fall quite slowly with increasing multiplicity in this situation. A shorter clock

time can be used, which suppresses the background in burst spectra, but this leads to a larger fraction of atoms for which the counting stopped while the atom was still scattering photons, thereby distorting the photon statistics. To accommodate the wide range of atomic velocities and avoid unnecessarily long counting times, a different scheme is needed. Rather than use a clock set for a long (>100 μsec) time, a resettable clock set for a short (~10 μsec) time is used. While an atom scatters photons, the detection rate is approximately one MHz. The time between counts from atom- scattered light is, on the average, much less than the 10 μsec reset time. This high rate keeps the counter on until the atom stops scattering photons. The average time between background counts is much greater than the reset time, making a high multiplicity event from background alone unlikely. Choosing the reset time is clearly important: if it is too short the counting interval may be prematurely ended; if it is too long the background may continue to reset the clock long after the atom has left the beam. Whether a fixed-time clock (mode 1) or a resettable clock (mode 2) is used depends upon the atomic-transit time distribution and the background rate present.

As explained in Chapter II, the coincidence counter is turned on when it receives a pulse and it indicates the counting period is completed with a strobe pulse which

causes the computer to record the multiplicity of the event. Assume that only random background is present. The resettable clock strobing rate (S) with background rate R_b and reset time τ is given by (59)

$$S=R_b\, e^{-R_b\tau}.$$

After a pulse is received, the probability of no additional background pulses occurring during the reset time τ is

$$P_2(0)=e^{-R_b\tau}.$$

The probability of exactly one additional pulse being detected, i.e., exactly one retriggering is

$$P_2(1)=e^{-R_b\tau}\int_0^{\tau} R_b\, e^{-R_b t}\, dt=e^{-R_b\tau}\,(1-e^{-R_b\tau}).$$

Similarly, the probability of exactly two additional retriggerings without breaks is

$$P_2(2)=e^{-R_b\tau}\,(\int_0^{\tau} R_b\, e^{-R_b t}\, dt)(\int_0^{\tau} R_b\, e^{-R_b t}\, dt)=e^{-R_b\tau}\,(1-e^{-R_b\tau})^2.$$

In general, the probability of an n-length background photon chain, which implies n-1 clock retriggerings is

$$P_2(n)=e^{-R_b\tau}\,(1-e^{-R_b\tau})^{n-1}.$$

The rate of mode 2, n-multiplicity background events is the strobing rate multiplied by the probability of n-1 additional pulses or (60),

$$N_2(n)=R_b\, e^{-2R_b\tau}\,(1-e^{-R_b\tau})^{n-1}. \qquad 4.2$$

For a mode 1 counter each strobe pulse represents a fixed counting interval T. The fraction of time the clock is on and counting is ST. The fraction of time the clock is not counting is also the fraction of the background counts which initiate a strobe pulse, i.e., (61)

$$S/R_b=(1-ST).$$

Solving for S

$$S=R_b/(1+R_bT).$$

For a mode one counter the background count distribution is the strobe rate multiplied by the Poisson probability for n-1 additional counts (18)

$$N_1(n)=(R_b/(1+R_bT))((R_bT)^{n-1}e^{-R_bT})/(n-1)!. \qquad 4.3$$

As the background rate increases the two schemes approach different limits. The mode 1 strobe rate approaches 1/T, the inverse of the clock time, while the mode 2 rate goes to zero, recording one event consisting of all counts. Several background curves are shown for different values of $R_bT(\tau)$ (Fig.4.1a-b). These curves were obtained with scattered He-Ne laser light with the background count rate adjusted by the changing amount of light sent into the chamber. The solid lines are values from calculations using the measured background rate and clock time setting in equations 4.2 and 4.3 and the points are the actual number

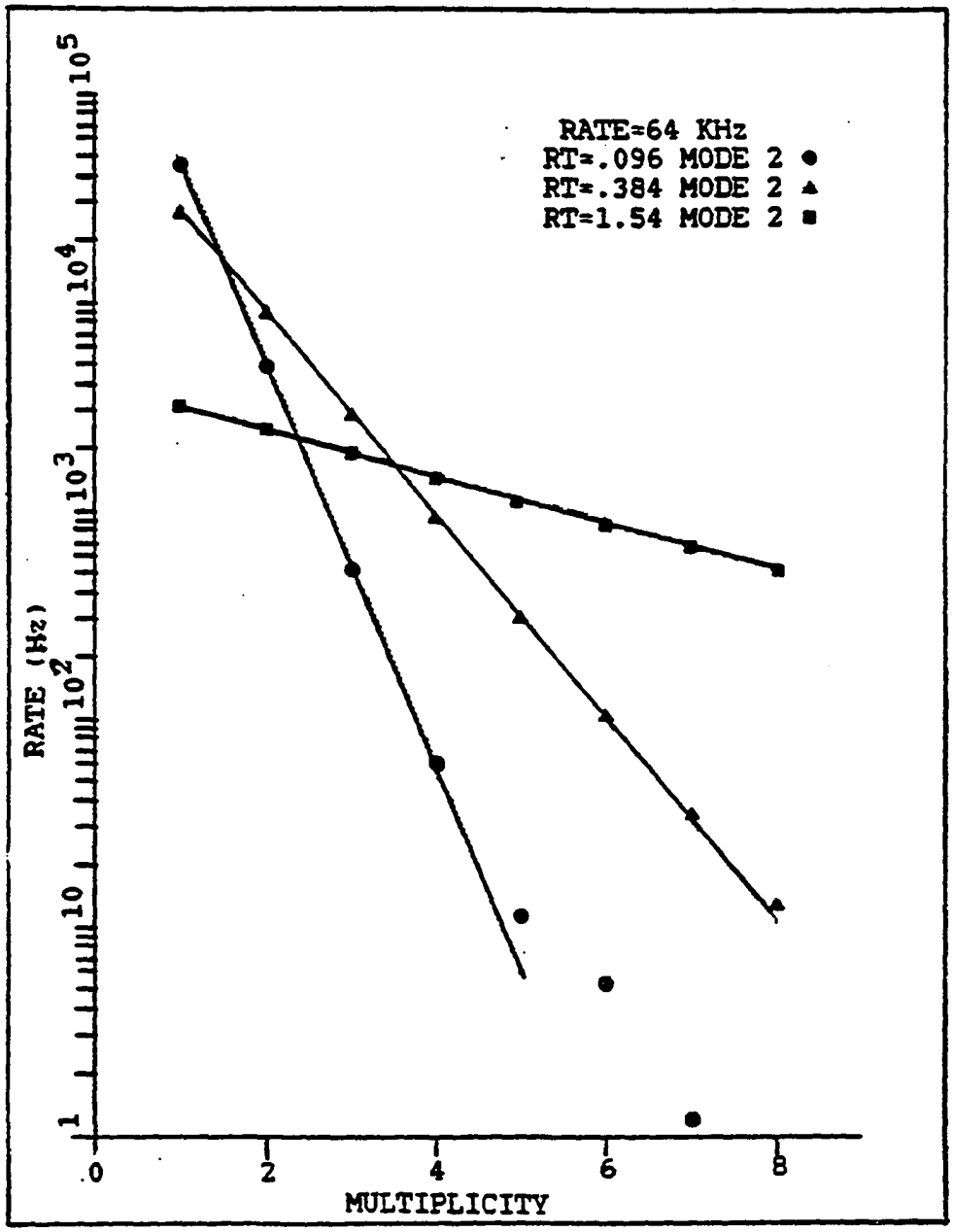

Figure 4.1a Mode 2 background distributions: theory(line) and experiment(points)

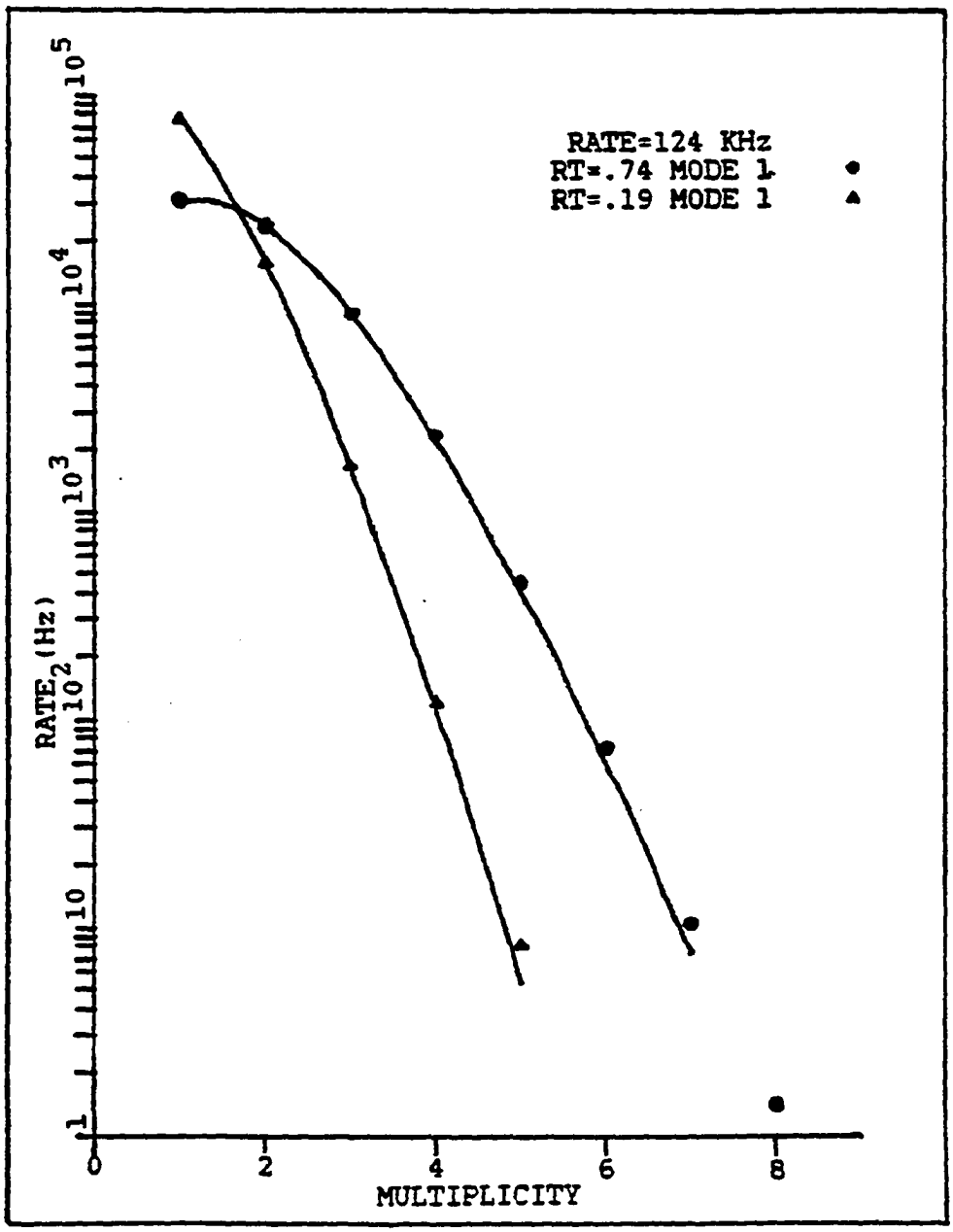

Figure 4.1b Mode 1 background distributions: theory(line) and experiment(points)

of counts measured at the various multiplicities for the mode, background rate and time setting indicated for each graph.

For equal background rate and clock time settings, the mode 1 burst background rate decreases with multiplicity much faster than the mode 2. If the required mode 2 clock setting is τ, and the mode 1 time required is $M\tau$, the ratio of the mode 1 background rate to the mode 2 background rate at multiplicity n is

$$\frac{N_1(n)}{N_2(n)} = \frac{1}{(1+R_b M\tau)} \cdot \frac{(R_b M\tau)^{n-1}}{(1-e^{-(R_b\tau)})^{(n-1)}} \cdot \frac{e^{(2-M)R\tau}}{(n-1)!}$$

For an $R_b\tau$ of .15 the calculated results are shown for various values of M (Fig. 4.2). If the longest atomic-transit time to be accommodated is only two or three times that of the reset time required, the mode 1 scheme is preferable. For longer atomic-transit times the balance swings toward using a resettable clock.

Dark Counts

Due to phototube dark current the background distribution noticeably deviates from pure scattered light statistics at higher multiplicities. The dark counts tend to come in bunches, resulting in more high multiplicity events than would be expected for randomly scattered light. Bursts of dark counts are fairly independent of the mode two reset time. In Fig. 4.3, dark count rates for multiplicities 1-9

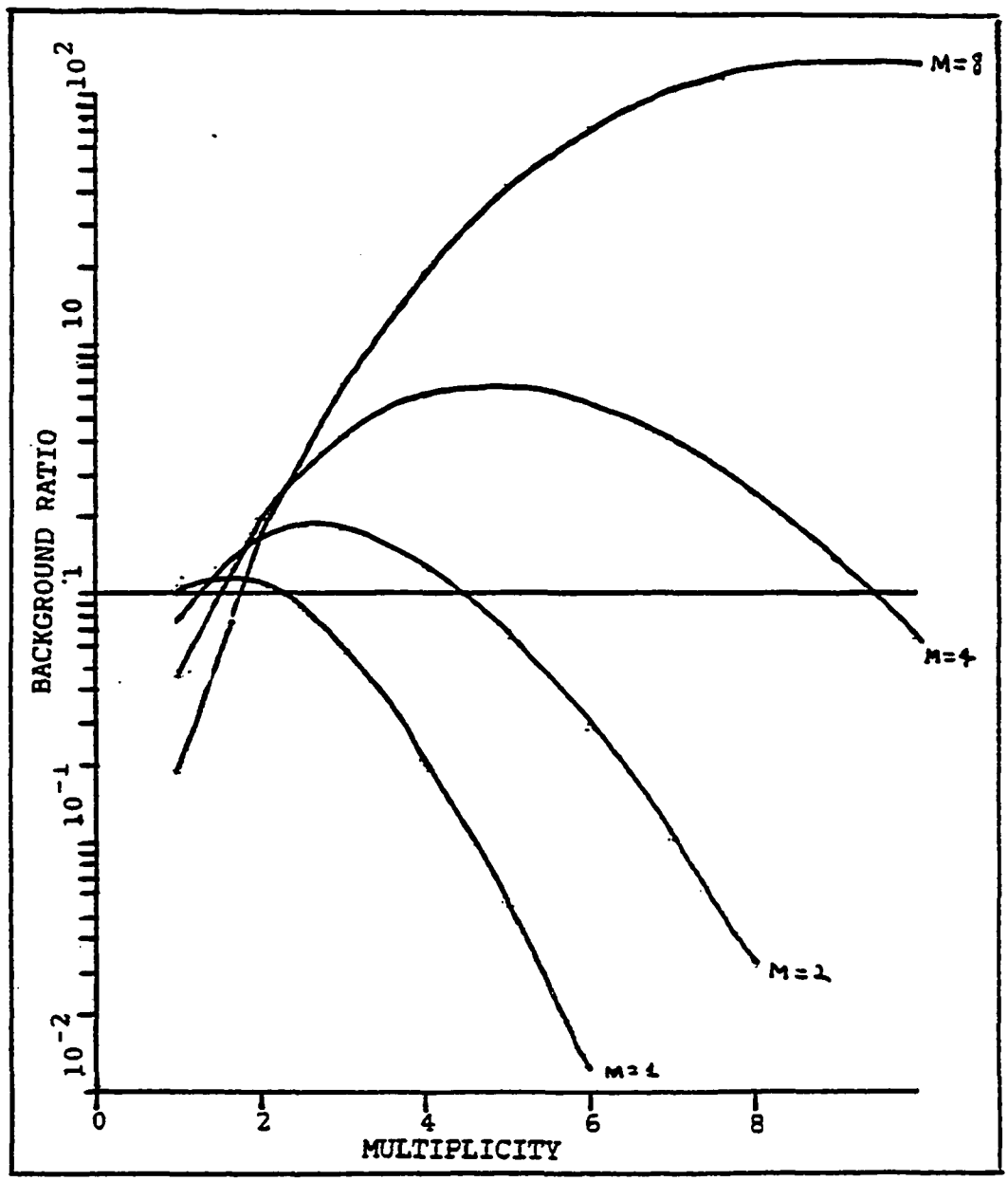

Figure 4.2 Ratio of Mode 1 background rate to Mode 2 for various multiplicities and "M" values. The solid horizontal line represents the ratio of one, points above the line favor mode 2, and points below favor mode 1.

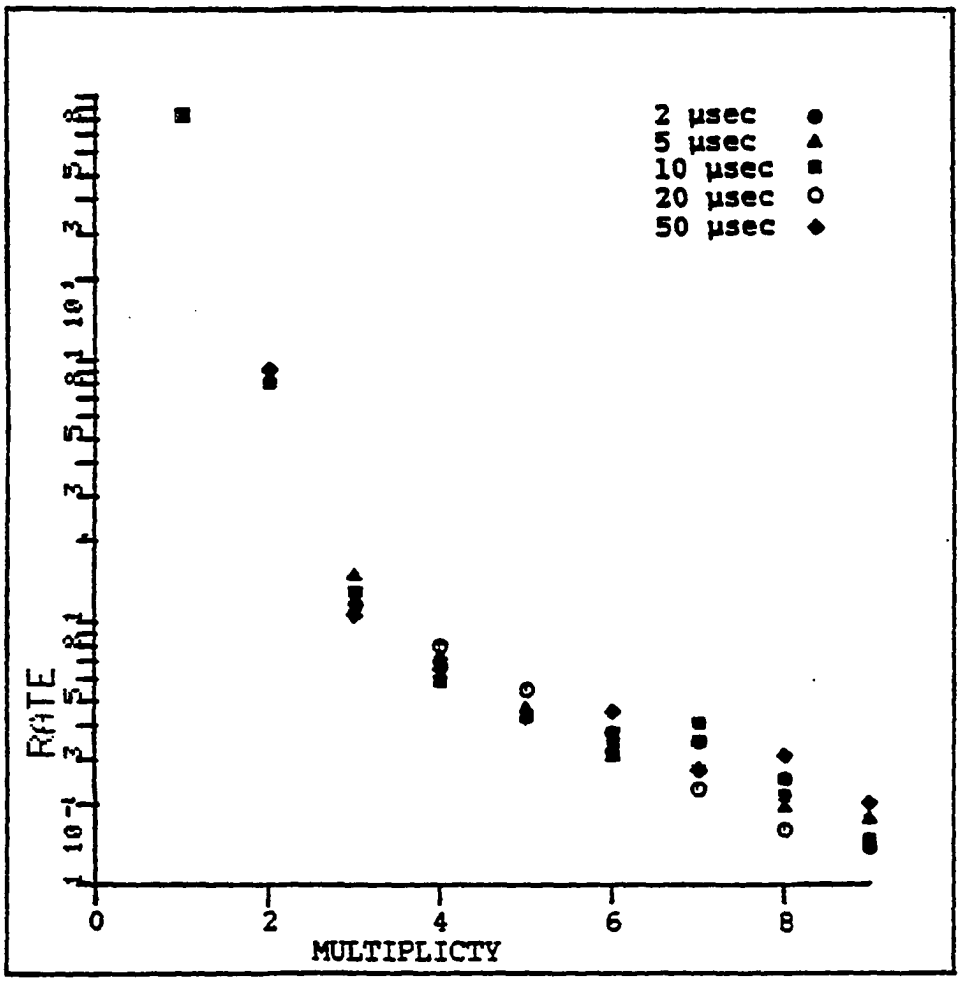

Figure 4.3 Dark count distributions for four mode 2 reset times

are shown for reset times between 2 and 50 μsec. Even at multiplicity nine, there is no statisticaly significant difference between the 2 μsec and 50 μsec settings. For scattered light the ratio of the backgrounds for such time differences would be on the order of $(25)^9$. Since the dark count rate is much smaller than the light scattered background count rate (~200 dark counts/sec vs.~10,000 counts/sec from scattered light) and the dark counts are independent of reset time, there effect is easily removed in the background subtraction algorithm developed in the background interference section.

Dark counts from two phototubes are assumed to be independent. If counts are required from both tubes to initiate a strobe pulse then the anomalously high event rates in large multiplicities do to autocorrelation in the dark counts of a single tube are greatly reduced. In Fig. 4.4a the result of requiring one photon from each tube is shown. The dark counts are reduced a factor of 100 by requiring one count from each tube and a further improvement of 100 can be obtained with a two counts/tube coincidence. Scattered laser light provides pulses to fulfill the coincidence requirements thereby reducing the effectiveness of this scheme. In Figs. 4.4b and c, graphs of data taken with both laser scattered light and phototube dark counts present are shown. Background is reduced when a coincidence

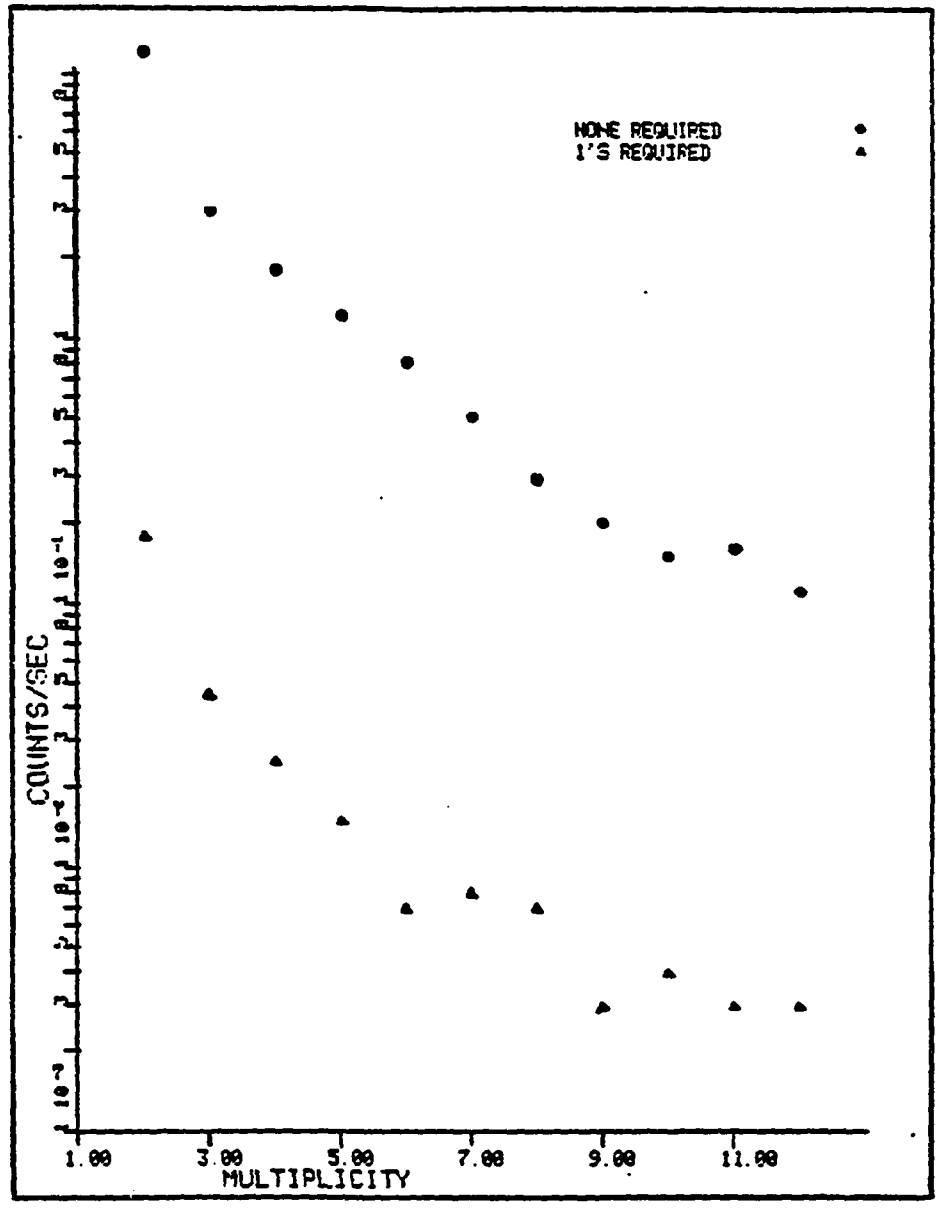

Figure 4.4a Dark counts with no coincidence requirement, and a one count/tube requirement.

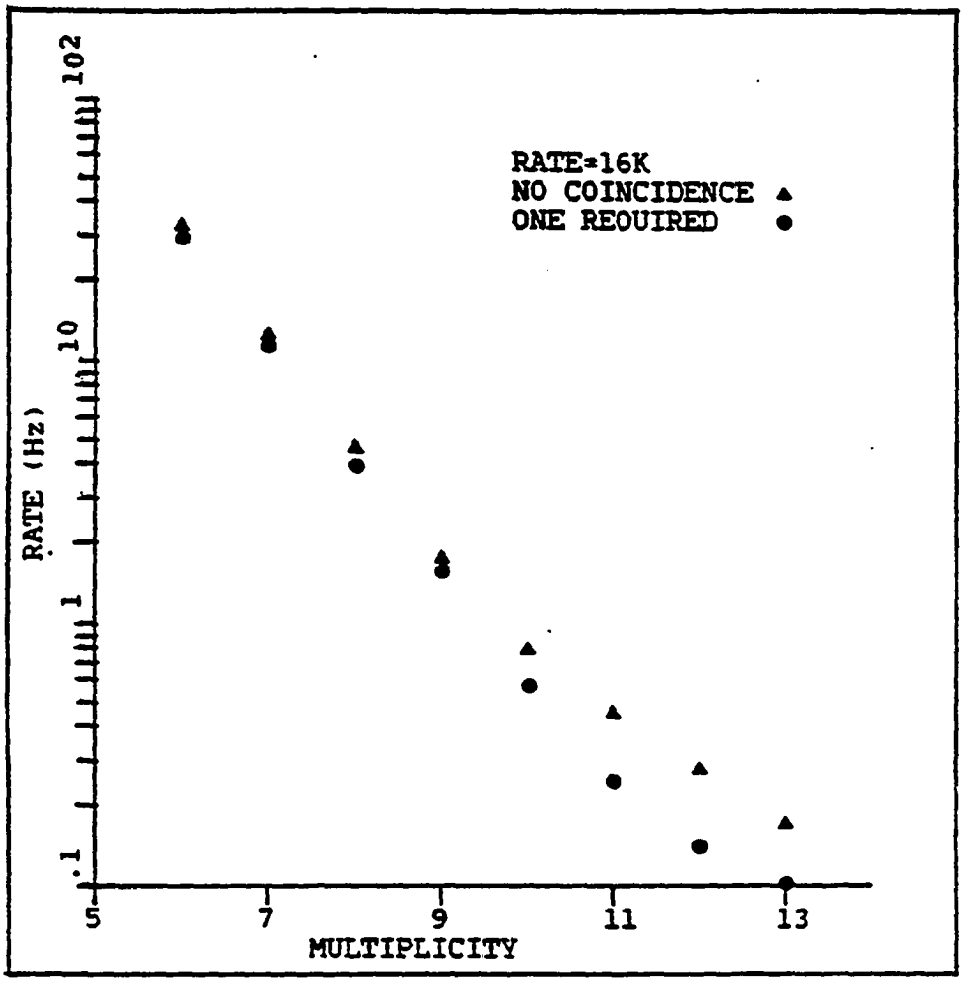

Figure 4.4b Background with and without a coincidence requirement

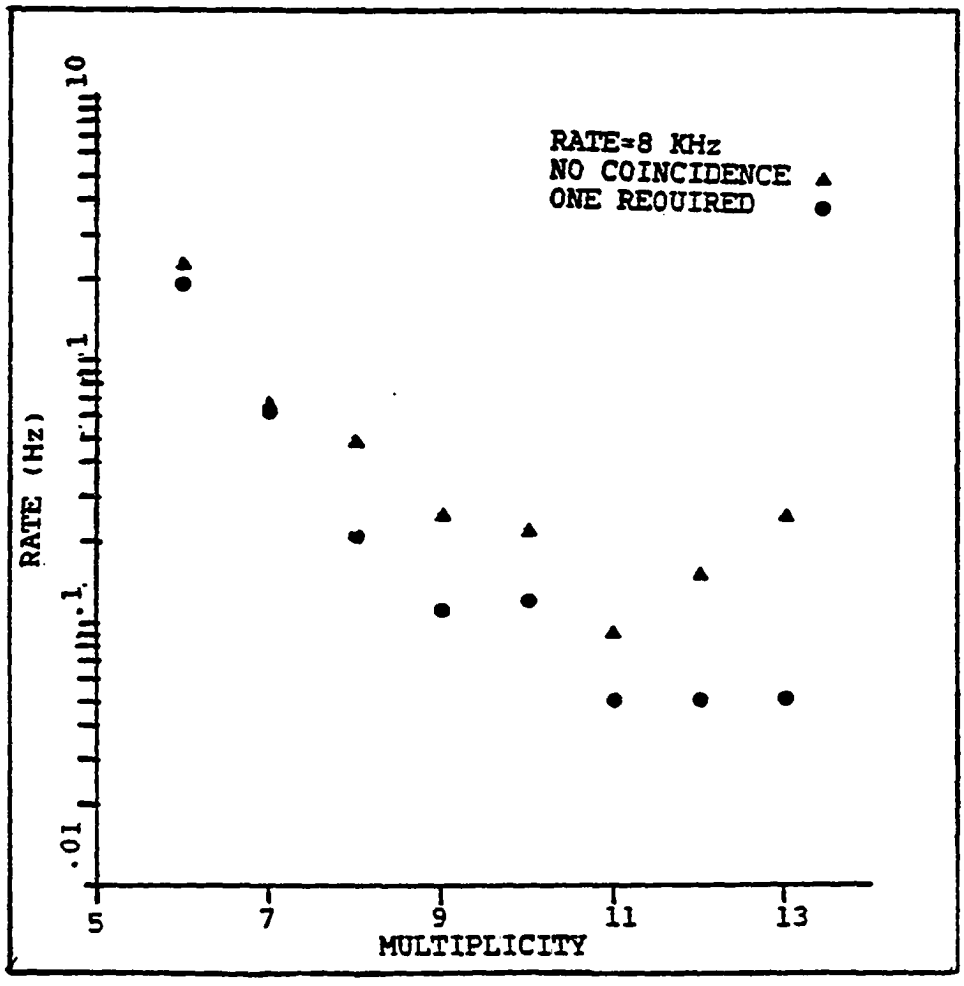

Figure 4.4c Background,with and without a coincidence requirement

is required, but the reduction is not as dramatic as for the case with no laser scattered background light. Comparing Figs. 4.4b and 4.4c, the background reduction can be seen to be greater when the scattered laser light intensity is reduced.

Requiring counts from each tube affects the multiplicity distribution by selectively discarding events. If one count is required from each tube, all events in which zero counts come from one tube and n counts come from the other are rejected. In general, for n incoming counts there are 2^n possible ways for these counts to be distributed between two tubes. If one count is required from each tube, then two of these possibilities are rejected. The fraction accepted is

$$F_{a1}(n)=(2^n-2)/2^n.$$

It is assumed that the tubes have equal light detection efficiencies. Similarly, when two counts are required from each tube the fraction accepted is

$$F_{a2}(n)=(2^n-(2+2n))/2^n.$$

When C counts are required from each tube, the fraction of counts accepted will be

$$F_{ac}(n)=(2^n-2\ \Sigma_{k=0}^{C}\ \binom{n}{k})/2^n.$$

Table 4.1 shows the fraction accepted for various values of C and N. These factors must be included in the comparison of experimental distributions to those derived in Chapter III.

Table 4.1 Two Tube Correction Factors

n	C=1	C=2	C=3	C=4	C=5	C=6
1	.000	.000	.000	.000	.000	.000
2	.500	.000	.000	.000	.000	.000
3	.750	.000	.000	.000	.000	.000
4	.875	.375	.000	.000	.000	.000
5	.938	.625	.000	.000	.000	.000
6	.969	.781	.313	.000	.000	.000
7	.984	.875	.547	.000	.000	.000
8	.992	.930	.711	.273	.000	.000
9	.996	.961	.820	.492	.000	.000
10	.998	.979	.891	.656	.241	.000
11	.999	.988	.935	.773	.451	.000
12	1.00	.994	.961	.854	.612	.226
13	1.00	.997	.978	.908	.733	.419
14	1.00	.998	.987	.943	.820	.576
15	1.00	.999	.993	.965	.882	.698

Chain Breaking

The mode 2 reset time depends on the detection rate of photons from an atom. It must be long enough so the clock cannot fail to reset while the atom is still scattering photons. The premature ending of the counting period wouldcause the chain of photons making up an event to be split and interpreted as two events. This is called a chain break.

For a chain break to occur three things must happen:
1) a photon from an atom must be detected, starting or resetting the clock;
2) no photons are detected for the reset time τ; and
3) the atom emits another detected photon before leaving the beam.

The probability of this happening is

$$P_{cb}(\tau)\, dt = P(t) P_n(t, t+\tau) P(t+\tau, T_f)\, dt$$

where $P(t)dt$ is the probability of a detected photon between time t and t+dt, $P_n(t,t+\tau)$ is the probability of no detected photons between time t and $t+\tau$ and $P(t+\tau,T_f)$ is the probability of a detected photon between time $t+\tau$ and T_f. The time that the atom leaves the beam is T_f. If the rate of detected photons from an atom (R_1) is constant between t=0 and T_f then

$$P_n(t,t+\tau) = e^{-(R_1 \tau)}$$

$$P(t+\tau, T_f) = [1 - e^{-(R_1 [T_f - (t+\tau)])}]$$

$$P(t)dt = R_1 dt.$$

The probability for a chain break to be initiated between time t and t+dt is

$$P_{cb}(\tau)dt=R_1[e^{-(R_1\tau)} - e^{-(R_1(T_f-t))}]dt.$$

The probability of this happening anywhere within an atomic transit is given by

$$P_{cb}(\tau)= \int_0^{v_m} P(v)dv \int_0^{(D_I/v\ -\tau)} R_1[e^{-(R_1\tau)} - e^{-R_1(D_I/v-t)}]dt$$

where D_I is the length of the interaction region, and v_m is equal to D_I/τ. If $v>D_I/\tau$ the atom spends less than a counting interval in the laser beam, so no chain break can occur.

If R_1 is not constant then $P_n(t,t+\tau)$ is more complicated. Consider a varying rate $R_1(t)$ which is equal to R_1' from time zero to t_1, and R_1'' from time t_1 to T_f. The probability for zero detected photons from time zero to t_1 is

$$P_n(0,t_1)=e^{-R_1't_1},$$

and from t_1 to T_f it is

$$P_n(t_1,T_f)=e^{-R_1''(T_f-t_1)}.$$

The probability for no counts over the entire range is

$$P_n(0,T_f)=e^{-[R_1't_1+R_1''(T_f-t_1)]}.$$

If $R_1(t)$ is many blocks, each with rate R_n for time Δt_n, the

probability of a zero over this interval is

$$P_n(0,T_f)=e^{-[\Sigma_{n=0}^{N} R_n\ \Delta t_n]} .$$

As $\Delta t_n \to 0$ and $R_n \to R_1(t)$, this expression becomes

$$P_n(t_1,t_2)=e^{-R_I(t_1,t_2)} .$$

$$R_I(t_1,t_2)=\int_{t_1}^{t_2} R_1(t)dt$$

The probability for a chain break with a time dependent count rate averaged over velocity is given by the following expression.

$$P_{cb}(\tau)=\int_0^{v_m} P(v)dv \int_0^{D_I/v-\tau} R_1(t)\left[e^{-R_I(t,t+\tau)} - e^{-R_I(t,D_I/v)}\right]dt \qquad 4.4$$

The population of the upper level as a function of position along the laser beam is needed to find $R_1(t)$. The form of $R_1(t)$ was given in Chapter III. The values that are used in eq. 4.4 in the remainder of this chapter are consistent with saturation data as described in Chapter V. Note that these chain breaking expressions apply only for the two-level case.

To experimentally determine the correct reset time, spectra were taken holding input power and beam profile constant while the reset time was varied. If chain breaking is present the number of events with higher multiplicities is diminished since some of these events are broken into shorter chains, and the lower multiplicities are enhanced as

the broken chains appear as several low multiplicity events. Since increasing the reset time (τ) eliminates chain breaks, the photon number distributions should, except for statistical fluctuations, become indistinguishable as τ increases. The four photon number distributions plotted in Fig. 4.5 were measured with reset times of 9.09, 18.2, 25.0 and 35 μsec, a Gaussian beam with FWHM of 5.27 mm, 5 mW of total input power (distribution C2, see Chapter II) and a background count rate of 14,000/sec. The backgrounds in the burst spectra were measured by monitoring frequencies far from resonance. These values for each multiplicity were subtracted from the data to obtain the peak heights plotted. The curves do not converge with increasing reset time. This indicates either there is significant chain breaking even for τ=25 μsec or some other effect is causing this divergence.

Background Interference

The chain breaking effect was investigated using a Monte Carlo program which simulated a three-level atom with an adjustable branching ratio (a two-level atom could be modeled by using a branching ratio of infinity) emitting photons at a constant rate over a one centimeter region. The atomic velocity distribution for a thermal source (eq. 4.1) was used, and random background counts could be included. The program kept track of how the counts in each

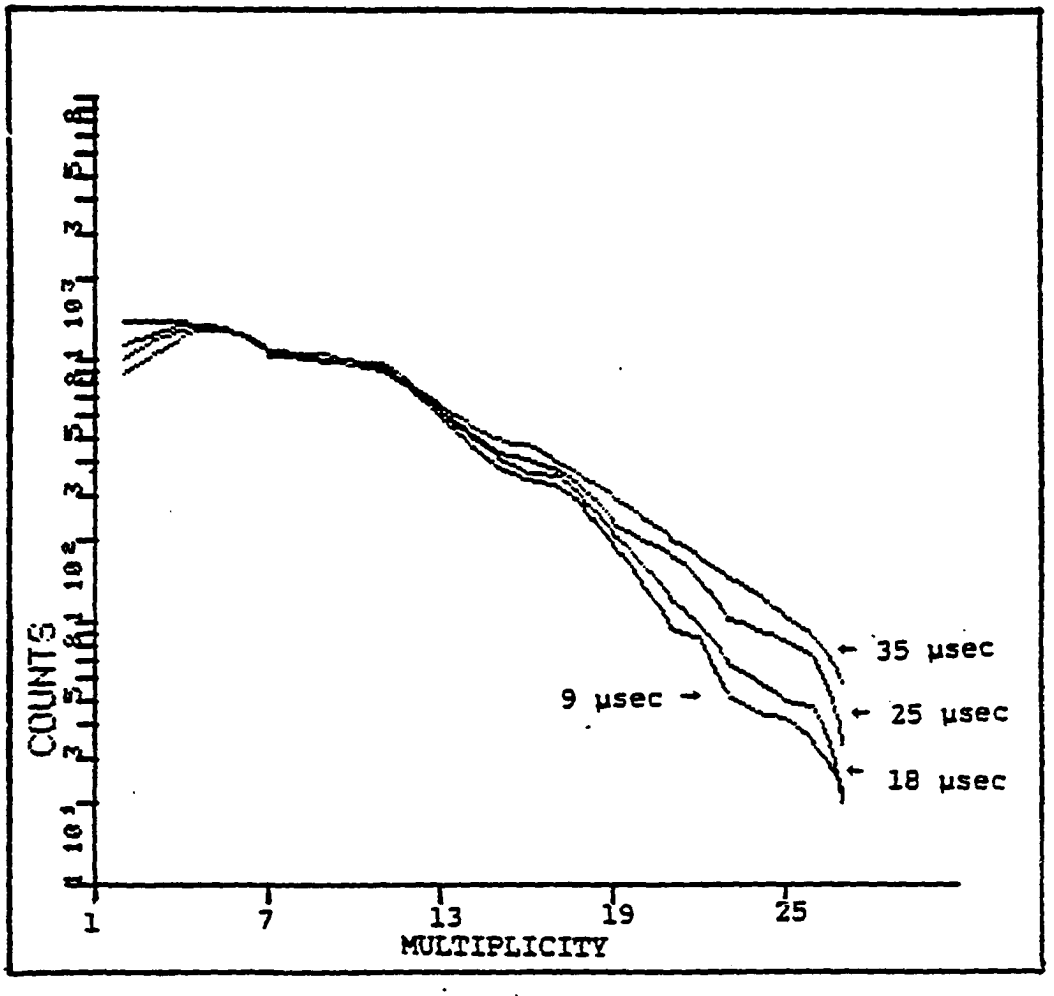

Figure 4.5 Photon burst data taken with four mode 2 reset times

multiplicity were produced, so that the effects of chain breaking and background could be studied. For a two-level atom with no random background the results agreed with the predictions of equation 4.4.

To study these effects under conditions similar to the C2 measurement (Fig. 4.5), the program was run using a three-level atom, with γ=11 (see Chapter III and Chapter V) and with a background count rate of 14,000/sec and an atomic photon scattering rate which approximately gives the same number of detected photons as in the measurements. The results of the calculation are shown in Fig. 4.6. The solid line is the average of the three distributions from just the atomic photon scattering and the points include chain breaks and background counts with reset times of 9, 18 and 35 μsec. The program recorded no breaks for the 18, or 35 μsec runs in 20,000 events, but the distributions still have not converged. If the background is set to zero, as in Fig. 4.7, the distributions show no significant differences. It should be noted that even the 9.09 μsec run, which has a 5% chain breaking rate, fits in nicely with the rest. This clearly indicates that the divergence in the experimental distributions is do to background interference rather than chain breaks. Background interference arises when n counts are produced by an atom during its transit and an additional v background counts occur during the same period causing the

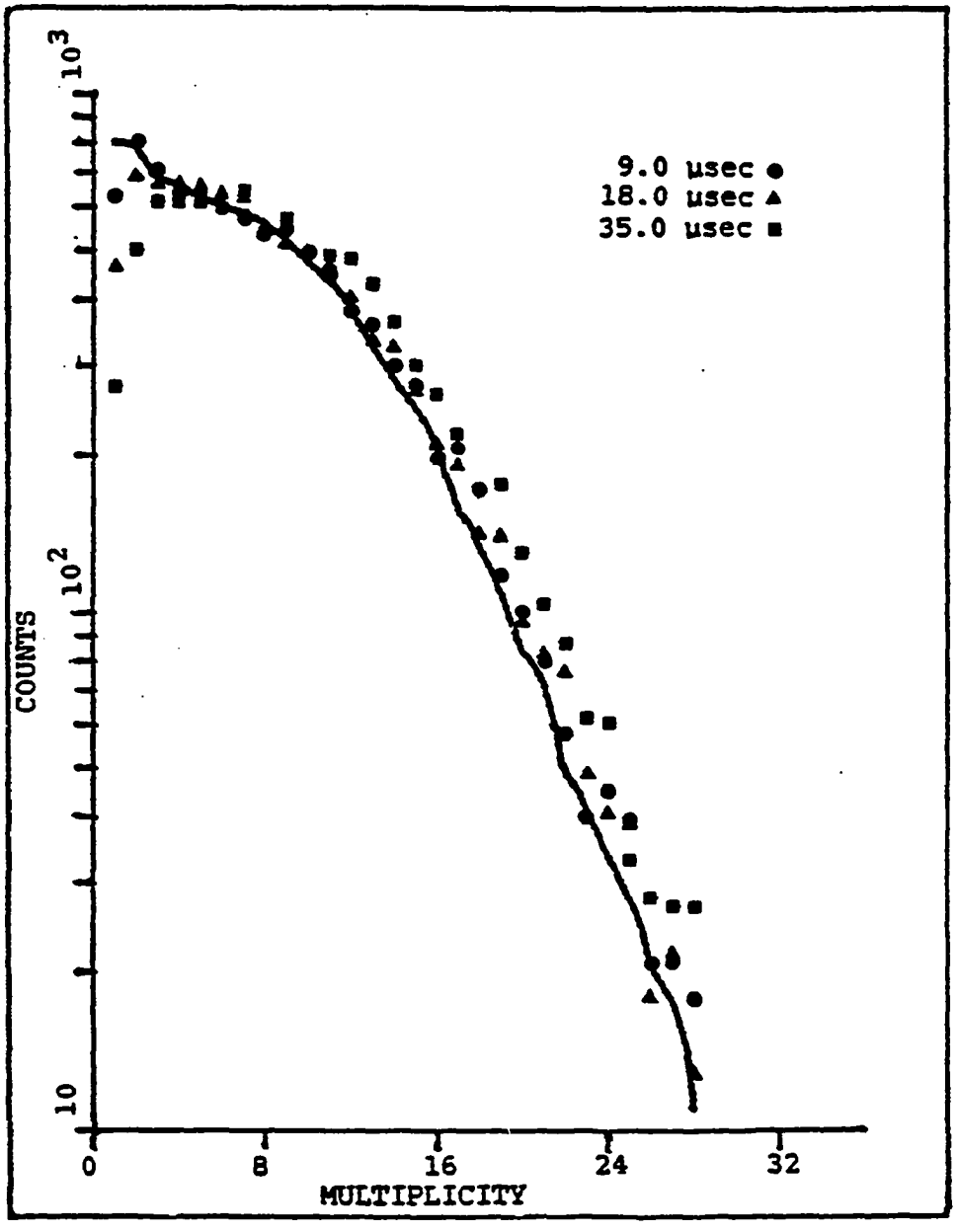

Figure 4.6 Monte Carlo program result. Points are burst data with background and chain breaking, the solid line is the average burst distribution with atom scattered photons only

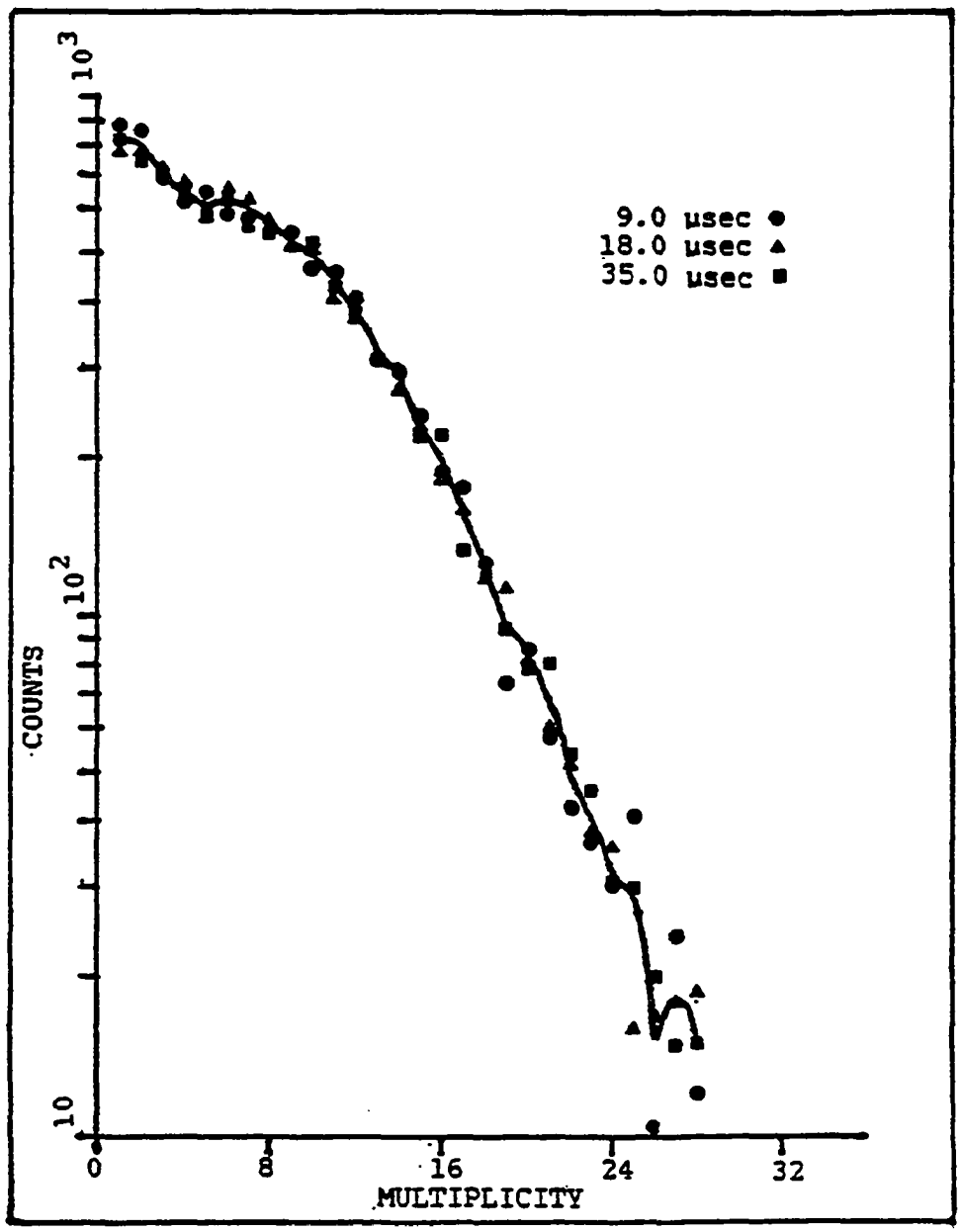

Figure 4.7 Monte Carlo program result. Burst data taken with four reset times, zero background

event to be recorded as a multiplicity n+y event rather than multiplicity n event. This effect is not removed by the simple background subtraction to find the peak heights.

As discussed in Chapter III, $R_1(t)$ is not a constant. Calculations and a Monte Carlo program utilizing the form for $R_1(t)$ developed there show that, for $\tau>18$ μsec, the number of chain breaks is less than .03% of the total number of events for conditions under which the C2 data were measured. Graphs of the number of chain breaks expected per 10,000 atoms for several situations are presented in Fig. 4.8. The Monte Carlo program and eq. 4.4 show that, as a general guideline, if $(\langle R_1\rangle\tau)>6$, less than 1% of the events suffer a chain break.

The predicted chain breaking rate is far too low to account for the observed experimental differences in the distributions, and the Monte Carlo program has shown that background interference alone could be responsible for the observed divergences. To compare distributions obtained with different reset times, background interference must be factored out.

If an atom scatters n photons with probability $P_a(n)$, the number of multiplicity n events is $N_0P_a(n)=N_a(n)$, where N_0 is the total number of atoms. If during the atomic transit the probability of an additional y background counts is $P_b(y)$, then $N_a(n)P_b(y)$ of the true multiplicity n atomic

Figure 4.8 Calculations of chain breaks/10,000 events in various situations. The upper curve represents the calculations with a variable scattering rate and the points are the Monte Carlo results. The lower curve represents the calculations with a constant rate and the points are the Monte Carlo results

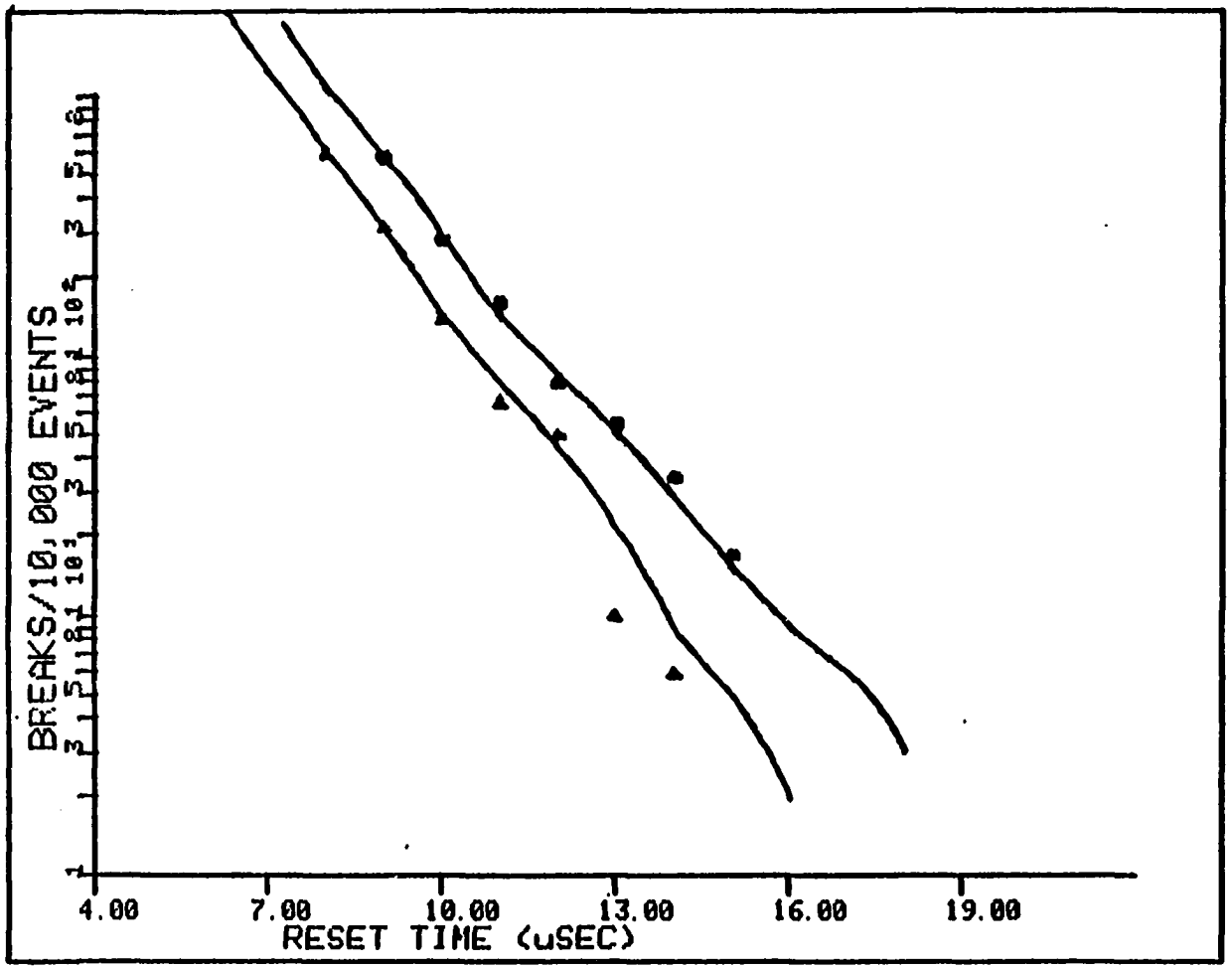
BREAKS/10,000 EVENTS
4.00
7.00
10.00
13.00
16.00
19.00
RESET TIME (uSEC)

photon events will be recorded as n+y atom+background photon events. The number of events recorded at a given multiplicity is

$$N(n)=\sum_{k=0}^{n-1} N_a(n-k)P_b(k).$$

The quantity N(n) is measured and $N_a(n)$ is the quantity desired. The sum goes to n-1 rather than n because it is assumed that pure background events ($N_a(0)$) have already been removed by simple subtraction. In Fig. 4.6 the points are N(n), the solid line represents $N_a(n)$. Solving the above equation for $N_a(n)$ yields

$$N_a(n)=[N(n)-\sum_{k=1}^{n-1} N_a(n-k)P_b(k)]/P_b(0).$$

To disentangle $N_a(n)$ from N(n) the form of $P_b(y)$ must be found. This is done in the Appendix. The probability of y background counts occurring during an atomic photon event depends upon the multiplicity of the event, so the background count distribution should actually be written as $P_b(n,y)$. The relationship between the number of counts recorded [N(n)] and the number scattered by the atom [$N_a(n)$] is

$$N(n)=\sum_{y=0}^{n-1} N_a(n-y)P_b(n-y,y)$$

$$N_a(n)=1/P_b(n,0)[(N(n)-\sum_{y=1}^{n-1} N_a(n-y)P_b(n-y,y))]. \qquad 4.5$$

$N_a(1)=N(1)/P_b(1,0)$

$N_a(2)=[N(2)-N_a(1)P_b(1,1)]/P_b(2,0)$

$N_a(3)=[N(3)-N_a(2)P_b(2,1)-N_a(1)P_b(1,2)]/P_b(3,0)$

$N_a(4)=[N(4)-N_a(3)P_b(3,1)-N_a(2)P_b(2,2)-N_a(1)P_b(1,3)]/P_b(4,0)$

In the calculation of background interference the autocorrelation in dark counts has been ignored. The dark count rate from both tubes is much lower than the random background count rate (~200 counts per second as opposed to ~14,000 counts per second) even though the former dominate high multiplicity events. The probability of a dark-count burst while an atom is in the beam is extremely small. Because of this, dark counts do not enter into the above interference terms, but add to the overall level of the background in a particular multiplicity. As shown in Fig. 4.3 the dark count background is independent of the mode 2 time. The dark count background is dealt with by simply subtracting it from the height of the resonance peak. Because of the high rate of the random background, the probability of a count while an atom is in the beam cannot be ignored, and the background interference terms must be calculated.

To find $N_a(n)$, in principle N(n-1), N(n-2)... N(1) must be known. The two tube coincidence scheme used in this experiment required one count from each tube, so no values of N(1) were recorded making it impossible to directly solve for $N_a(1)$. Monte Carlo results indicate that, for scattering

and background rates encountered in this work, $N(1)<N(2)$ and $N_a(1)>N_a(2)$. In general, $N(n)<N_a(n)$, since $N(n)=N_a(n)/P_b(1,0)$. In Fig. 4.9, graphs of $N_a(n)$ extracted using eq. 4.5 are shown for three different choices of N(1). The values of N(n) were generated with the Monte Carlo program with a background rate of 14,000 count/sec and a reset time of 18 μsec. The three values of N(1) used were 300, 550, and 800. The actual value for N(1) from the Monte Carlo program was 550. The three different values of N(1) give very different values of $N_a(1)$ and $N_a(2)$, but by multiplicity three, the three curves have converged. The choice of N(1) strongly affects $N_a(1)$ and $N_a(2)$ but, due to the rapid decline of background with increasing y, has little affect upon higher multiplicities. Since the higher multiplicities are not affected by the choice of N(1), theoretical fits to these multiplicities are independent of this initial choice. The theoretical fit yields a value for $N_a(1)$, which can be used to find a new value for N(1). This new value for N(1) can then be used to generate a new curve, from which a new value of $N_a(1)$ can be obtained. Because the higher multiplicities are independent of the choice of N(1), this process converges quickly, usually in two steps.

This algorithm was used on the four experimental C2 distributions previously plotted in Fig. 4.5 and the results are shown in Fig. 4.10. The 9.0 μsec data is the solid

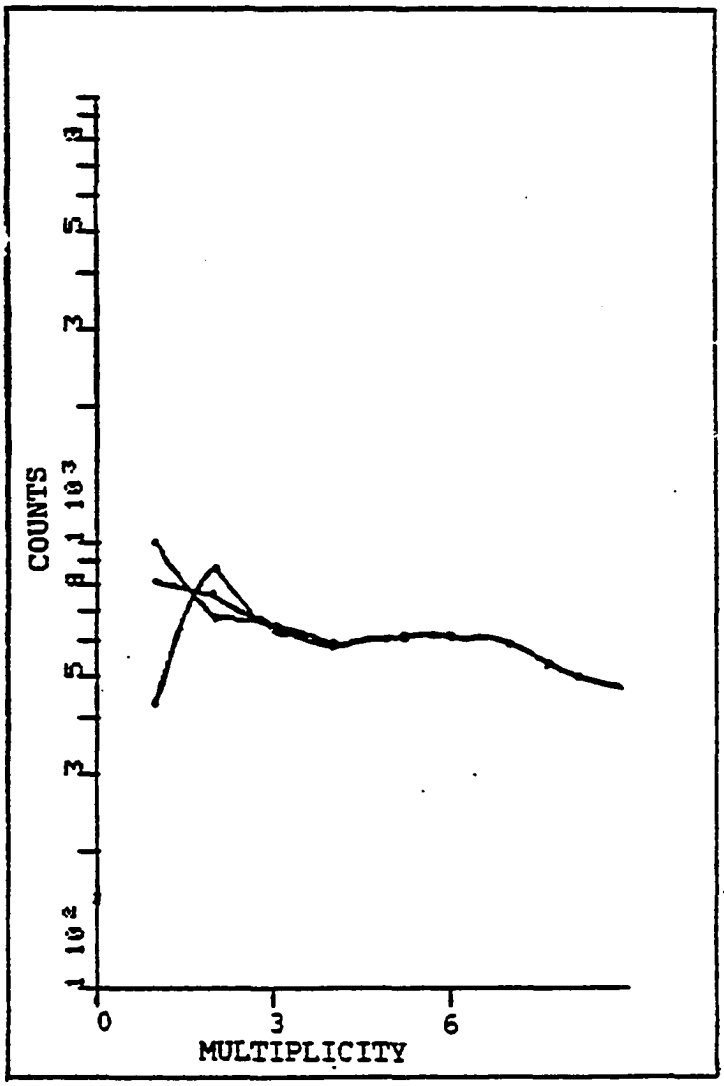

Figure 4.9 The result of using different values for $N_a(1)$. Note that for $N_a(3)$ the three predictions coincide

curve. The 25 and 35 μsec data fall on top of each other and the 18 μsec data differences from these are statistically significant only near multiplicity 14. This confirms that background interference is the cause of the difference in the distributions, not chain breaking. The level of chain breaking can be predicted with sufficient accuracy to be avoided, and a method of removing background interference has been found. This allows distributions taken with different background count rates and different mode 2 reset times to be compared to each other in a meaningful way.

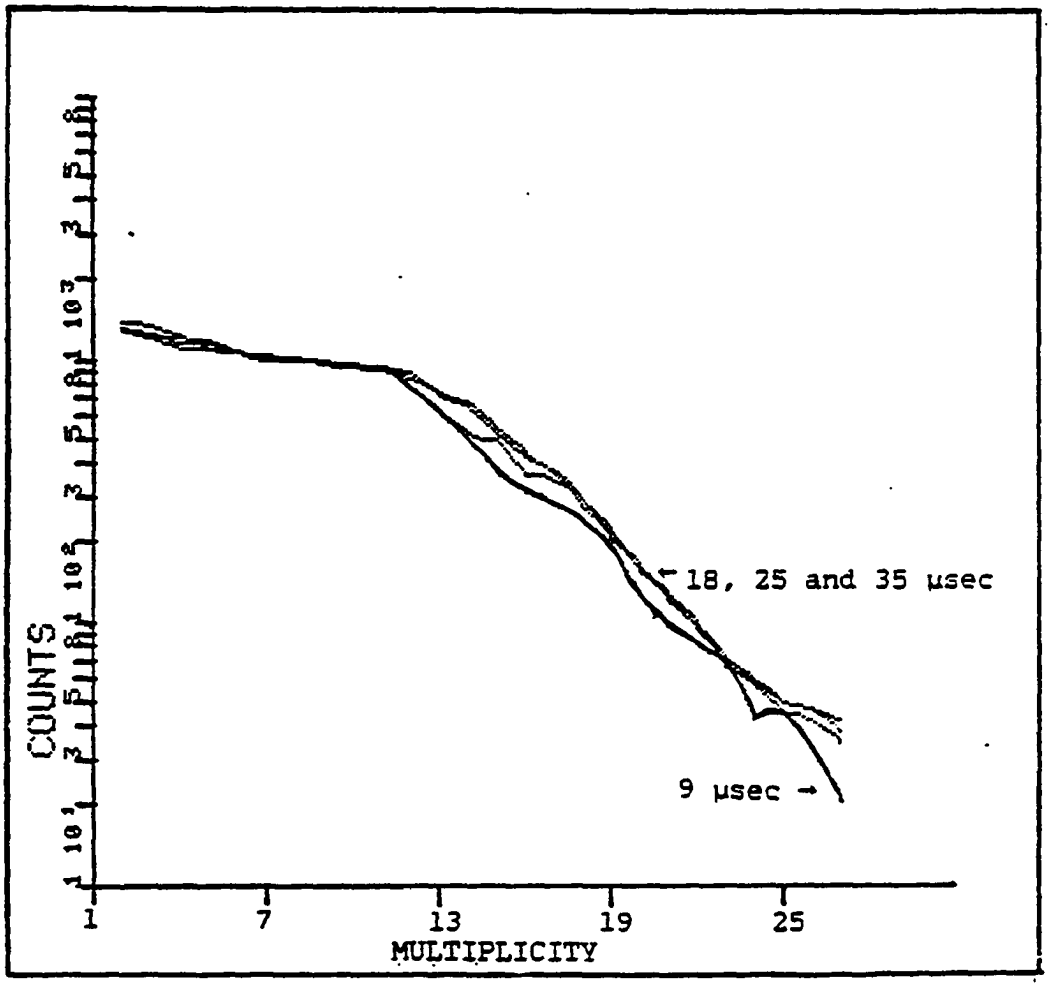

Figure 4.10 Photon burst data after the background removal algorithm

CHAPTER V. DATA AND ANALYSIS

The laser beam intensity profiles were measured. The spontaneous emission rate was also measured as a function of laser power for a small interaction region. These rates agreed well with the two-level prediction in eq. 3.19 using the measured intensity profile. Values of $\langle R_1 \rangle \langle T \rangle$ and γ were obtained from fitting data from the A, B and C sets with the photon number distributions given in eq. 3.24. The fits were quite good and the values of γ obtained from each distribution were the same within statistical errors. The number of photons that would have been scattered had the atom been a pure two-level system (N_p) can be calculated with the spontaneous emission rate for each distribution using eq. 3.19. The slope of a plot of N_p vs. $\langle R_1 \rangle \langle T \rangle$ is the light detection efficiency. This value of efficiency with the value of γ gives the branching ratio of the 5535 A transition of barium.

The beam intensity profiles and excited state occupation probability measurements were used with eq. 3.42 to calculate the expected lineshapes. These predicted lineshapes are compared to the experimental distributions with mixed results.

Photodiode Calibration and Laser Intensity Profile Measurements

The laser power was measured using a Schottky barrier photodiode with an area of one square inch which was calibrated by using a Scientech disk calorimeter (62). The calorimeter calibration factor (.96 mV/mW) was provided by the manufacturer and an internal heating element was built into the device which allowed this calibration factor to be checked. A graph of power reaching the photodiode vs. photodiode voltage reading yields a conversion factor of 4.95±.15 mW/V at 5535 A if the photodiode is followed by a transconductance amplifier with a gain of 10,000 volts/amp.

The laser intensity profiles along the atomic beam were measured by masking the photodiode with a .11 mm radius pinhole. The pinhole size was measured by comparing its area to the area of a larger pinhole with a known diameter. The larger pinhole was masked with the smaller, and both were used to mask a photodiode. This pinhole-photodiode combination was illuminated with a large area laser beam. The power with both in place was noted and since care was taken to insure the pinholes did not overlap, this power was due to the light which passed through the small pinhole. The small pinhole was removed, and the amount of light passing through the large pinhole was then noted. The ratio of the two measurements is the ratio of the pinhole areas.

In order to measure the laser intensity profile, the photodiode and pinhole were mounted upon a micrometer adjustable translation stage which made possible accurate translation of the assembly along the profile. The beam geometry used in this experiment is shown in Fig. 5.1. The light is first spatially filtered with a commercial pinhole-telescope (Jodon LPSF 100) and expanded to the beam size required. In a coordinate system where X is along the laser beam, Z is along the atom beam and Y is perpendicular to both, for the B and C distributions (see list below) the beam was focused to a line parallel to the Z axis one meter from the interaction region with a 4 m cylindrical lens. This left the light rays parallel in the XZ plane and perpendicular to the atomic beam. The 1/2 mm (A distribution) interaction region was produced with the addition of a second 4 m cylindrical lens which focused the light into a line parallel to the Y axis at the atomic beam, i.e., minimized the length of the interaction region. This arrangement made the laser beam width much larger than the atomic beam diameter (.26 mm) at the interaction region which insured that all atoms experienced the same laser intensity profile. This profile in the Z direction was approximately Gaussian with a half width at half maximum of $D_{1/2}$ (see below). The beam sizes and total input powers used are listed below:

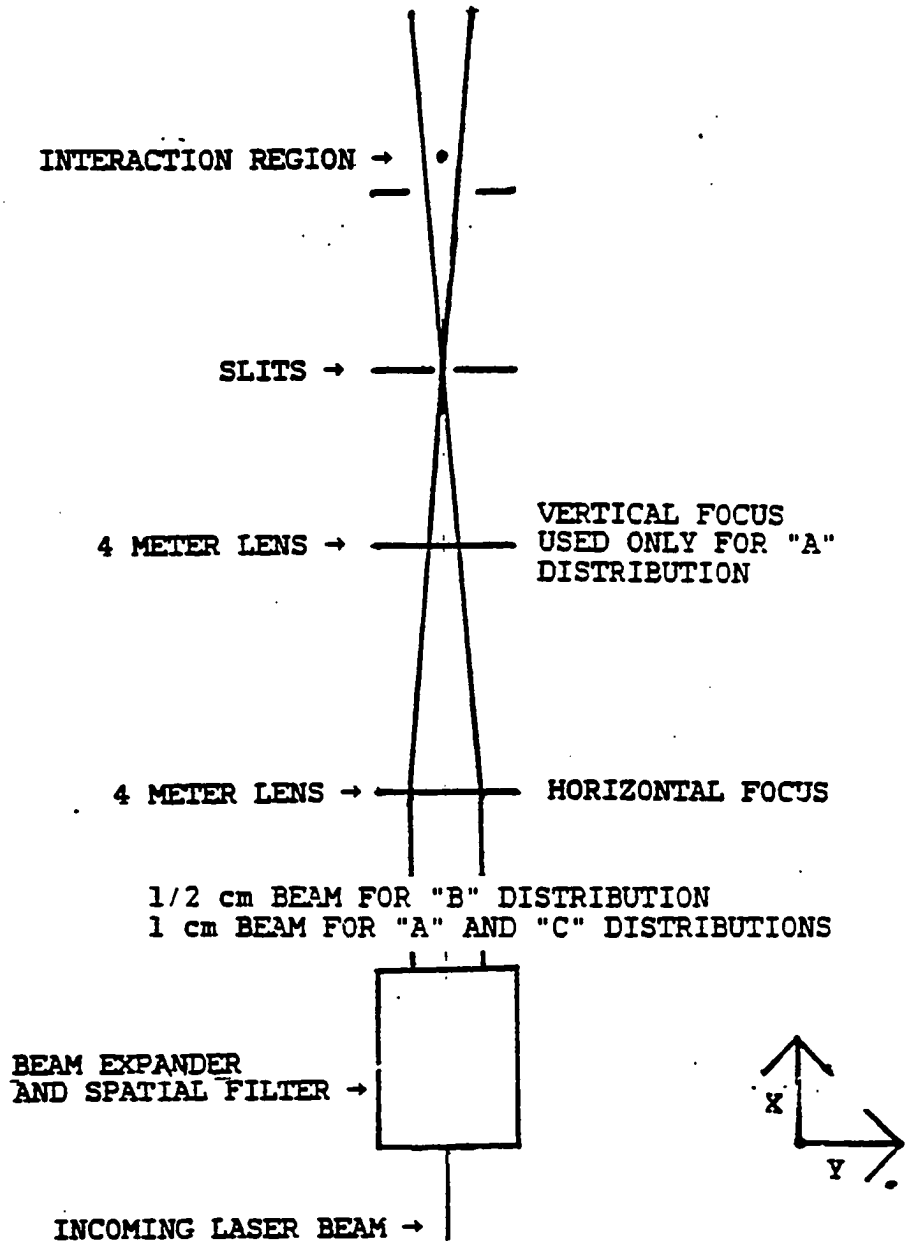

Figure 5.1 Laser beam optics chain

Label	$D_{1/2}$	Input Power	Max. Intensity
A1	.26 mm	.3 mW	.36 mW/mm^2
A2	.26 mm	1.0 mW	1.2 mW/mm^2
A3	.26 mm	4.0 mW	4.8 mW/mm^2
B1	1.5 mm	1.25 mW	.49 mW/mm^2
B2	1.5 mm	2.5 mW	.98 mW/mm^2
B3	1.5 mm	5.0 mW	1.96 mW/mm^2
C1	2.8 mm	5.0 mW	.56 mW/mm^2
C2	2.8 mm	10.0 mw	1.13 mW/mm^2
C3	2.8 mm	12.5 mW	1.41 mW/mm^2.

The atomic flux can be obtained by dividing the total resonance fluorescence count rate (minus background) by the average number of photons scattered per atom ($\langle n \rangle$). The flux was kept between one and two hundred atoms/sec for the extended (B and C) distributions to avoid multiple atoms in the beam.

Upper Level Population Probability

The resonance fluorescence from a short interaction region was measured as a function of input power. The laser was locked to the center of the transition ($\Delta=0$) with the atomic flux held constant. A 1/2 mm interaction region was used to minimize optical pumping and momentum effects. From Chapter III the number of photons scattered by atoms moving through this short interaction region is

$$\langle R_1\rangle\langle T\rangle = A_1 \int_{-\infty}^{+\infty} \frac{KI_0 e^{-(z/D)^2}}{1+2KI_0 e^{-(z/D)^2}}\, dz,$$

with $A_1 = N_0 \varepsilon A\langle T\rangle$, where N_0 is the number of atoms that passed through the beam. The factor A_1 is considered to be the same for all measurements, K has the value of 1.97 mm^2/mW for the barium 5535 A transition and I_0 was measured for each power using the .11 mm pinhole. The laser frequency width is extremely small on the time scale of an atomic transit (a few μsec), but acoustic noise does change it on the msec scale. This broadens the laser frequency into the Gaussian distribution with a FWHM of 7 MHz shown in Fig. 2.8. If the laser linewidth is included the scattering rate is given by:

$$\langle R_1\rangle_\omega\langle T\rangle = A_1/(\Gamma_L\sqrt{\pi}) \int_{-\infty}^{+\infty} d\omega \int_{-\infty}^{+\infty} dz \frac{KI_0\, e^{-(z/D)^2} e^{-[(\omega-\omega_L)/\Gamma_L]^2}}{1+2KI_0 e^{-(z/D)^2 + 4(\omega-\omega_0)^2/A^2}}.$$

The parameter Γ_L is the laser 1/e frequency width (4.2 MHz) and ω_L is the laser central frequency. Since the laser is locked to the atomic resonance ω_L is equal to ω_0. The data are compared with calculations in Fig. 5.2. Since the laser linewidth (7 MHz FWHM) is much smaller than the natural linewidth (19 MHz FWHM), the calculated values for $\langle R_1\rangle\langle T\rangle$ and $\langle R_1\rangle_\omega\langle T\rangle$ are essentially the same. The only unknown parameter is the product $A_1 = N_0 \varepsilon A\langle T\rangle$ which sets the overall normalization. This has been adjusted to fit the data. The close agreement even for high input powers indicate that the

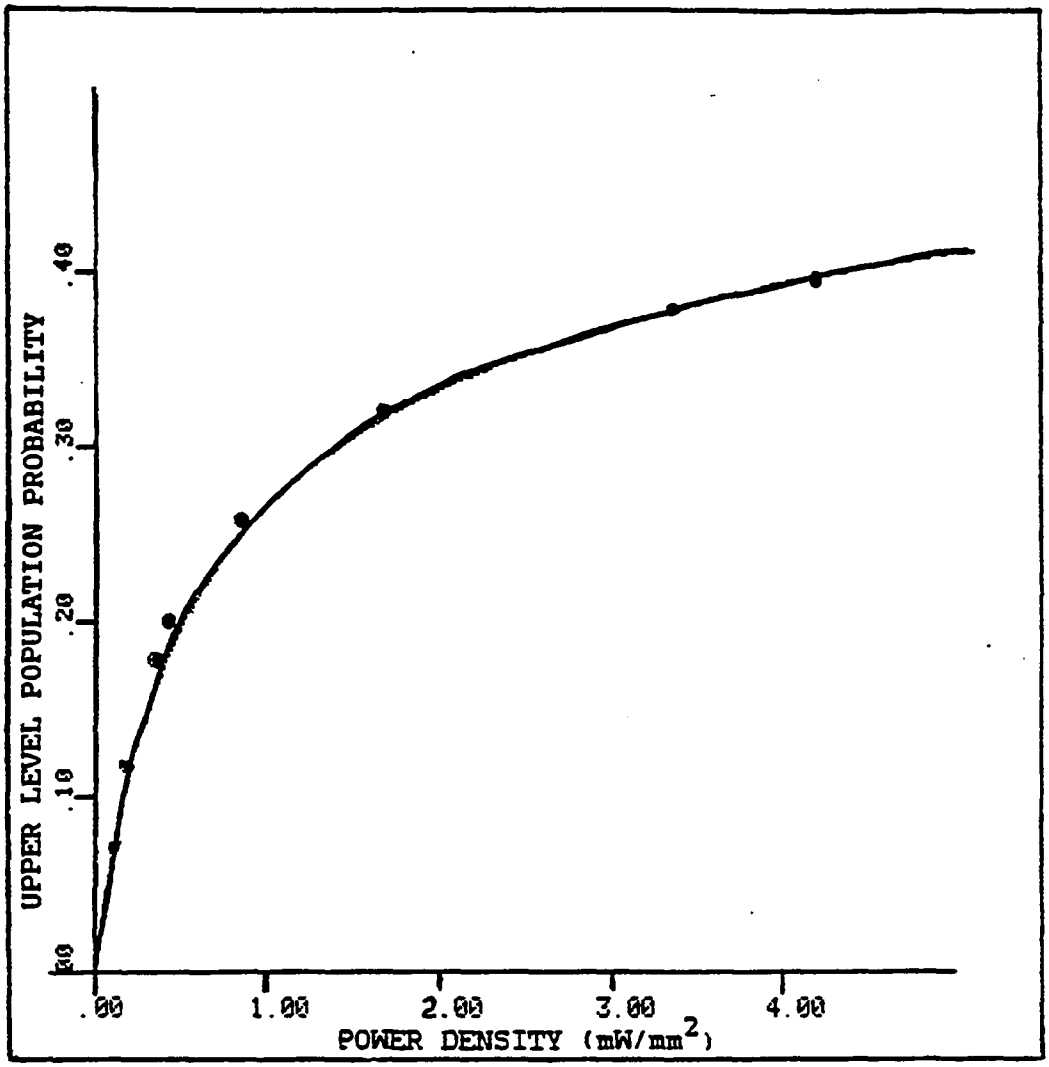

Figure 5.2 Atomic upper level population probability as a function of power at center of laser beam

two-level approximation is valid for short interaction regions. This also is confirmed by the photon number distributions described below.

Photon Number Distributions

The photon number distributions were found using the number of counts at ν_{max}, the peak of the Doppler shifted fluorescence curve. These are fit using the equation for photon probability in a three-level system derived in Chapter III (3.24) after background interference effects have been removed as described in Chapter IV. For each laser intensity distribution values of $\langle R_1 \rangle \langle T \rangle$ and γ were obtained by minimizing χ^2. In Fig. 5.3a-c χ_ν^2 ($\chi_\nu^2 = \chi^2/N_f$, where N_f is the number of degrees of freedom) vs. γ are shown. The value of $\langle R_1 \rangle \langle T \rangle$ used to obtain the function $\chi_\nu^2(\gamma)$ is the one which minimizes χ_ν^2 for that particular γ. Near this minimum the function $\chi_\nu^2(\gamma)$ is only very weakly dependent upon $\langle R_1 \rangle \langle T \rangle$. Since $\chi_\nu^2(\gamma)$ is weakly dependent upon $\langle R_1 \rangle \langle T \rangle$, the error in γ is given by (63)

$$\sigma_\gamma^2 = \frac{2}{(\partial^2 \chi_\nu^2(\gamma)/\partial \gamma^2)}.$$

The γ given below is the overall minimum for each data set.

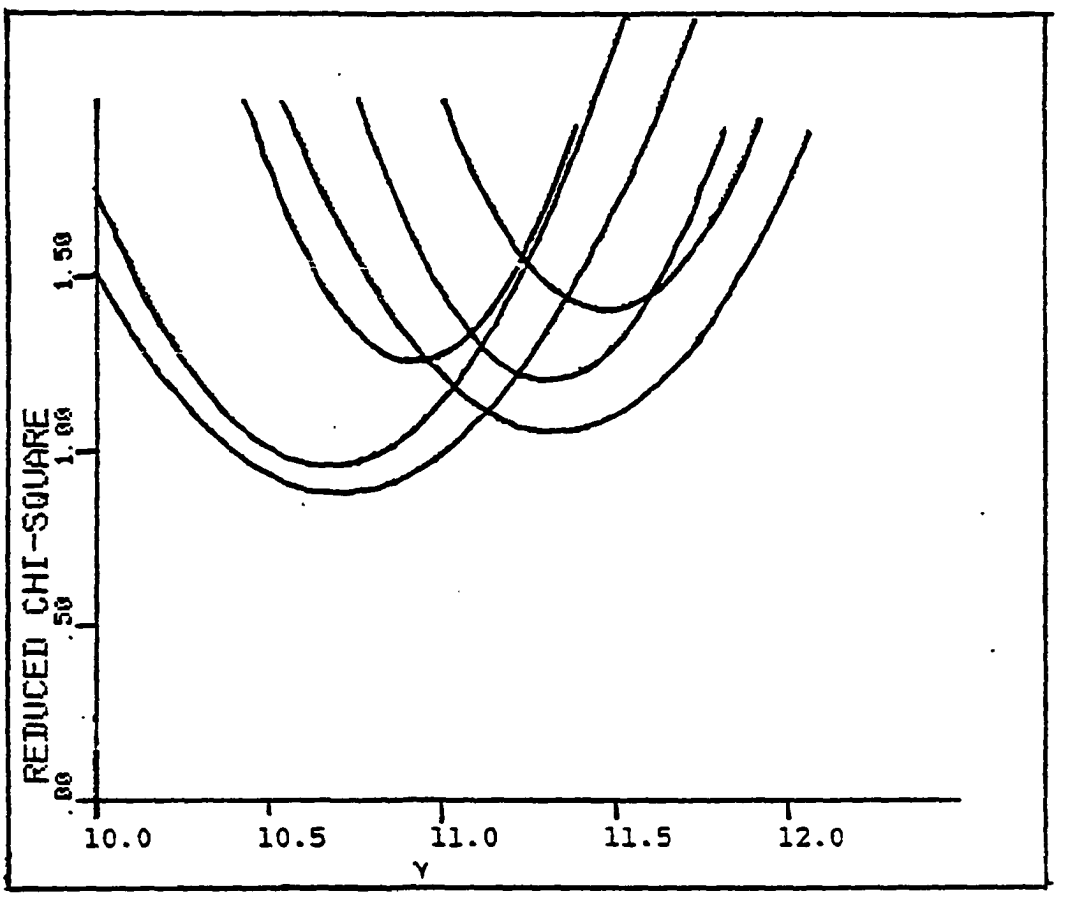

Figure 5.3a Chi-Square vs. Gamma for the six extended beam profiles

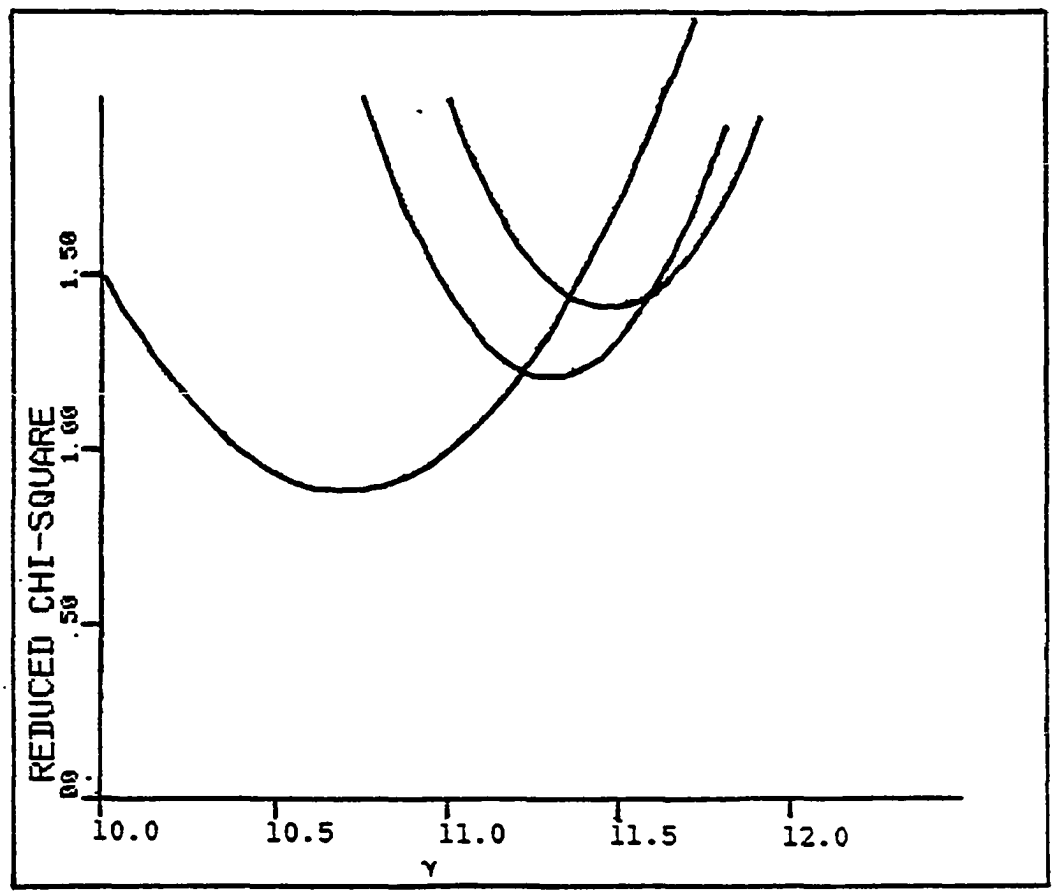

Figure 5.3b Chi-Square vs. Gamma for the "B" distributions. The curves from left to right are B3, B1, B2

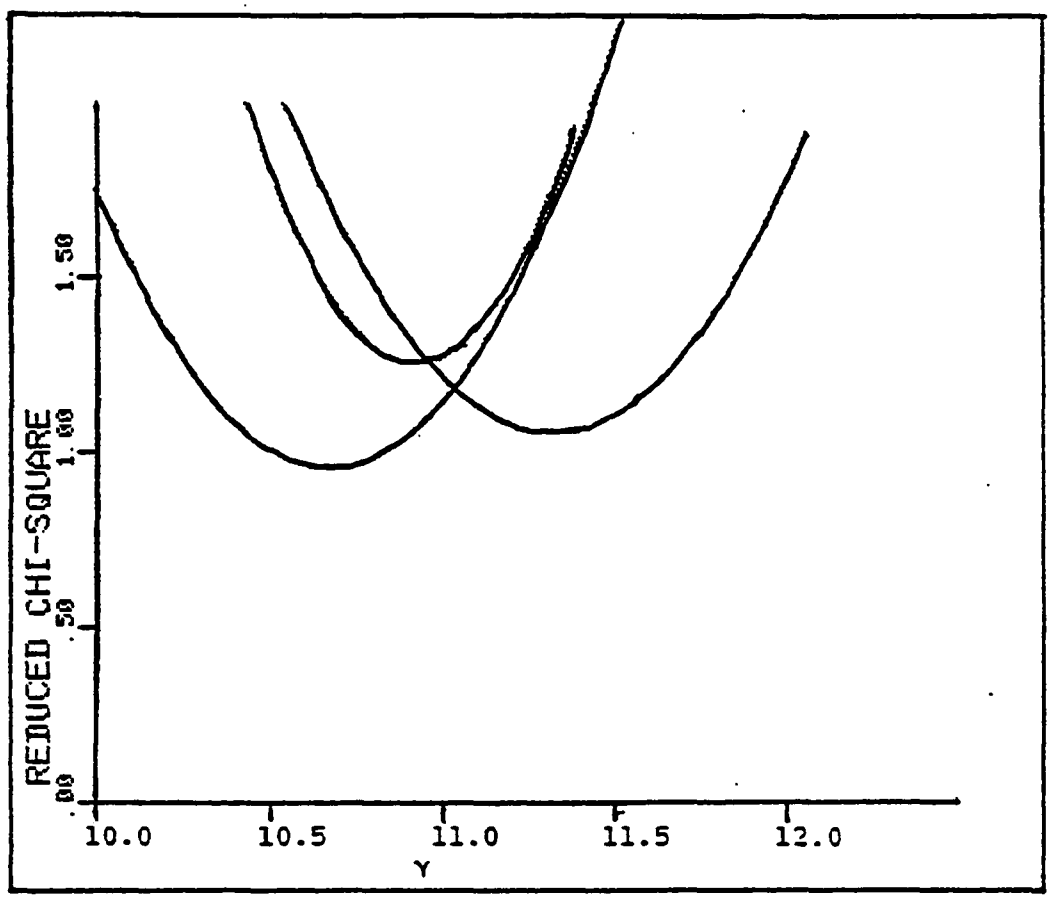

Figure 5.3c Chi-Square vs. Gamma for the "C" distributions. The curves from left to right are C3, C1, C2

DISTRIBUTION	GAMMA	σ_γ
B1	11.30	.37
B2	11.47	.36
B3	10.70	.78
C1	10.93	.32
C2	11.33	.64
C3	10.67	.56

The average value of γ is given by (63)

$$\bar{\gamma} = \frac{\Sigma_i \, (\gamma_i/\sigma_i^2)}{\Sigma_i \, (1/\sigma_i^2)}$$

and the average sigma is similarly found with the equation (63)

$$\bar{\sigma}_\gamma^2 = \frac{1}{\Sigma_i \, (1/\sigma_i^2)} \quad .$$

The average γ obtained is 11.1±.2. The "A" distributions, due to the low number of photons scattered are not sensitive to γ and were not included in this average. The $\langle R_1 \rangle \langle T \rangle$ value for each distribution was found holding γ=11.

Photon number distributions are shown in the following Figs.(5.4a-5.4i). The solid line is the calculation and the vertical lines are data points with error bars. The error bars are equal to the square root of the number of counts (background + signal) in the channel that these graphs are based upon. The lower multiplicities have large error bars

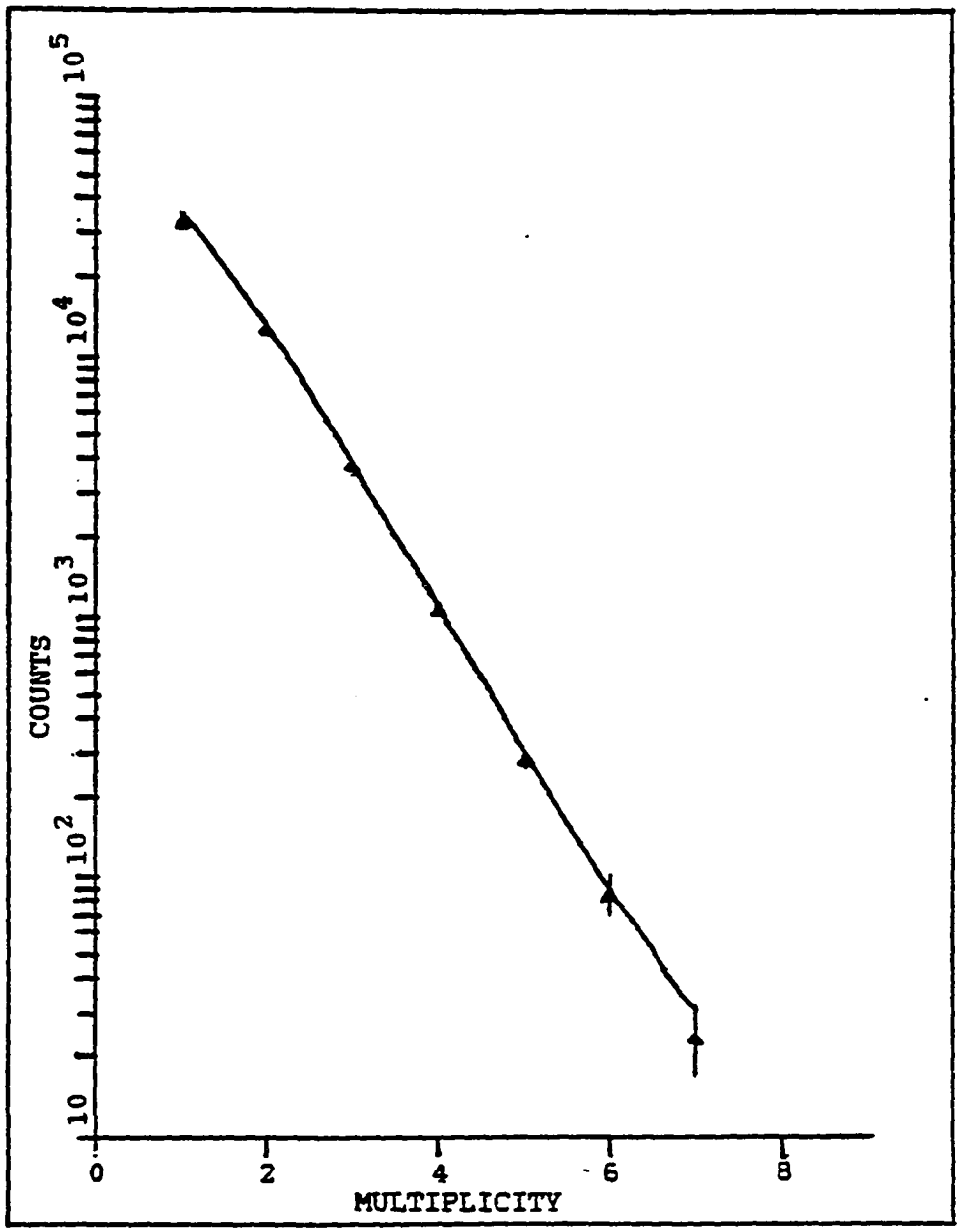

Figure 5.4a Beam Profile Al, R_1T= .75, γ=11.0

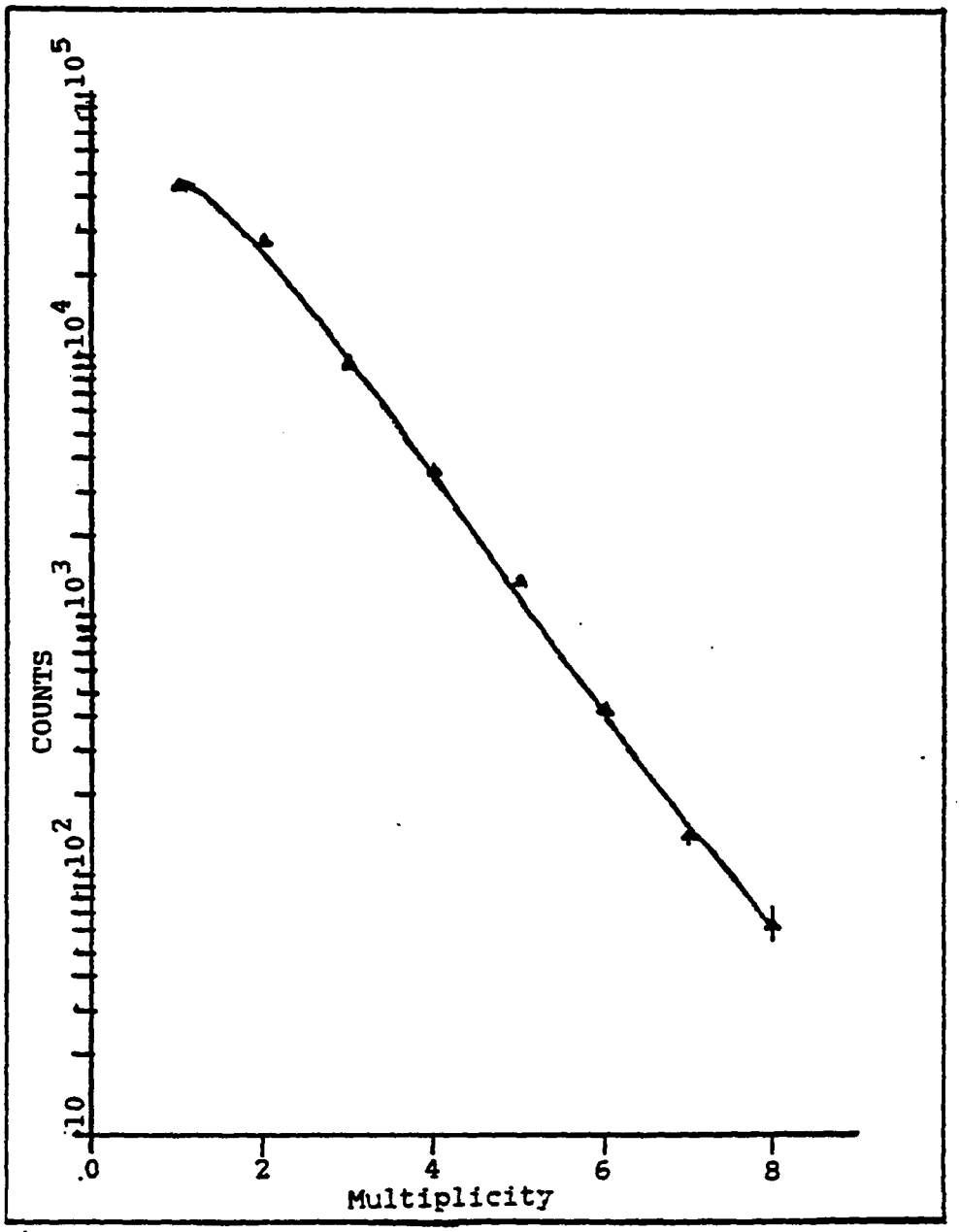

Figure 5.4b Beam Profile A2, R_1T= 1.1, γ=11.0

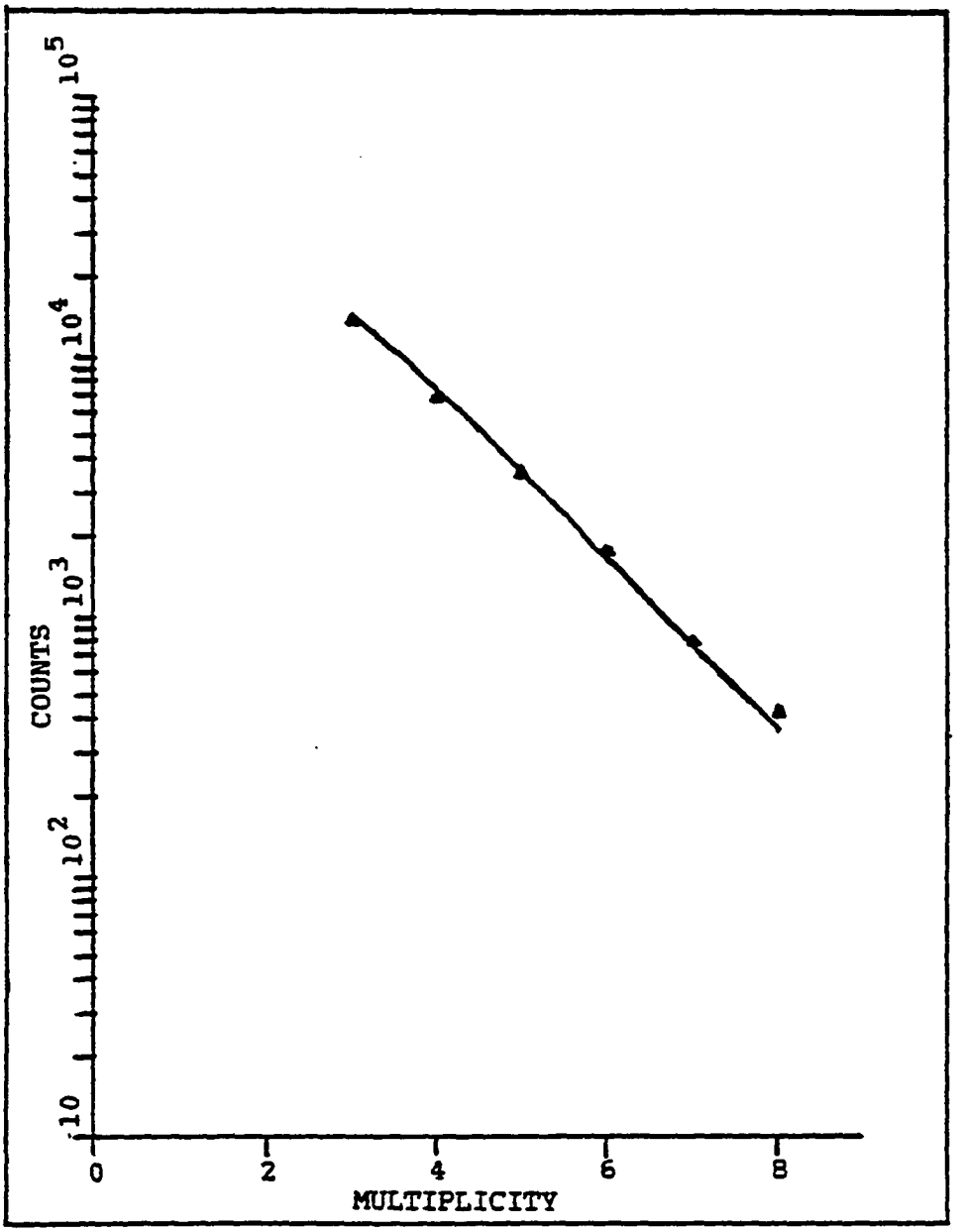

Figure 5.4c Beam Profile A3, R_1T= 2.0, γ=11.0

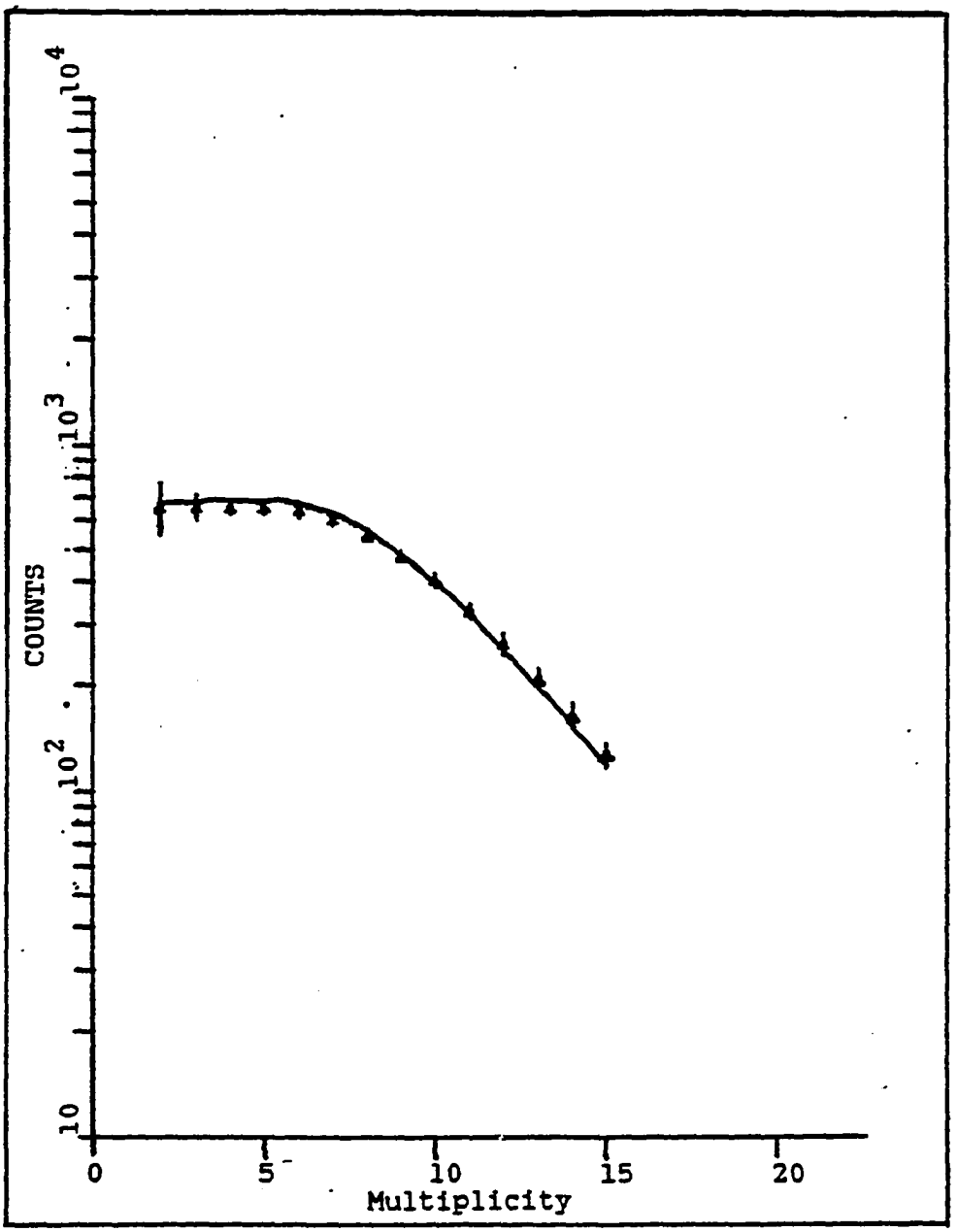

Figure 5.4d Beam Profile B1, R_1T= 10.5, γ=11.0

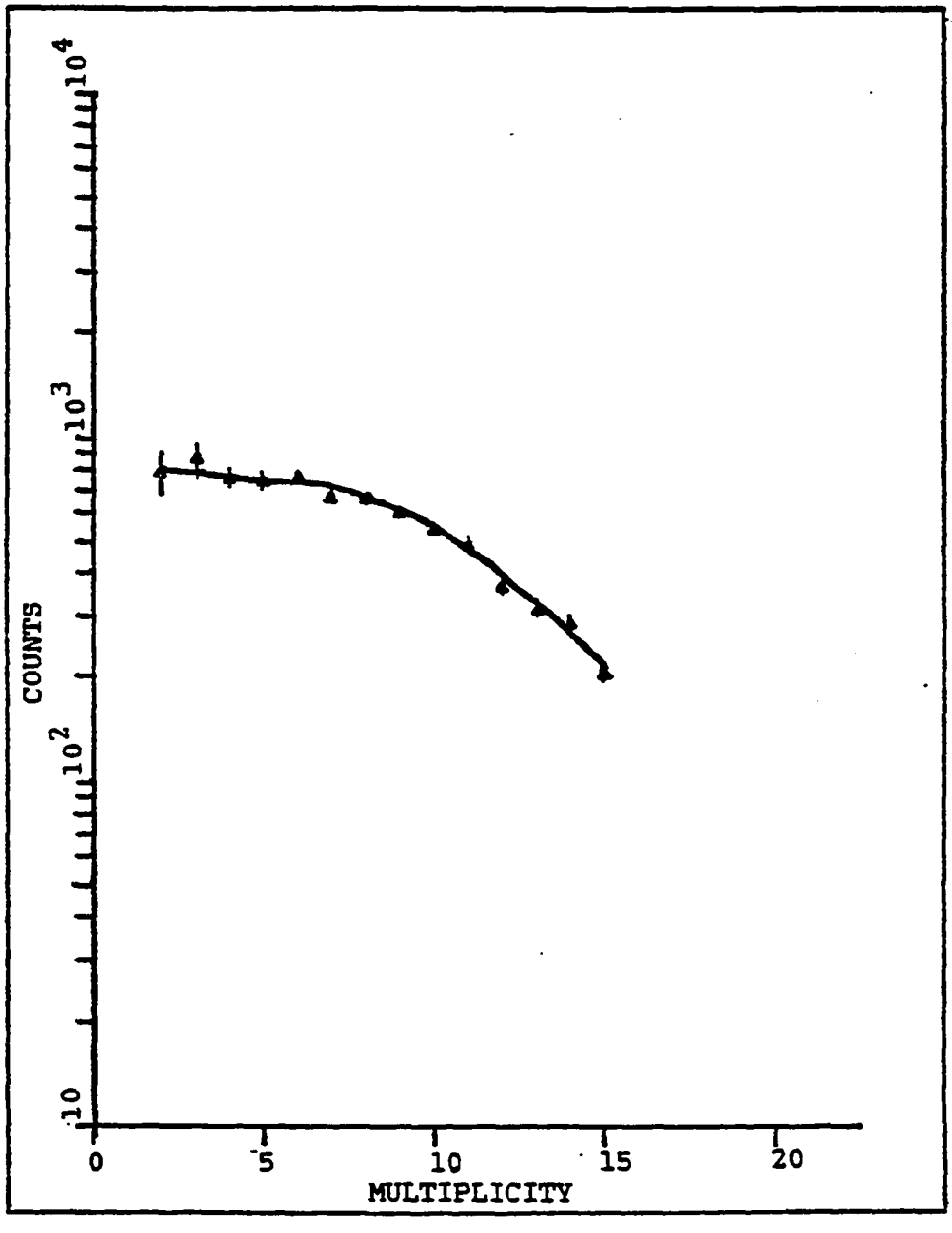

Figure 5.4e Beam Profile B2, R_1T= 13.0, γ=11.0

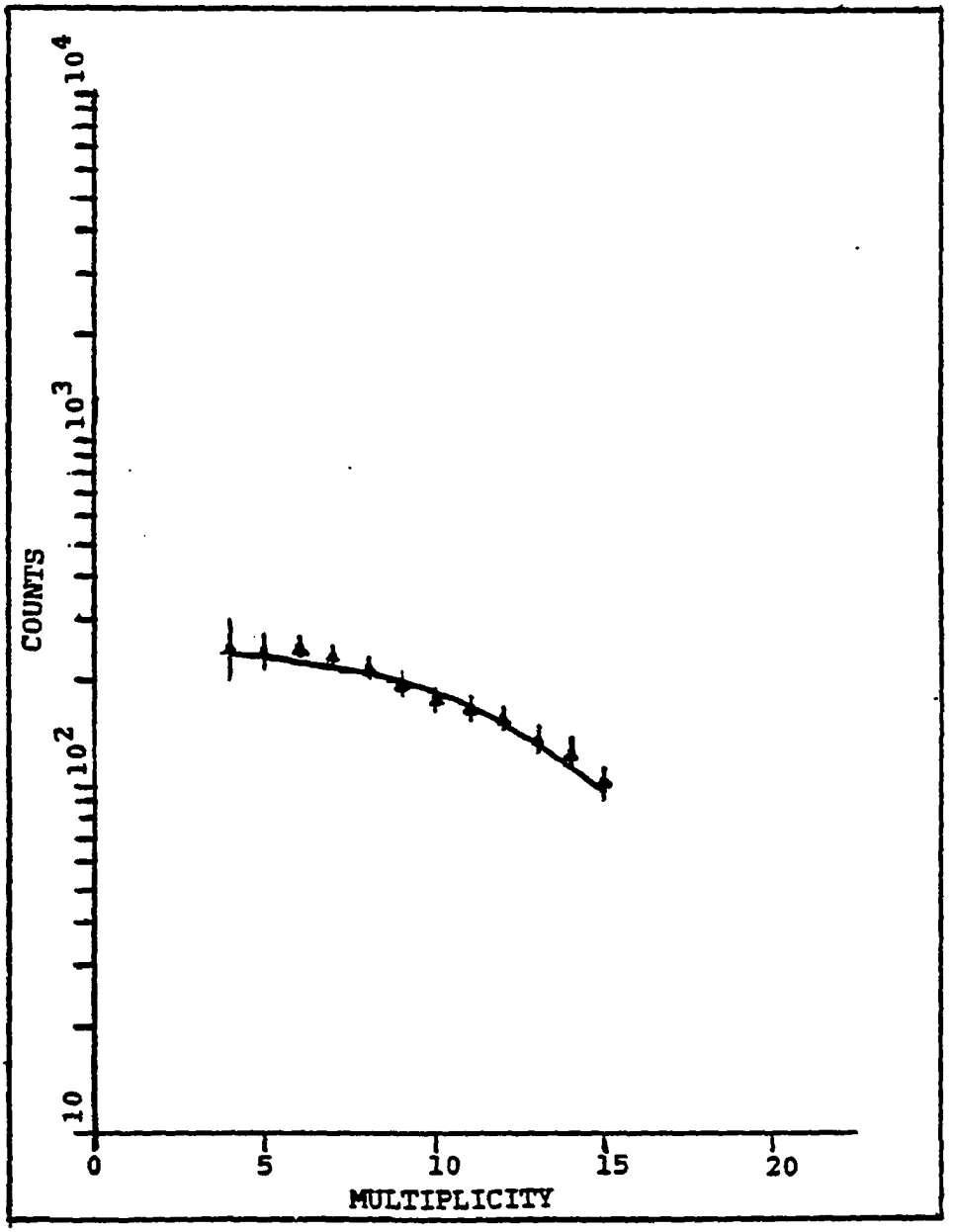

Figure 5.4f Beam Profile B3, R_1T= 17.0, γ=11.0

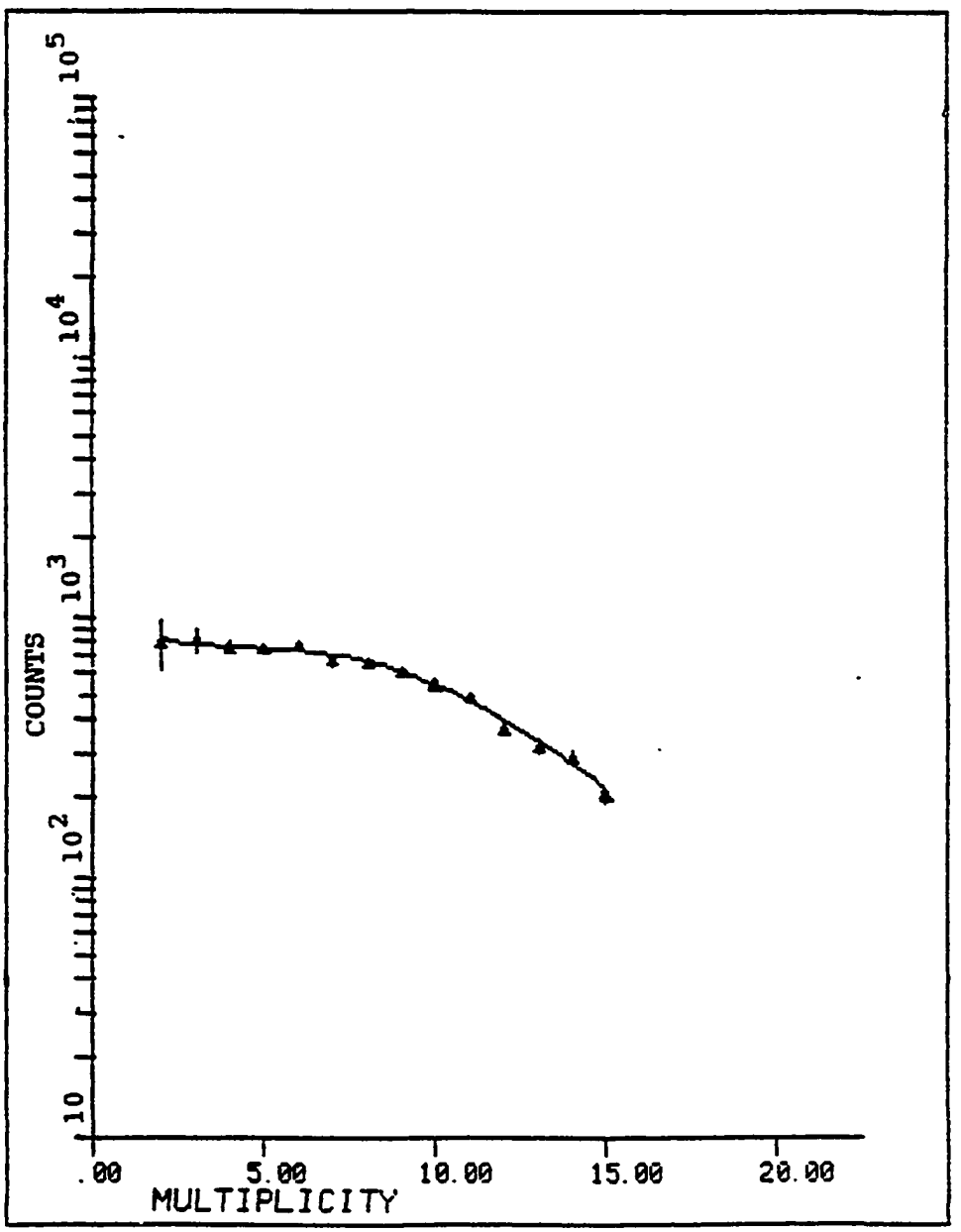

Figure 5.4g Beam Profile Cl, R_1T= 16.5, γ=11.0

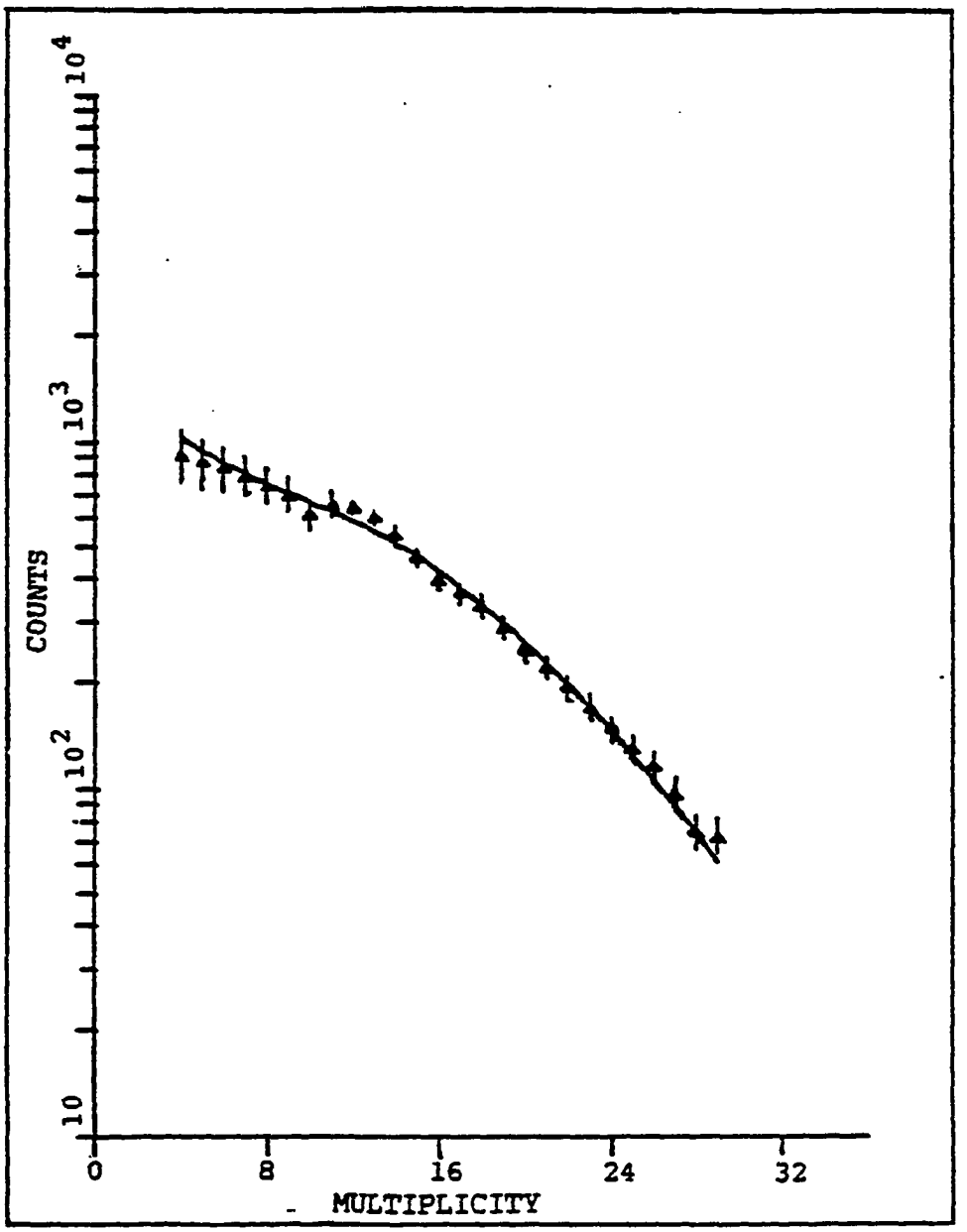

Figure 5.4h Beam Profile C2, R_1T= 23.5, γ=11.0

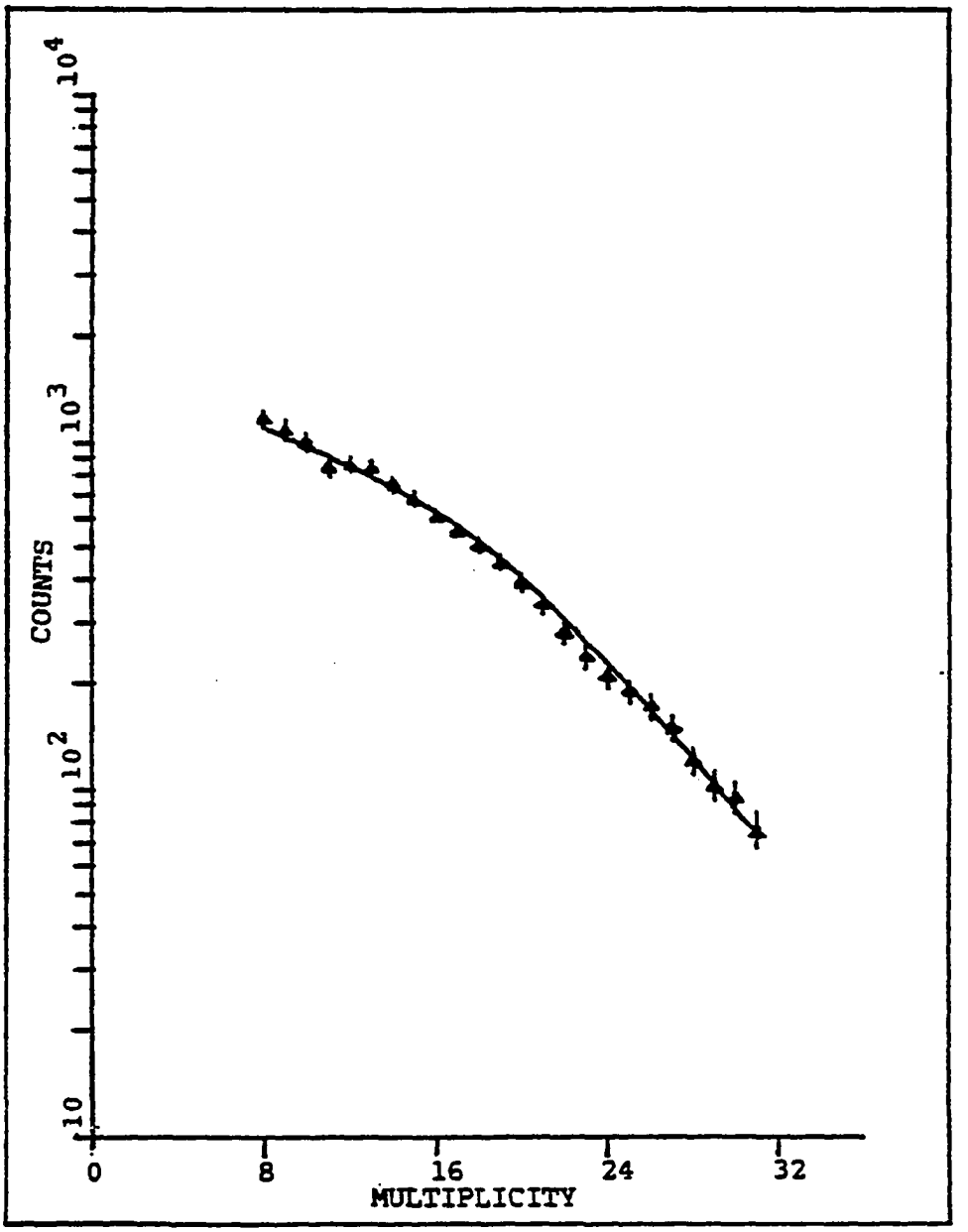

Figure 5.4i Beam Profile C3, R_1T= 25.0 ,γ=11.0

because of the large background in comparison to peak height at these multiplicities. The channel used was the best estimate of ν_{max}. As discussed in Chapter III, this frequency is characterized as a relative minimum in the low multiplicities, and a relative maximum in the high multiplicities.

The relationship between the barium branching ratio (x) and γ is $x = \gamma/\varepsilon$. The number of photons scattered by the atom as it passes through the laser beam in an extended interaction region, if there were no optical pumping, is N_p. As previously discussed in this chapter, the atomic transition linewidth is much larger than the laser linewidth, making it unnecessary to average over the laser linewidth. Two methods of calculating N_p are discussed in Chapter III: (1) for an infinitely massive atom equation 3.19 can be used and (2) for an atom for which radiation pressure is a factor, equation 3.45 must be used. The number of photons scattered was calculated using both equations. The results taking into account the finite mass of the atom are roughly 10% lower than the infinite mass atom for large $\langle n \rangle$. A graph of $\langle R_1 \rangle \langle T \rangle$ vs. N_p should be a straight line with slope ε.

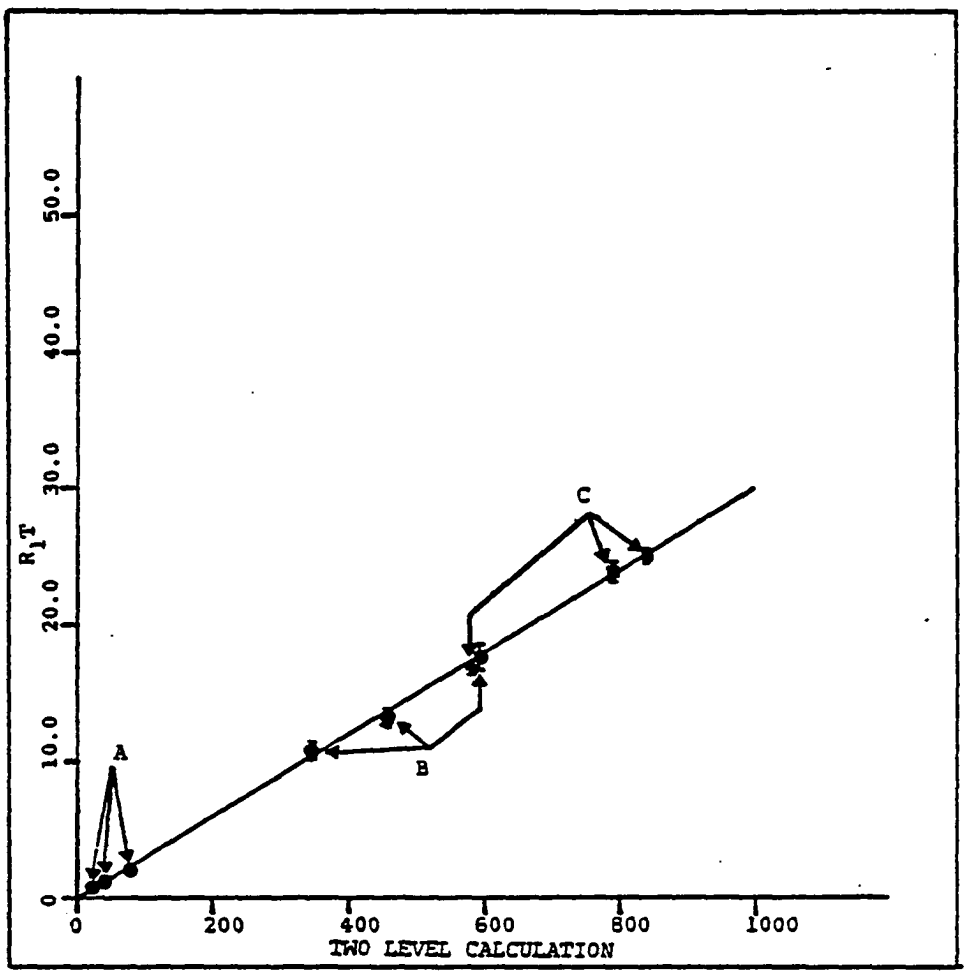

Figure 5.5 Graph of atomic scattering rate vs. N_p. The slope of the line is the system light detection efficiency

Label	$\langle n \rangle$	$\langle R_1 \rangle \langle T \rangle$	Photons Scattered(Np)	
			Finite	Infinite
A1	.8	.75 ± .03	22.3	22.3
A2	1.1	1.10 ± .04	37.6	37.6
A3	1.9	2.00 ± .06	74.2	74.2
B1	6.4	10.7 ± .6	344.6	379.5
B2	7.4	12.8 ± .7	454.3	509.3
B3	8.1	17.2 ± 1.0	589.7	650.2
C1	8.2	16.7 ± .5	576.5	641.9
C2	9.7	23.8 ± .7	787.3	867.4
C3	9.8	25.1 ± .5	837.6	935.1

The parameter $\langle n \rangle$ is $\Sigma_{n=0}^{+\infty} nP(n)$, the average number of photons scattered for each laser beam intensity. For a two-level atom $\langle n \rangle$ is equal to $\langle R_1 \rangle \langle T \rangle$. The experimental distributions do not extend to zero, nor to infinity so the value of $\langle n \rangle$ given in the table above is

$$\langle n \rangle = \frac{\Sigma_{n=a}^{b} nP(n)_{exp}}{\Sigma_{n=a}^{b} nP(n)_{theory}} \left(\Sigma_{n=0}^{+\infty} nP(n)_{theory}\right)$$

where a and b are the limits of the experimental distribution. The relationship between $\langle R_1 \rangle \langle T \rangle$ and N_p is graphed in Fig. 5.5. The function is $\langle R_1 \rangle \langle T \rangle = \varepsilon N_p$, where ε is .0295 ± .0007. The error given is the statistical error of the fit; the uncertainties in the input power and laser beam size introduce larger errors than this. A more reasonable

estimate for the uncertainty is σ_ε=.0015 (a 5% error rather than a 2.5% error). Using this value for the efficiency and the previously quoted value of γ, the branching ratio obtained is

$$(1-x)/x=375 \pm 30.$$

Lineshape, Data and Calculations

The linewidth of the atomic transition is greatly affected by the input power. From eq. 3.35, the FWHM of the resonance is given by

$$FWHM=(A/2\pi)(1+2\Omega^2/A^2)^{1/2}$$

The increase of linewidth with intensity is called power broadening. In Fig. 5.6, two peaks of multiplicity 15 are shown. The wide curve was measured with the highest power density used in this series of experiments and the narrow curve was measured with the lowest. Even at this high multiplicity the wide curve has a FWHM of 46 MHz. This 46 MHz width is not totally due to power broadening. The $\langle R_1 \rangle \langle T \rangle$ value for this curve is seventeen, and since the multiplicity is fifteen, the linewidth is broadened by the effects of the photon-burst function (Chapter III). The narrow curve has a FWHM of 12 MHz which is smaller than the natural linewidth (19 MHz FWHM).

In the previous calculations of numbers of photons scattered, the linewidth of the laser could be ignored, as previously shown in this chapter. This is possible because the fluorescence curve is flat near the center and does not

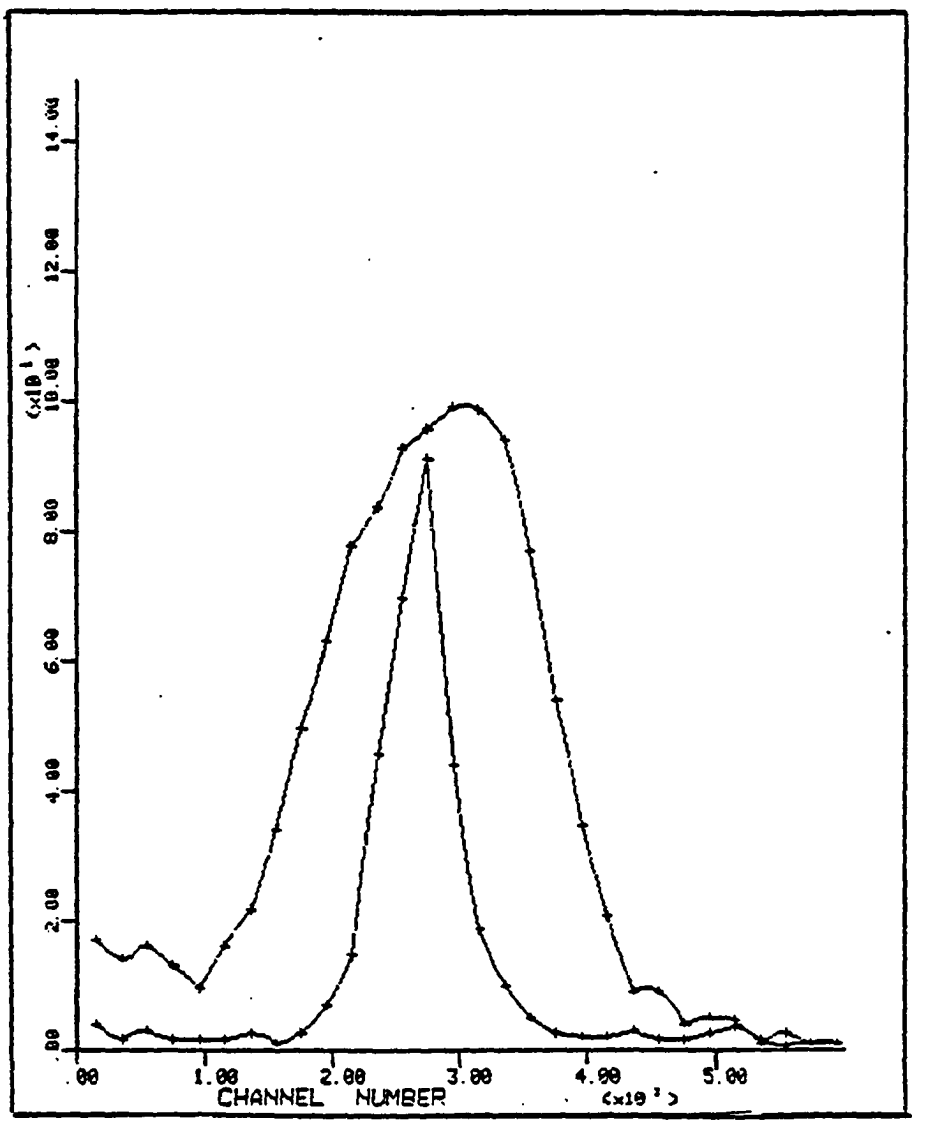

Figure 5.6 Two multiplicity 15 peaks taken with different input power densities. The narrow peak was taken with the low power density

hange appreciably on the scale of the laser linewidth if ω_L equals ω_0. Farther from the resonance center the scattering rate changes significantly within the span of the laser linewidth. This makes it necessary to include the laser linewidth in the calculation of individual burst spectra lineshapes.

The number of events of multiplicity n depends only on $\langle R_1(\nu)\rangle\langle T\rangle$,γ, and the total number of atoms N_0. In the calculations of burst spectra lineshapes $\langle R_1(\nu)\rangle\langle T\rangle$ was evaluated using equation 3.42 which includes radiation pressure effects. These lineshapes are asymmetric and the double humped low multiplicity spectra have unequal hump heights after laser linewidth is included. Since γ and N_0 were determined by fitting the peak heights, there are no free parameters in these calculations. Examples from the B1 and B2 are shown in Figs. 5.7a-g. The backgrounds were lowest for these two runs minimizing the effects of background interference. A comparison of the measured and calculated peak width for the B1 distribution is shown in Fig. 5.8.

The calculated curves fit the measured peaks fairly well near the peak of the resonance but the data consistently fall below the predictions at larger frequency differences from line center. This is caused by chain breaking. The reset time was set to eliminate breaks at the highest rates, i.e., at the peak of the curve. Far from line center the

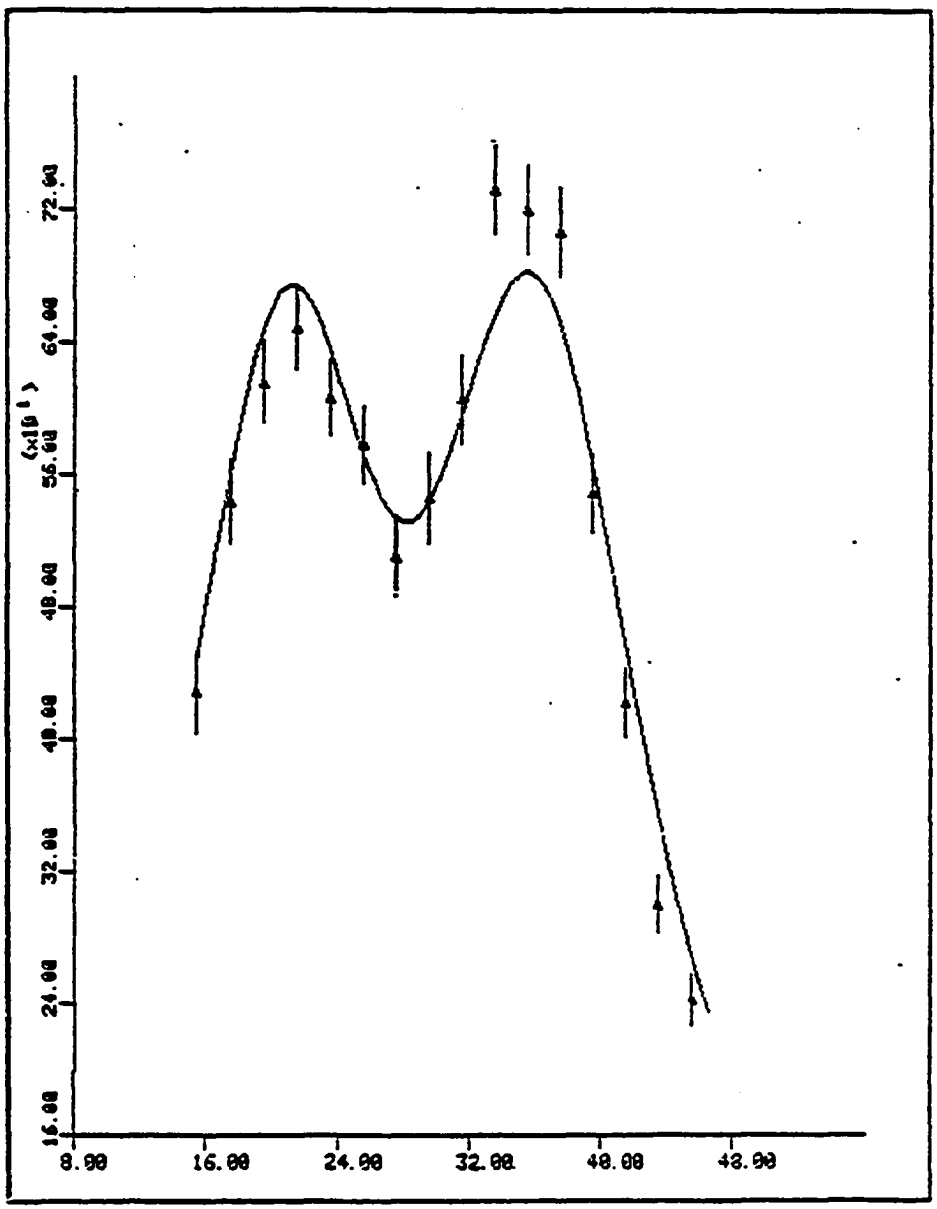

FIG. 5.7a Distribution B1. Multiplicity 5
The horizontal scale is channnel number each channel is 2.26 MHz. and the vertical scale is the number of counts

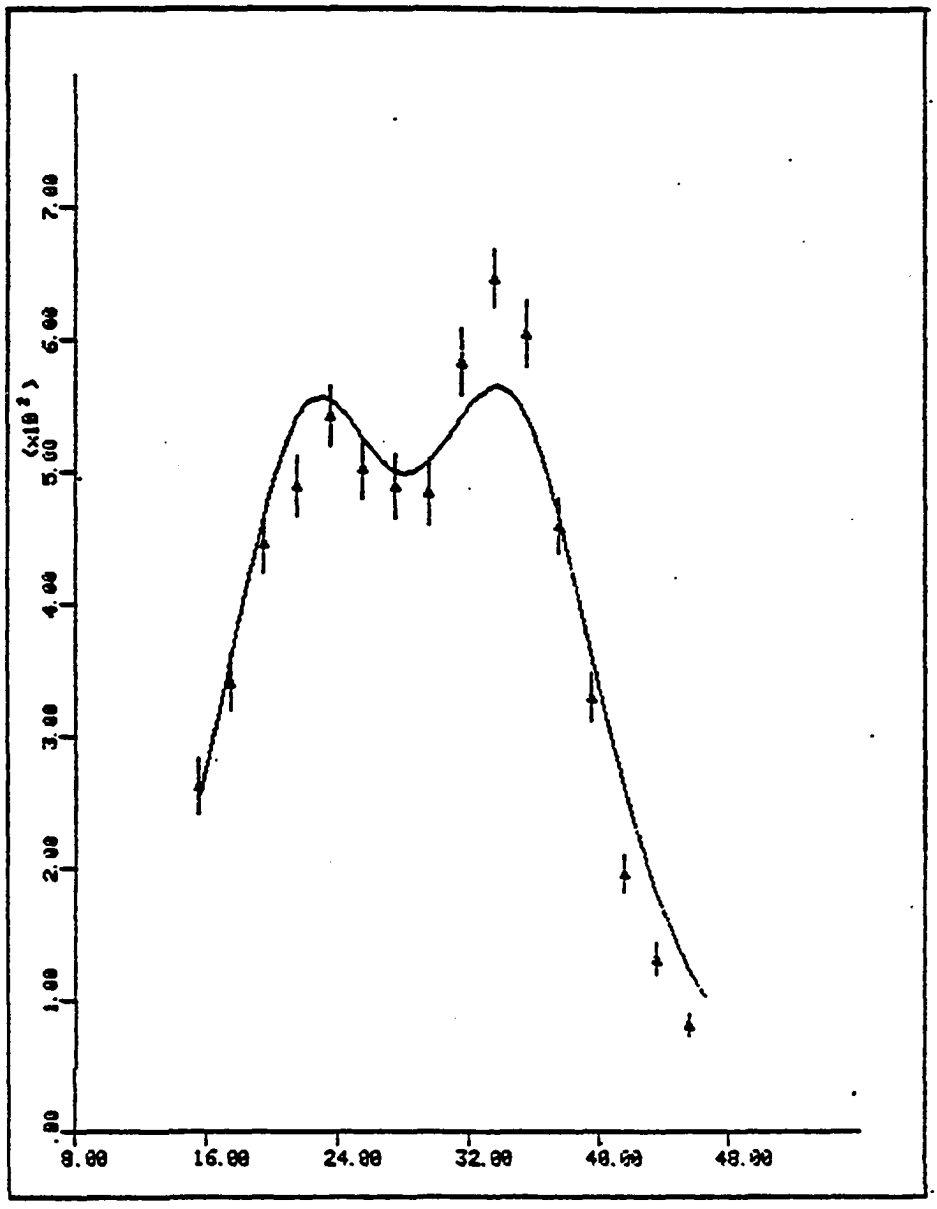

FIG. 5.7b Distribution B1, Multiplicity 6

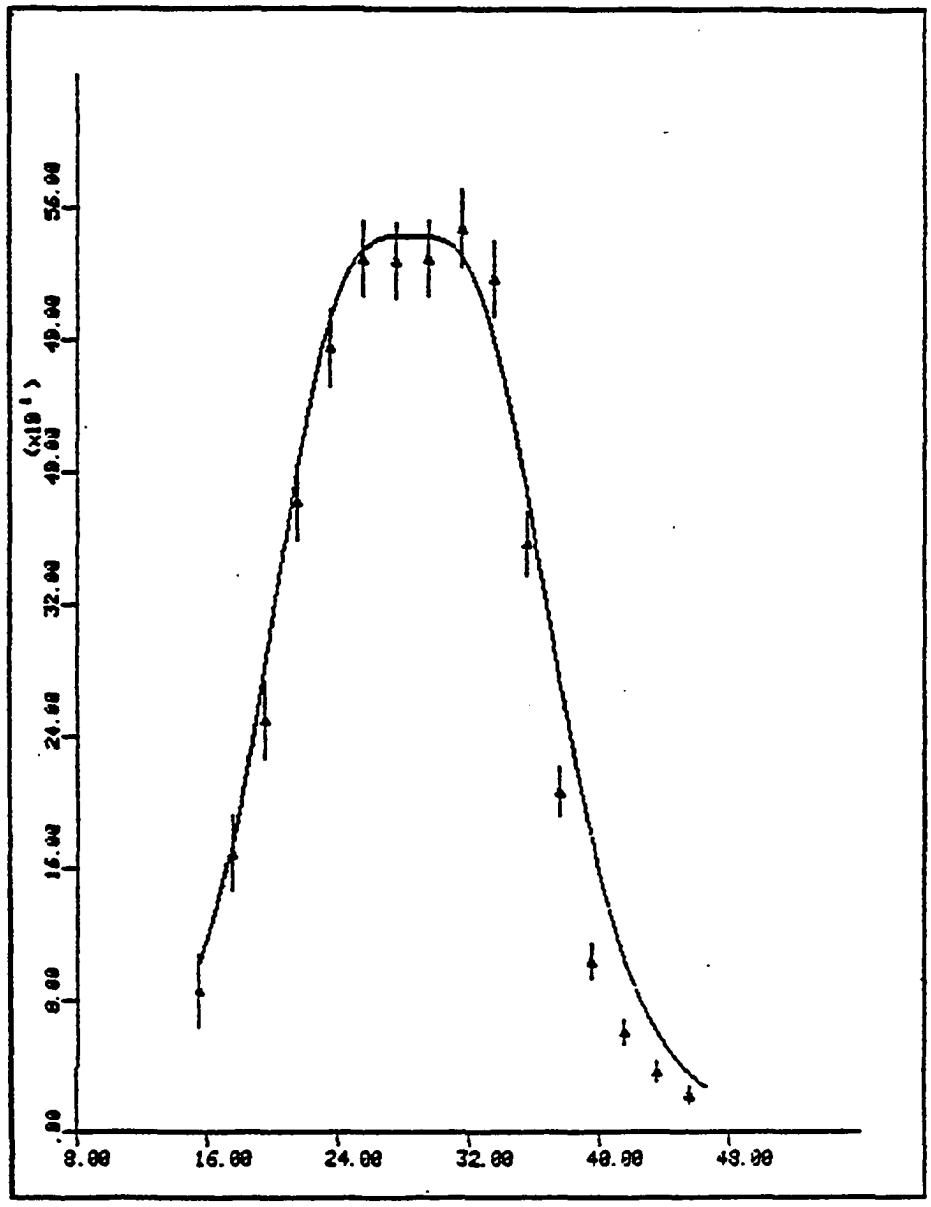

FIG. 5.7c Distribution B1. Multiplicity 8

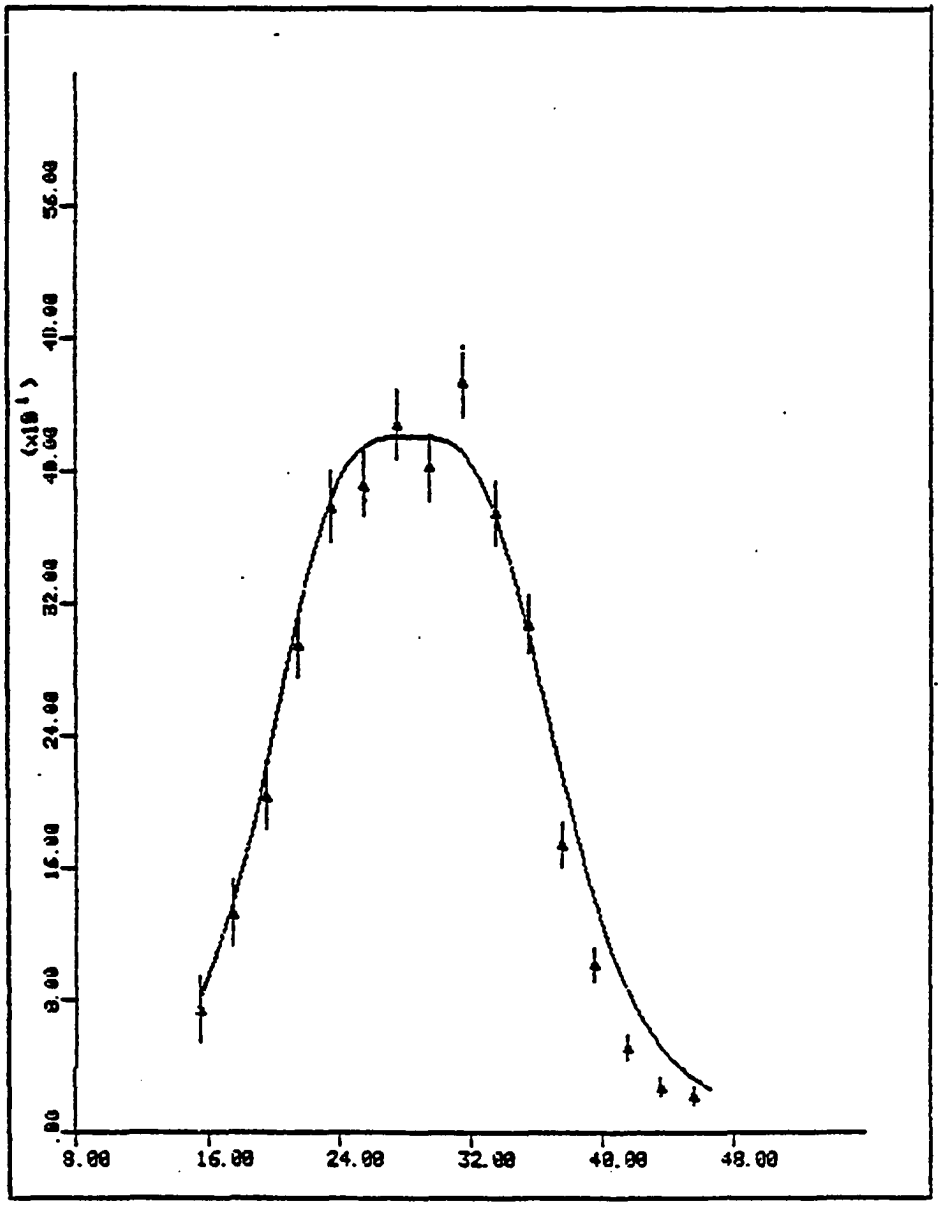

FIG. 5.7d Distribution B1, Multiplicity 9

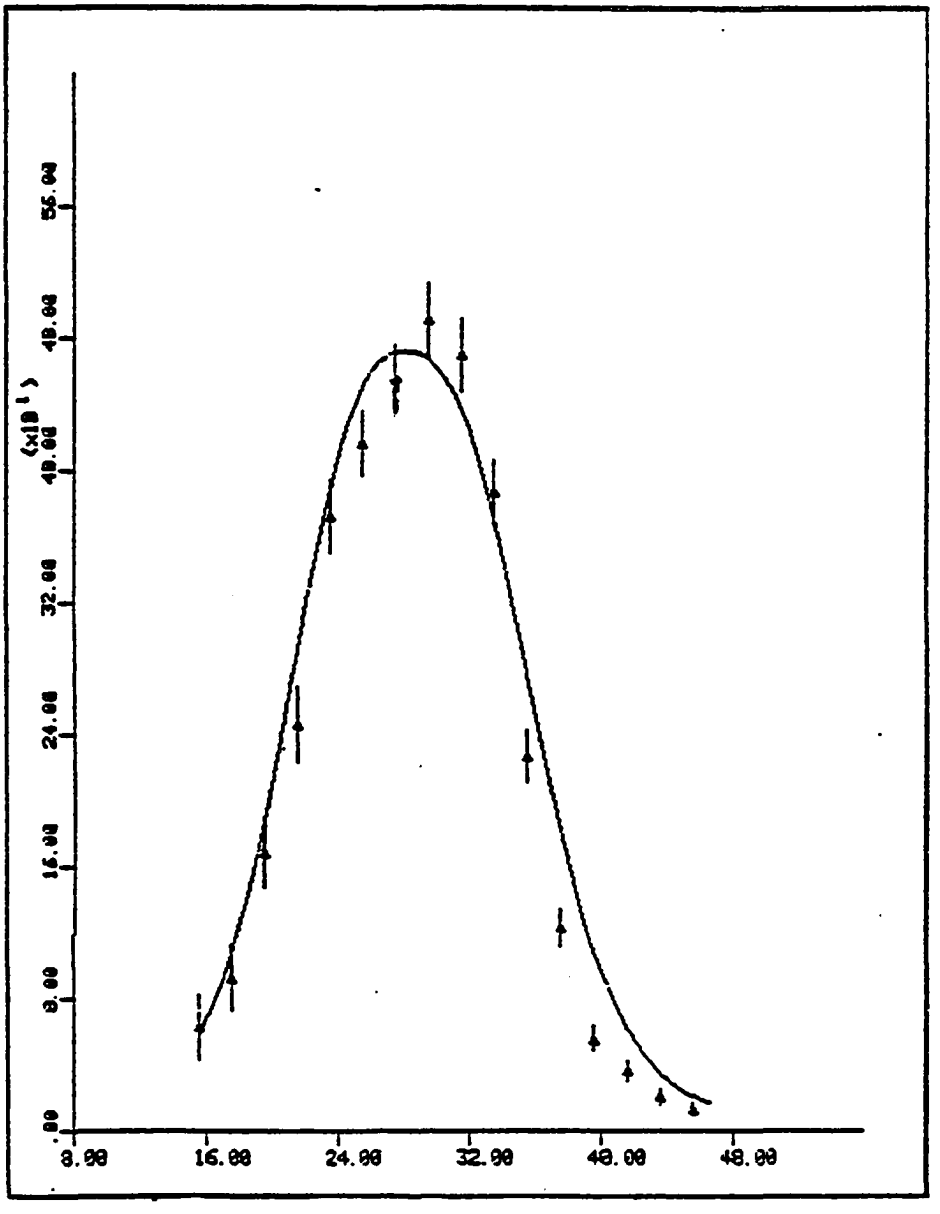

FIG. 5.7e Distribution B1, Multiplicity 10

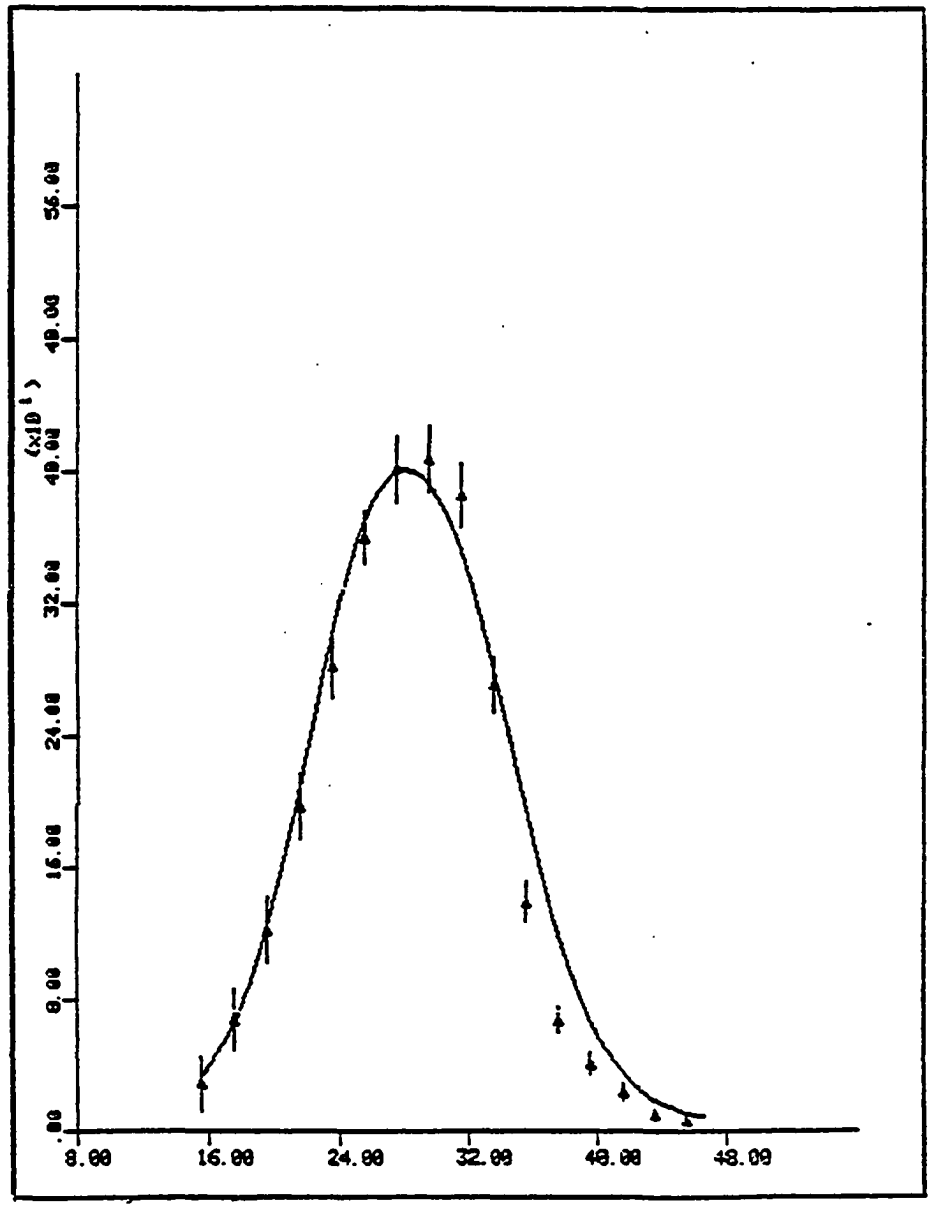

FIG. 5.7f Distribution B1. Multiplicity 11

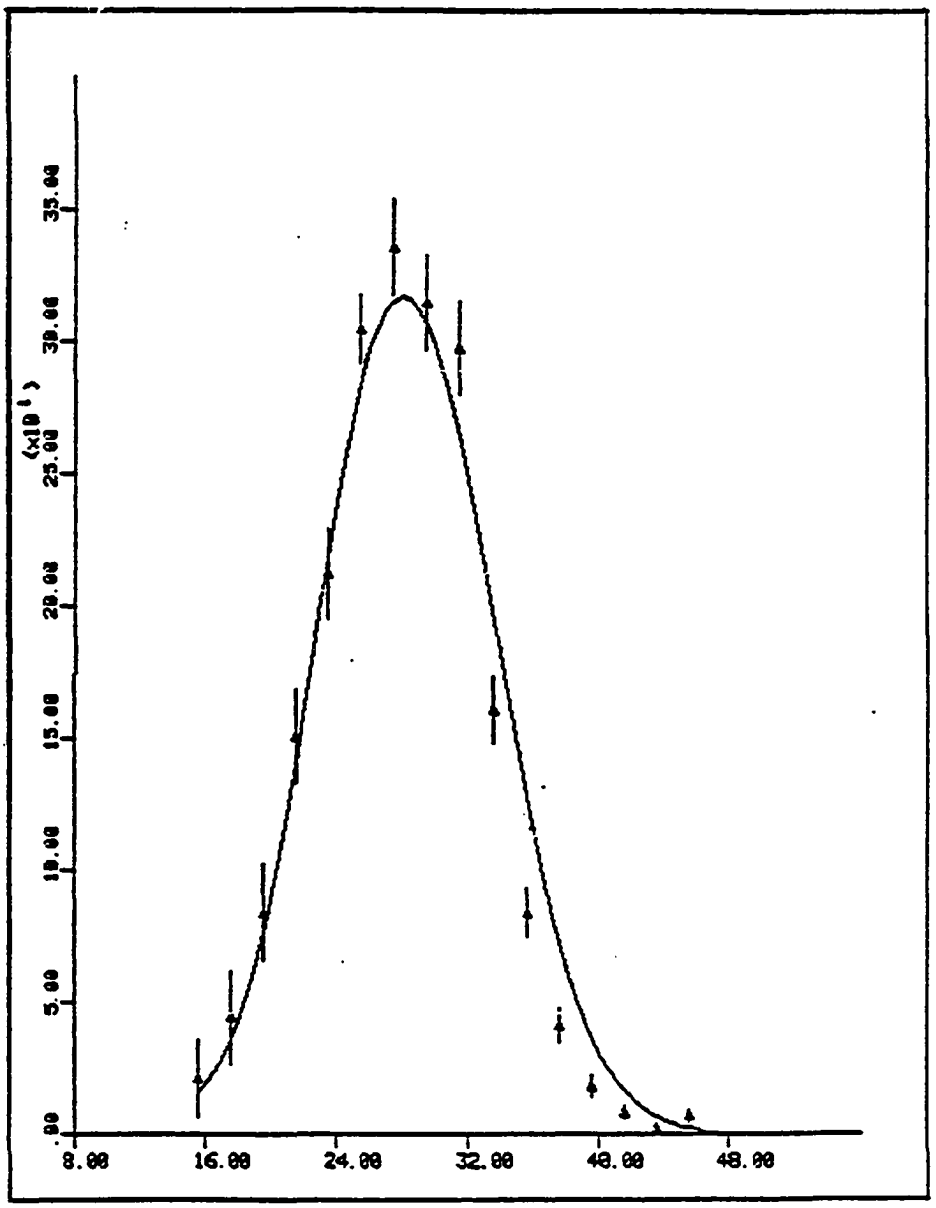

FIG. 5.7σ Distribution B1, Multiplicity 12

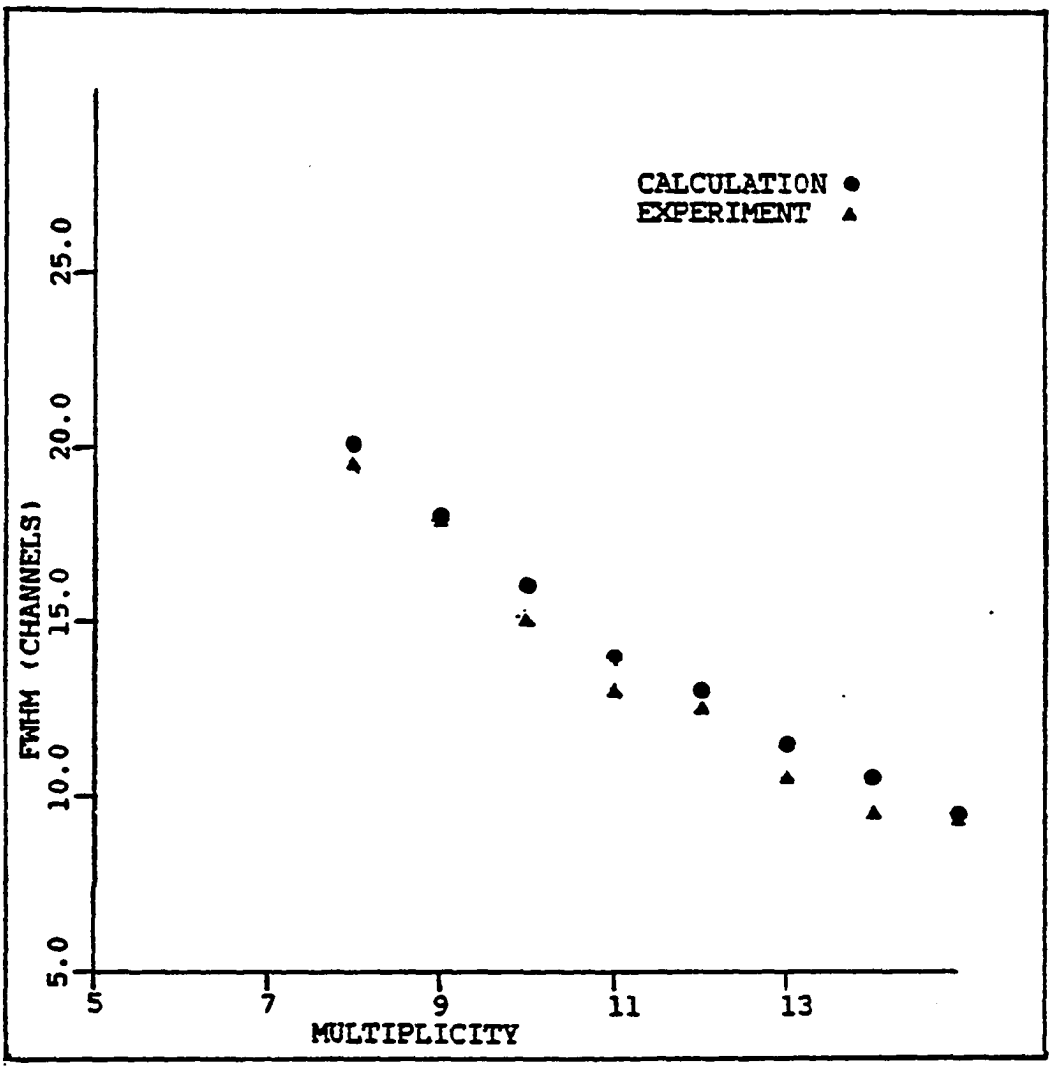

FIG. 5.8 Comparison of the calculated and experimental linewidths for distribution B1.

rate falls and chain breaking becomes important. The first set of curves (B1) were taken with a 33 μsec mode 2 reset time and are not as strongly affected by this as the second set of curves (B2) which had a τ of 15 μsec. This effect seems smaller on the left side of the ^{138}Ba peak. As shown in Figs. 3.1a and 5.7, the tail of the ^{135}Ba(5/2) falls in this region and is probably responsible for this difference.

The calculations do not produce lineshapes as asymmetric as the experimental data. The asymmetries are largest in multiplicities 4-8 and decrease in higher multiplicities. The Doppler width of the atomic beam is assumed to be zero in these calculations. The overall Doppler width of the atomic beam is 3 MHz, but the photon-burst process is somewhat velocity selective: the fast atoms contribute mainly to the lower multiplicities and the slower atoms contribute mainly to higher multiplicities. As a result, the lower multiplicities have larger Doppler widths than the higher multiplicities. Averaging the lower multiplicities (4-9) over frequency width increases the apparent skewness of their already asymmetric lineshapes as illustrated in 3.6a and b. This effect may account for part of the difference between the calculated and experimental lineshapes.

As discussed in Chapter III lineshapes can be conveniently characterized by their first three moments. Due

to the presence of the ^{135}Ba(5/2) (see Figs. 3.1a and 5.6) peak near the ^{138}Ba peak and the limited scanning range, exacerbated by the large widths of the lower multiplicity spectra, meaningful moments could not be extracted. A larger scan range using an isotopically pure sample is needed if moment data are to be obtained.

CHAPTER VI. CONCLUSIONS

System Sensitivity

One measure of the sensitivity is the length of time required to accumulate a signal that is recognizably different from background. The criterion that will be used is that the signal must be at the 3σ level, that is, the peak height must be at least three times the variance of the background. The time T to accumulate a signal of this level in spectrum n is determined by

$$3\sqrt{\overline{R_b(n)T}} = P_a(n)R_aT, \text{ or}$$

$$R_a^2T = \frac{9\ R_b(n)}{P_a^2(n)}$$

where R_a is the atomic flux, $R_b(n)$ is the background rate of multiplicity n, and $P_a(n)$ is the probability of a n multiplicity event produced by an atom. In Fig. 6.1 the relationship between the sensitivity parameter R_a^2T and multiplicity is shown for the photon number distribution $\langle R_1\rangle\langle T\rangle=13.5$, $\gamma=11.0$, with a background count rate of 7000 per sec taken with a mode 2 reset time of 15 μsec (distribution B2). The parameter is a minimum with a value of 35 at multiplicity 9, that is, a 35 sec measurement time is required to distinguish a beam flux of 1 atom/sec from background.

All multiplicities are measured simultaneously which increases the sensitivity. A simple way to make use of this

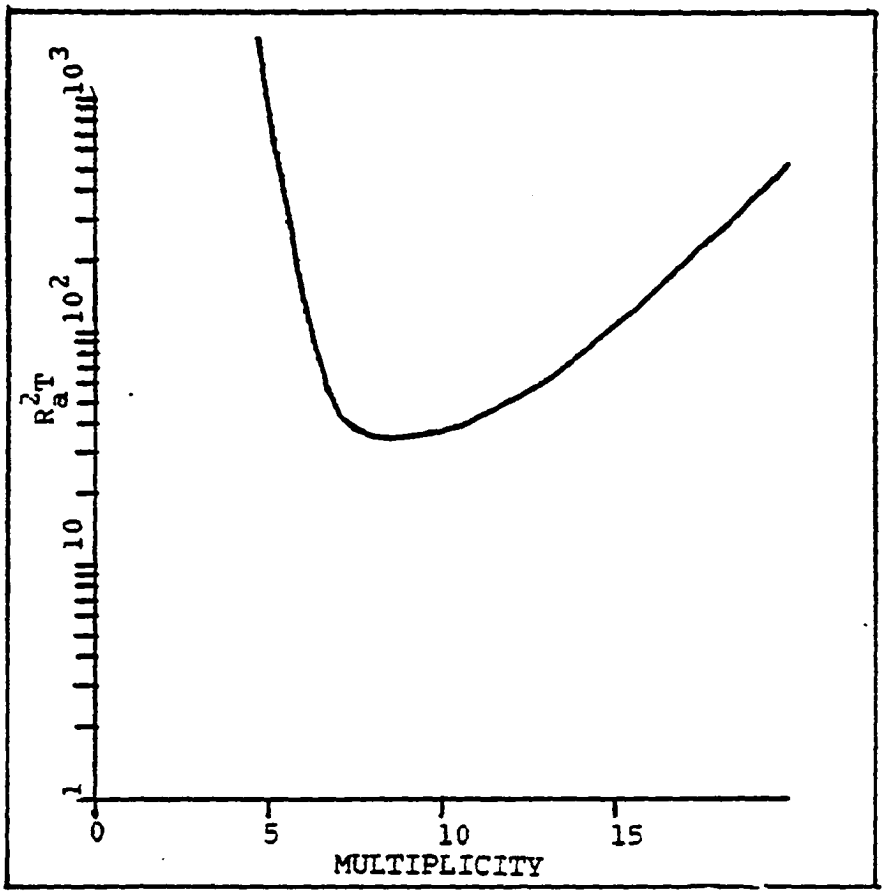

FIG. 6.1 R_a^2T versus multiplicity for the B_2 photon number distribution

information is to sum many multiplicities. The requirement for a signal to be recognizably different from background is then given as

$$R_a^2T=\frac{9\ \Sigma_{n=a}^{b}\ R_b(n)}{(\Sigma_{n=a}^{b}\ P_a(n))^2}$$

where a and b are the limits needed for maximum sensitivity. In Fig. 6.2 R_a^2T vs. the lower mutiplicity limit (a) is shown. The minimum of 1.96 occurs for a=7 and b=23. The sensitivity is weakly dependent upon the upper limit and changes little past b=23. Summing the multiplicities reduces the scan time necessary by a factor of 9. The observation time required for various beam fluxes are shown below:

Atom Rate	Time for 1 Channel	Time for 64 Channels
1 atom/sec	3.9 sec	4.1 min.
.1	6.4 min	6.9 hr.
.01	10.7 hrs	28.5 days.

The time for one channel is the time to accumulate the necessary statistics when the laser is exactly on resonance and the time for 64 channels is the length of time to do a 64 channel frequency scan of the region of interest.

If a one count/tube coincidence is used, as was done in this work, the practical sensitivity limit, with a thermal beam of barium atoms, is approximately 1 atom per 100 sec.

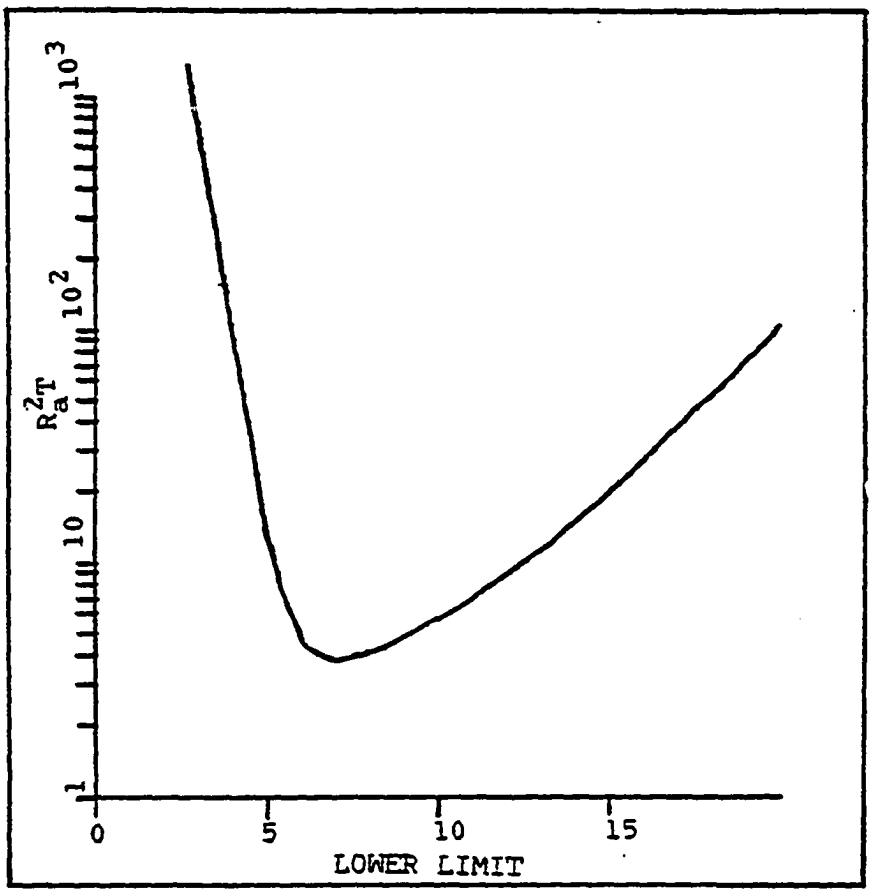

Fig. 6.2 The summed R_a^2T versus the lower limit of the sum. The upper limit of the sum is the value which maximizes sensitivity

Requiring two count/tube has been shown to reduce the dark count background by an additional factor of one hundred. In a two count per tube mode, the system sensitivity could be expected to be on the order of 1 atom per 10^4 sec. Utilizing such sensitivity would require an extremely reliable laser system; at a beam flux of 10^{-4} atom/sec twelve days would be required for one hundred atoms to pass through the laser beam for each channel.

The sensitivity depends upon the average number of detected photons and the background rate. The photon burst mode used and clock setting for maximum sensitivity depends upon the type of atomic beam used, and the details of the atomic resonance. The sensitivity will vary as conditions change and each situation needs to be individually analyzed.

Photon Number Distributions

The experimental distributions are described quite well by the three-level atom photon number distribution of Chapter III. This is the first time that such a distribution has been observed to diverge from a simple Poisson distribution averaged over the atomic velocity distribution. This provides a new way to measure the atomic branching ratios.

The value obtained for the barium branching ratio, 375±30 is significantly lower than the value of 700 obtained by Bernhardt et al. (25). No errors limits are quoted in the

article, but author compares the experimental branching ratio to a calculated value of 600 (24) and implies the two values are in close agreement. This indicates the error in Bernhardt's value of the branching ratio is at least ±100.

It is unlikely that the gamma value of 11.1 is grossly in error; the results from all six extended interaction regions are close to this number and <n> values are consistent with a γ of 11. The light collection detection efficiency of the system would need to be on the order of 1.5% in order for the branching ratio to be 700. This also seems unlikely as the estimate of efficiency from measurements of the various components (see Chapter II) puts the lower limit at 2.6% and the efficiency from the scattered photon distribution (see Chapter V) implies that the efficiency is 3%. If the calculations of N_p are too low by a factor of two, the resulting efficiency would be overestimated by this same factor. The values for the upper level occupation probability used predicted the atoms were scattering nearly the maximum possible for laser profiles B3 and C3, so N_p would, if anything, already be too high. Errors in this calculation could raise the efficiency but not lower it.

Spectral Lineshapes

The spectral lineshapes are reasonably well described by the calculations except for the larger than predicted

asymmetries in multiplicities 4-8. These multiplicities are dominated by atoms which have been optically pumped and have higher than average velocities. It does not seem likely that the optical pumping process could be responsible for the asymmetry. The fast atoms have a Doppler width that is larger than average, which increases the width and apparent skewness of the photon burst lineshapes. The average Doppler width (3 MHz) is small and has been ignored in the calculations. It is possible that the larger Doppler widths in the lower multiplicities are the cause of the discrepancy.

REFERENCES

1. E. W. Otten, in Fourth International Conference on Nuclei Far from Stability, Proceedings CERN report 81-09 (1981)

2. P. Jacquinot and R. Klapisch, Rep. Prog. Phys. 42, 612 (1979)

3. G. Huber, J. Boon, H. J. Kluge, and E. W. Otten, Z. Physics, A276, 187 (1976)

4. K. Heileg and A. Steudel, Atomic Data and Nuclear Data Tables 14, 613 (1974)

5. M. Burns, P. Pappas, M. S. Feld, and D. E. Murnick, Nuc. Inst. and Methods 141, 429 (1977)

6. C. E. Bemis, Jr., J. R. Beene, J. P. Young, and S. D. Kramer, Phys. Rev. 43, 1854 (1979)

7. J. R. Zacharias, Phys. Rev. 61, 270 (1942)

8. G. Huber, C. Thibault, R. Klapisch, H. T. Duang, J. L. Vialle, J. Pinard, P. Juncar, and P. Jacquinot, Phys. Rev. Lett. 34, 1209 (1975)

9. C. Thibault and F. Touchard, Lasers in Nuclear Physics, Edited by C. E. Bemis and H. K. Carter, (Harwood Academic Publishers, New York 1982)

10. C. Duke, H. Fischer, H. J. Kluge, H. Kremmling, T. Kuhl, and E. W. Otten, Phys. Rev. 50A, 1829 (1977)

11. I. Lindgren, E. Matthias, and A. Timmerman, Lasers in Nuclear Physics, Edited by C. E.Bemis and H. K. Carter (Harwood Academic Publishers, New York 1982)

12. F. Schneider, W. Makat, E. Mattias, R. Wenz and P. J. West, Lasers in Nuclear Physics, Edited by C. E. Bemis and H. K. Carter, (Harwood Academic Publishers, New York 1982)

13. G. Nowicki, K.Bekk, S. Goring, A. Hanser, H. Rebel, and G. Schatz, Phys. Rev. C, 18, 2369 (1978)

14. S.L. Kaufman, Opt. Commun. 17, 309 (1976)

15. R. Neugart Lasers in Nuclear Physics, Edited by C. E. Bemis and H. K. Carter (Harwood Academic Publishers, New York, 1982)

16. G. Greenlees, D. Clark, S. Kaufman, D. Lewis, J. Tonn, and J. Broadhurst, Opt. Commun. 23, 236 (1977)

17. D. A. Lewis, J. F. Tonn, S. L. Kaufman, and G. W. Greenless, Phys. Rev. A 19, 1580 (1979)

18. D. Lenstra, Phys. Rev. A 26, 3369 (1982)

19. R. Cook, Phys. Rev. A 23, 1243 (1981)

20. L. Mandel, Optics Letters 4, 205 (1979)

21. L. Mandel, Proc. Phys. Soc. 72, 1037 (1958)

22. J. A. Abate, H. J. Kimble, and L. Mandel, Phys. Rev. A 14, 788 (1976)

23. B. M. Miles and W. L. Wiese, U.S. National Bur. Stand. Tech. Note 474 (1969)

24. P. McCavert and E. Trefftz, J. Phys. B7, 1270 (1974)

25. A. F. Bernhardt, D. E. Duerre, J. R. Simpson and L. L. Wood, J. Opt. Soc. Am. 66, 416 (1976)

26. J. Aysto, S. Hillebrand, K. H. Helmuth, and K. Valli, Nucl. Inst. Meth. 120, 163 (1974)

27. C. N. Davids, G. W. Greenlees, S. L. Kaufman, M. A. Finn, D. A. Lewis, R. Evans, in Proceedings of the Forth International Conference on Nuclei Far from Stability, Edited by L. O. Stolen, (Helsingor, Denmark (1981)

28. W. Dick, G. Greenlees, and S. Kaufman, Phys. Rev. Lett. 53, 431 (1984)

29. W. Dick, Ph.D. Thesis, University of Minnesota, 1984 (unpublished)

30. W. Fairbank, Jr., T. Hansch, and A. Schawlow, J. Opt. Soc. Am. 65, 199 (1975)

31. H. Kuhn, Proc. in Chemistry of Organic Natural Products, Edited by D. L. Lechmeister (Springer-Wein 1958-1959)

32. F. D. Schafer, Topics in Applied Physics, Vol.1, (Springer-Verlag, New York 1977)

33. C. L. Tang, H. Stuzt and G. de Mars, J. Appl. Phys., 34, 2289 (1963)

34. J. B. White, Nature 201, 911 (1964)

35. A. Clobes and M. Brienza, Appl. Phys. Lett. 21, 256 (1972)

36. A. Jenkins and H. White, Fundamentals of Optics, Fourth ed., (McGraw Hill, New York, 1976)

37. S. Jarret and J. Young, Optics Letters 6, 176 (1977)

38. A. Bloom, Opt. Engineering 1, 1 (1972)

39. M. Born and E. Wolf, Fundamentals of Optics, (Pergamon Press, Oxford, England, 1969)

40. D. R. Preuss and J. L. Gole, Applied Optics 19, 702 (1980)

41. G. Holtom and O. Teschke, IEEE J. Quantum Electro 10, 577 (1974)

42. M. Hercher, Applied Optics 5, 951 (1978)

43. Spectra-Physics Laser Technical Bulletin Number 6, (Spectra-Physics Inc., Mt. View CA. 1968)

44. M. Baumann and G. Wander, Phys. Lett. A 28, 200 (1968)

45. M. Coulombe and A. Pine, Applied Optics 18, 1505 (1979)

46. P. Juncar and J. Pinard, Opt. Commun. 14, 438 (1975)

47. R. Barger and J. Hall, Phys. Rev. Lett. 22, 4 (1969)

48. H. Gerhardt and A. Timmerman, Opt. Commun. 21, 343 (1977)

49. D. A. Lewis, R. Evans, M. A. Finn, Rev. Sci. Inst., to be published (1985)

50. Spectra-Physics Tech. Report No. 2 (1968)

51. J. Ferguson and R. Morris, Applied Optics 12, 2808 (1975)

52. J. B. Fergeson and R. H. Morris, Applied Optics 18, 2924 (1978)

53. T. Baer, F. V. Kowalski, and J. L. Hall, Applied Optics 18, 3173 (1980)

54. F.V. Kowalski, R. T. Hawkins and A. L. Schawlow, J. Opt. Soc. Am. 66, 956 (1976)

55. M. A. Finn, Private Communication, University of Minnesota

56. R. Hanbury-Brown and R. Twiss, Nature 177, 27 (1956)

57. E. M. Purcell, Nature 178, 1449 (1956)

58. F. W. Sears, An Introduction to Thermodynamics, the Kinetic theory of Gases and Statistical Mechanics, (Addison-Wesley, Cambridge, Mass., 1959)

59. L .I. Schiff, Phys. Rev. 50, 88 (1936)

60. D. A. Lewis, Department of Energy Progress Report, Iowa State University, 1981 (unpublished)

61. R. D. Evans, The Atomic Nucleus, (McGraw-Hill, New York, 1955)

62. E. D. West and D. A. Jennings, Rev. Sci. Inst. 41, 565 (1970)

63. P. R. Bevington, Data Reduction and Error Analysis for the Physical Sciences, (McGraw Hill, New York, 1969)

PARTIAL TABLE OF SYMBOLS

A	Einstein spontaneous emission coefficient
A_1	$N_0 \varepsilon A \langle T \rangle$
c	speed of light
D	distance from center to 1/e point of laser beam intensity profile
$D_{1/2}$	Half width at half maximum of laser beam intensity profile
$\bar{E}$	laser electric field strength
FWHM	Full Width at Half Maximum
$\hbar$	$h/2\pi$
I	laser beam intensity
K	proportionality constant between Ω^2/A^2 and I
K_b	Boltzman constant
n_e	index of refraction of extraordinary axis in birefringent material
n_o	index of refraction of ordinary axis in birefringent material
N_0	number of atoms which passed through laser beam
N_F	number of free parameters
$\langle n \rangle$	$\Sigma_0^{+\infty} n\, P(n)$, average multiplicity of a distribution
$\langle (\Delta n)^2 \rangle$	variance of a probability distribution
N_p	calculated number of photons scattered by a two level atom traversing a laser beam of a given

	size and total power
$P(v)dv$	probability of atom having velocity between v and v+dv
$P(n,t)$	probability of detecting n photons in time t
$P_{op}(n)$	probability of detecting n photons from an optically pumped atom
$P_{3L}(n)$	probability of n photons when branching is possible
Q	second factorial moment, $\{\langle(\Delta n)^2\rangle-\langle n\rangle\}/\langle n\rangle$
Q_{3L}	Q parameter for a three level system
R	R_1+R_2
R_a	atomic flux
R_b	background rate
R_e	spontaneous emission rate
R_1	εR_e, photon detection rate
R_2	χR_e, rate of decay to metastable state
$\langle R_1\rangle$	$\varepsilon A\bar{O}$, photon scattering rate averaged over laser beam profile
T	atomic transit time
T_e	oven temperature
$\langle T\rangle$	$D\int_0^{+\infty} P(v)\, dv/v$, average atomic transit time
v	atomic velocity
X	direction in laser beam-atomic beam system parallel to the laser beam
Y	direction in laser beam-atomic beam system perpendicular to both laser beam and atomic

	beam
Z	direction in laser beam-atomic beam system parallel to the atomic beam
β	v/c
χ^2_ν	χ^2/N_F
Δ	frequency difference between laser and atomic transition
ε	light collection and detection efficiency
γ	ε/x, $\langle n \rangle$ in optical pumping limit
Γ_L	laser frequency width
λ	light wavelength
τ	mode 2 reset time
Ω	Rabi frequency parameter
ω_L	laser frequency
ω_0	atomic transition frequency
x	atomic branching ratio

APPENDIX

Background Interference

Background counts follow two types of statistics, depending on whether the clock is in mode 1 or mode 2. While the atom is in the beam it is assumed that resonantly scattered photons are continually resetting the clock which causes the background statistics to correspond to mode 1. Before (after) the atom enters (leaves) the beam background counts reset the clock so the statistics correspond to mode 2. In this appendix an expression for $P_b(n,y)$, the probability for additional y background counts in a burst of n counts from an atom, is derived.

In the time before the atom enters the beam, the probability that a count string of multiplicity y_2' is produced and added to the atom-scattered count chain is

$$P_{b2}(y_2')=(1-e^{-R_b\tau})^{y_2'}e^{-R_b\tau}.$$

Similarly, the chance of a string of y_2'' counts occurring after the atom left the beam is

$$P_{b2}(y_2'')=(1-e^{-R_b\tau})^{y_2''}e^{-R_b\tau}.$$

The probability that $y_2=y_2'+y_2''$ counts are added to the atomic photon chain is

$$P_{2b}(y_2)=P_{b2}(0)P_{b2}(y_2)+P_{b2}(1)P_{b2}(y_2-1)+\ldots+P_{b2}(y_2)P_{b2}(0).$$

There are y_2+1 terms in this expression, each one equal to

$$(1-e^{-R_b\tau})^{y_2'}e^{-R_b\tau}(1-e^{-R_b\tau})^{y_2''}e^{-R_b\tau}=(1-e^{-R_b\tau})^{y_2}e^{-2R_b\tau}.$$

This means $P_{2b}(y_2)$ is given by

$$P_{2b}(y_2)=(1+y_2)(1-e^{-R_b\tau})^{y_2}\, e^{-2R_b\tau}.$$

The probability for y_1 background counts while an atom is retriggering the clock is

$$P_{1b}(y_1)= [(R_bT_r)^{y_1}\ e^{-R_bT_r}]/y_1!$$

where T_r is the time that the atom spends resetting the clock. If the atoms are optically pumped while in the laser beam it can be shown that the probability distribution of T_r is

$$P(T_r)dT_r=R_1[(R_1T_r)^{n-2}\ e^{-R_bT_r}]/(n-2)!\ dT_r$$

where n is the multiplicity of the event and R_1 is the average photon detection rate. The probability of y_1 background counts occurring while a n multiplicity atom is retriggering the clock is

$$P_{1bop}(n,y_1)=\int_0^{+\infty} P(T_r)[(R_bT_r)^{y_1}\ e^{-R_bT_r}]/y_1!\ dT_r$$

$$=\{(n-2+y_1)!/[(n-2)!y_1!]\}\ (R_b/R_1)^{n+y_1-1}\ 1/(1+R_b/R_1).$$

If R_b/R_1 is small, $P_{1bop}(n,y_1)$ can be written as

$$P_{1bop}(n,y_1)=[(n-1)R_b/R_1)^{n}\ e^{-(n-1)R_b/R_1}]/y_1.$$

This is equivalent to substituting $(n-1)/R_1$, which is the average time spent resetting the clock at multiplicity n, for T in eq. 4.3. A plot generated from the Monte Carlo program of average time between first and last detected photons versus multiplicity for various photon detection rates is shown in Fig. A.1. The probability of being

optically pumped before leaving the laser beam is dependent upon the number of photons scattered. If an atom has a high scattering rate, it is more likely to have branched to the metastable state than an atom which has scattered fewer photons. The lower multiplicities in Fig. A.1 fit $\langle T\rangle=(n-1)/R_1$ quite well. These multiplicities are dominated by atoms which have been optically pumped. The higher multiplicities diverge from the $\langle T\rangle=(n-1)/R_1$ relationship, especially for lower scattering rates. This is because the atoms contributing to these multiplicities are not being optically pumped before leaving the laser beam.

Atoms which leave the beam without being optically pumped (transit-time-limited) do not have the same T_r distribution as those that are optically pumped, which is why the points fall beneath the line in Fig. A.1 for the higher multiplicities. The T_r distribution for a transit-time-limited atom is

$$P_{tt}(T_r)dT_r=n(n-1)(1-T_r/T)(T_r/T)^{n-1}dT_r/T_r$$

where T is the time the atom spends in the beam. The probability of y_1 background counts is

$$P_{btt}(y_1,T)=\int_0^T P_{tt}(T_r)\left[(R_bT_r)^{y_1}e^{-R_bT_r}\right]/y_1!\,dT_r$$

$$=\frac{n(n-1)}{y_1!}(R_bT)^{y_1}e^{-R_bT}(n+y_1-1)!\sum_{k=0}^{+\infty}\frac{(R_bT)^k}{(n+y_1+k)!}\,. \qquad \text{A.1}$$

FIG. A.1 The average transit-time versus multiplicity for three different rates. The P(T) function was obtained from eq. 4.1 such that $\langle T \rangle = 25$ μsec

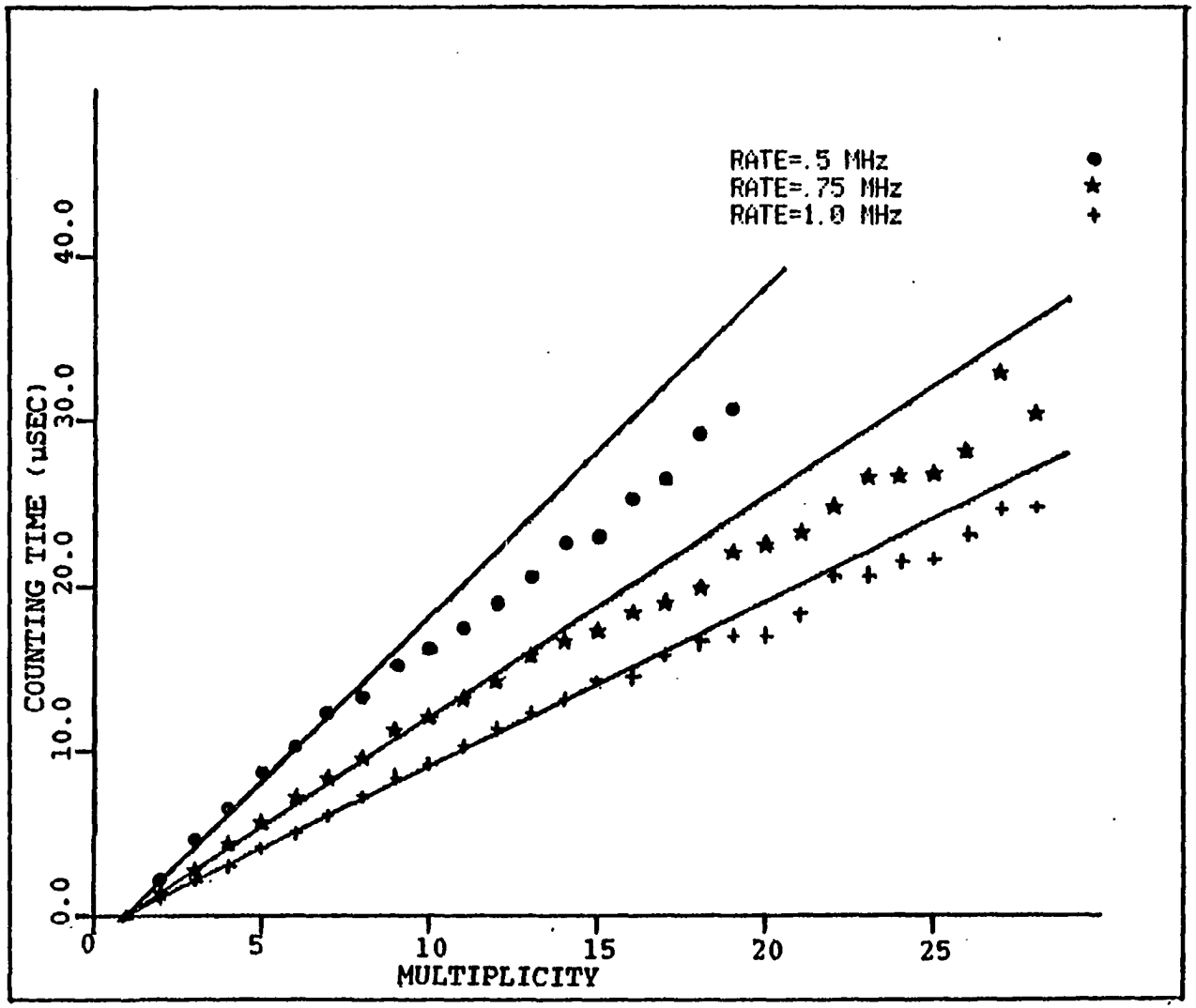
RATE=.5 MHz
RATE=.75 MHz
RATE=1.0 MHz
COUNTING TIME (μSEC)
0.0
10.0
20.0
30.0
40.0
0
5
10
15
20
25
MULTIPLICITY

The probability that an atom with transit time T will give rise to a n multiplicity event is $[(R_1T)^n e^{-(R_1T)}]/n!$. The probability that a n multiplicity event was caused by an atom with transit time T is

$$P(T(n))dT=P_a(T)\,[(R_1T)^n e^{-R_1T}]/n!\;dT$$

where $P_a(T)$ is the distributions of atomic transit times. This function is shown in Fig. A.2 for three different values of n. The average value of T for a given multiplicity is given by

$$\langle T(n)\rangle=\frac{\int_0^{+\infty} T\,P(T)[(R_1T)^n e^{-R_1T}]/n!\;dT}{\int_0^{+\infty} P(T(n))dT}.$$

Some examples of $\langle T(n)\rangle$ vs. n are shown in Fig. A.3. It can easily be seen that higher multiplicity events come from atoms which spend more time in the laser beam. The number of background counts that can be expected while a transit time limited atom is in the beam is

$P_{btt}(y_1,n)=\int_0^{+\infty}P(T(n))P_{btt}(y_1,T)dT.$

Because of the form of $P_a(T)$, $P_{lbtt}(y_1,n)$ can only be found numerically.

The background counts at a given multiplicity can be found if the atom either traverses the entire laser beam or

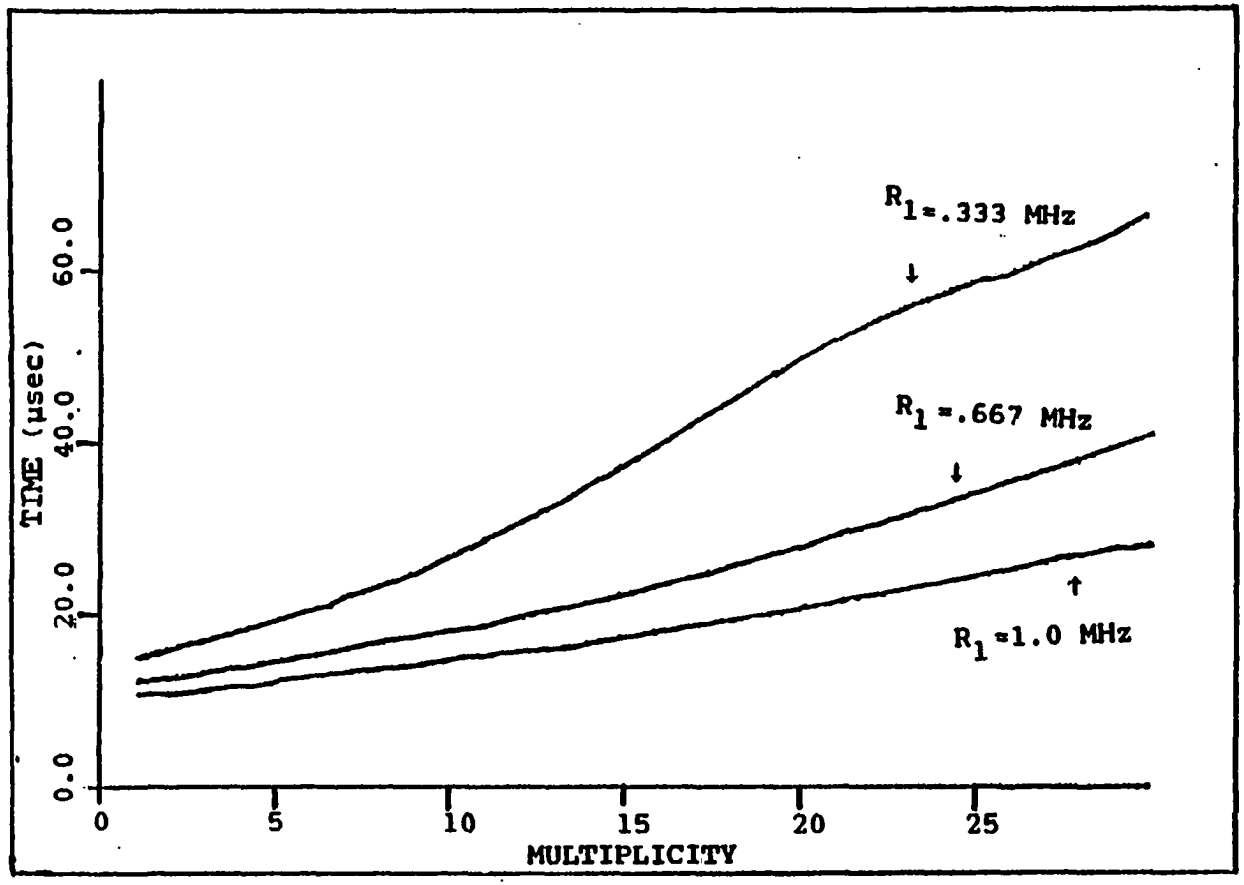

FIG. A.2 Average atomic transit-times versus multiplicity for transit time limited atoms

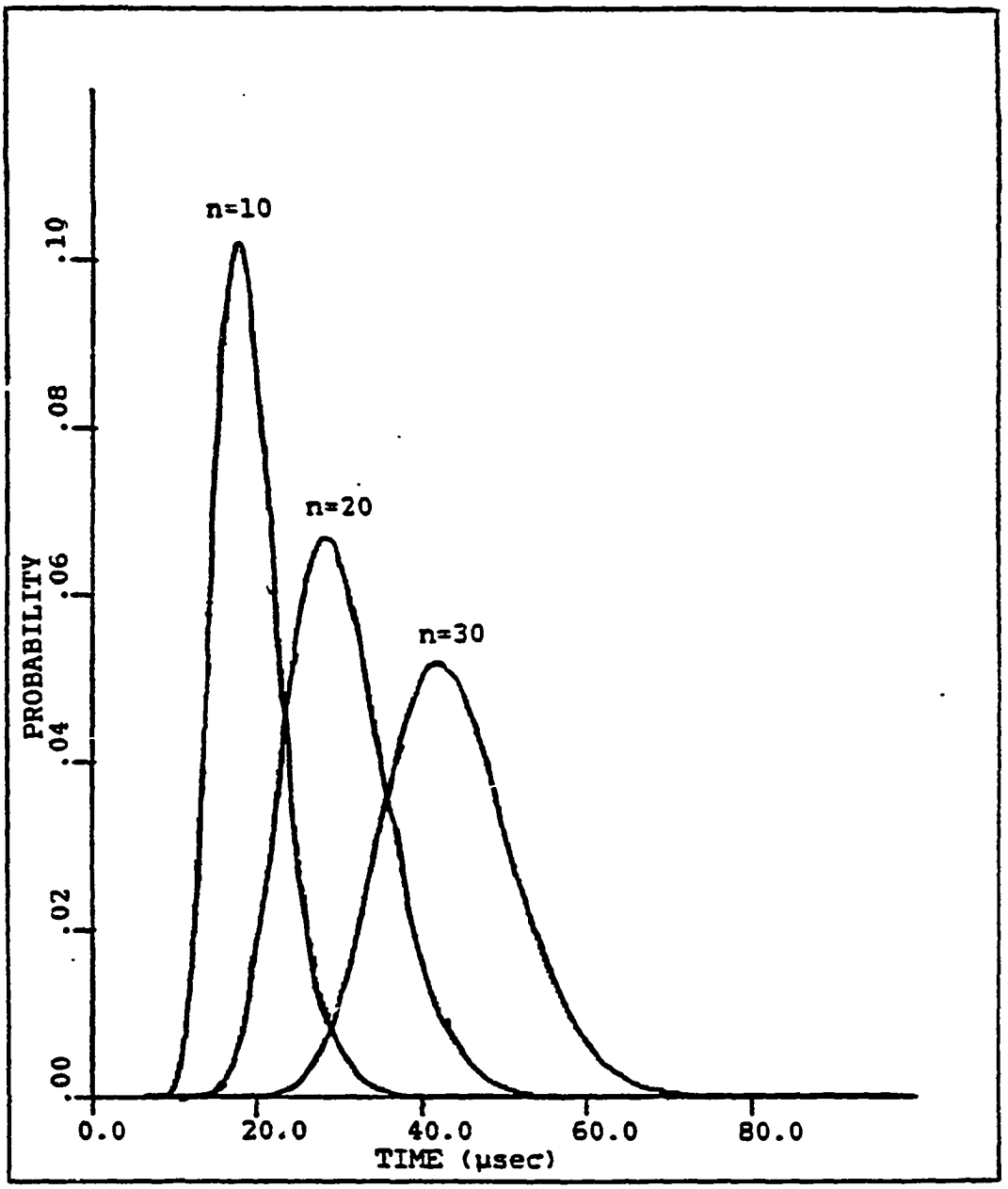

Figure A.3 Distribution of transit-times for three different values of n. R_1=.667 MHz. P(T) obtained from eq. 4.1 such that ⟨T⟩=25 μsec

is optically pumped. At a given multiplicity some atoms are optically pumped, the rest are not. The probability of y_1 background counts is

$$P_{b1}(n,y_1)=F_{op}(n)P_{1bop}(y_1,n)+F_{tt}(n)P_{1btt}(y_1,n)$$

where $F_{op}(n)$ is the fraction of atoms which have been optically pumped at multiplicity n, and $F_{tt}(n)$ are the fraction which traversed the entire beam. These fractions can be found by using the equations of Chapter III.

Now that the background statistics from both sources are known, the probability of $y=y_1+y_2$ background counts being added to a multiplicity n event can be calculated. The probability of y additional counts being added to the photon string is equal to

$$P_b(n,y)=\sum_{k=0}^{y} P_{1b}(n,y-k)P_{2b}(k).$$